ADVANCED STEEL CONSTRUCTION

An International Journal

Volume 8 Number 4

December 2012

CONTENTS

Technical Papers

A Computational Study of the Static and Dynamic Response of a Hybrid Barrel Vault Structure
Jianguo Cai, Yixiang Xu, Fang Wang, Jian Feng and Jin Zhang

Compressive Performances of the Concrete Filled Circular CFRP-Steel Tube (C-CFRP-CFST)
Y. Che, Q.L. Wang and Y.B. Shao

Research on Effect of Sliding Between Hoop Cable and Cable-Strut Joint on Behavior of Suspen-Dome Structures
Hongbo Liu and Zhihua Chen

Strength and Ductility Evaluation Method for Steel Bridge Pier Frames Considering Effect of Shear Failure
L. Kang and H.B. Ge

Random Equivalent Initial Bow and Tilt in Steel Frame
A. Machowski and I. Tylek

The Effects of Frame Deformation on Welded Gusset Plates for Diagonal Bracing Elements Loaded in Tension
J. Kent Hsiao, Donald W. Tempinson and Jianming Li

Website: *http://www.hkisc.org*
ISSN 1816-112X
Science Citation Index Expanded, Materials Science Citation Index and ISI Alerting

Cover:
THE COAL STORAGE DOMES AT THE ENEL TORREVALDALIGA NORTH THERMOELECTRIC POWER PLANT, ITALY
Credits:
Photo ©: Alfredo D'Amato - Agenzia 7 Minutes
Structural system: MERO Italiana, Verona
Dome Design: Ing. Gilbert Pirozzi, Mero, Verona
Construction Management and Technical Support: ENEL Energy and Innovation Office,
Ing. Giovanni Belloni, Ing. Marco Ulisse, Ing. Ubaldo Savina, Ing. Sergio Castronuovo.
Scientific Consultant: Prof. Federico M. Mazzolani,University of Naples

ADVANCED STEEL CONSTRUCTION

VOL.8, NO.4 (2012)

ADVANCED STEEL CONSTRUCTION

an International Journal

ISSN 1816-112X

Volume 8 Number 4 *December 2012*

ADVANCED STEEL CONSTRUCTION
an international journal

ISSN 1816-112X

Science Citation Index Expanded, Materials Science Citation Index and ISI Alerting

Advanced Steel Construction
an international journal

Cover: **THE COAL STORAGE DOMES AT THE ENEL TORREVALDALIGA NORTH THERMOELECTRIC POWER PLANT, ITALY**

General Information
Advanced Steel Construction, an international journal

Aims and scope

The International Journal of Advanced Steel Construction provides a platform for the publication and rapid dissemination of original and up-to-date research and technological developments in steel construction, design and analysis. Scope of research papers published in this journal includes but is not limited to theoretical and experimental research on elements, assemblages, systems, material, design philosophy and codification, standards, fabrication, projects of innovative nature and computer techniques. The journal is specifically tailored to channel the exchange of technological know-how between researchers and practitioners. Contributions from all aspects related to the recent developments of advanced steel construction are welcome.

Instructions to authors

Submission of the manuscript. Authors may submit double-spaced manuscripts preferably in MS Word by emailing to one of the chief editors as follows for arrangement of review. Alternatively papers can be submitted on a diskette to one of the chief editors.

Asian Pacific , African and organizing editor : Professor S.L. Chan, Email: ceslchan@polyu.edu.hk
American editor : Professor W.F. Chen, Email: waifah@hawaii.edu
European editor : Professor R. Zandonini, Email: riccardo_zandonini@ing.unitn.it

All manuscripts submitted to the journal are recommended to accompany with a list of four potential reviewers suggested by the author(s). This list should include the complete name, address, telephone and fax numbers, email address, and at least five keywords that identify the expertise of each reviewer. This scheme will improve the process of review.

Style of manuscript

General. Author(s) should provide full postal and email addresses and fax number for correspondence. The manuscript including abstract, keywords, references, figures and tables should be in English with pages numbered and typed with double line spacing on single side of A4 or letter-sized paper. The front page of the article should contain:

a) a short title (reflecting the content of the paper);
b) all the name(s) and postal and email addresses of author(s) specifying the author to whom correspondence and proofs should be sent;
c) an abstract of 100-200 words; and
d) 5 to 8 keywords.

The paper must contain an introduction and a conclusion. The length of paper should not exceed 25 journal pages (approximately 15,000 words equivalents).

Tables and figures. Tables and figures including photographs should be typed, numbered consecutively in Arabic numerals and with short titles. They should be referred in the text as Figure 1, Table 2, etc. Originally drawn figures and photographs should be provided in a form suitable for photographic reproduction and reduction in the journal.

Mathematical expressions and units. The Systeme Internationale (SI) should be followed whenever possible. The numbers identifying the displayed mathematical expression should be referred to in the text as Eq. (1), Eq. (2).

References. References to published literature should be referred in the text, in the order of citation with Arabic numerals, by the last name(s) of the author(s) (e.g. Zandonini and Zanon [3]) or if more than three authors (e.g. Zandonini et al. [4]). References should be in English with occasional allowance of 1-2 exceptional references in local languages and reflect the current state-of-technology. Journal titles should be abbreviated in the style of the Word List of Scientific Periodicals. References should be cited in the following style [1, 2, 3].

Journal: [1] Chen, W.F. and Kishi, N., "Semi-rigid Steel Beam-to-column Connections, Data Base and Modelling", Journal of Structural Engineering, ASCE, 1989, Vol. 115, No. 1, pp. 105-119.
Book: [2] Chan, S.L. and Chui, P.P.T., "Non-linear Static and Cyclic Analysis of Semi-rigid Steel Frames", Elsevier Science, 2000.
Proceedings: [3] Zandonini, R. and Zanon, P., "Experimental Analysis of Steel Beams with Semi-rigid Joints", Proceedings of International Conference on Advances in Steel Structures, Hong Kong, 1996, Vol. 1, pp. 356-364.

Proofs. Proof will be sent to the corresponding author to correct any typesetting errors. Alternations to the original manuscript at this stage will not be accepted. Proofs should be returned within 48 hours of receipt by Express Mail, Fax or Email.

Copyright. Submission of an article to "Advanced Steel Construction" implies that it presents the original and unpublished work, and not under consideration for publication nor published elsewhere. On acceptance of a manuscript submitted, the copyright thereof is transferred to the publisher by the Transfer of Copyright Agreement and upon the acceptance of publication for the papers, the corresponding author must sign the form for Transfer of Copyright.

Permission. Quoting from this journal is granted provided that the customary acknowledgement is given to the source.

Page charge and Reprints. There will be no page charges if the length of paper is within the limit of 25 journal pages. A total of 30 free offprints will be supplied free of charge to the corresponding author. Purchasing orders for additional offprints can be made on order forms which will be sent to the authors. These instructions can be obtained at the Hong Kong Institute of Steel Construction, Journal website: http://www.hkisc.org

The International Journal of Advanced Steel Construction is published quarterly by non-profit making learnt society, The Hong Kong Institute of Steel Construction, c/o Department of Civil & Structural Engineering, The Hong Kong Polytechnic University, Hung Hom, Kowloon, Hong Kong.

Subscription inquiries and change of address. Address all subscription inquiries and correspondence to Member Records, IJASC. Notify an address change as soon as possible. All communications should include both old and new addresses with zip codes and be accompanied by a mailing label from a recent issue. Allow six weeks for all changes to become effective.

The Hong Kong Institute of Steel Construction
HKISC
c/o Department of Civil and Structural Engineering,
The Hong Kong Polytechnic University,
Hunghom, Kowloon, Hong Kong, China.
Tel: 852- 2766 6047 Fax: 852- 2334 6389
Email: *ceslchan@polyu.edu.hk* Website: *http://www.hkisc.org/*
ISSN 1816-112X
Science Citation Index Expanded, Materials Science Citation Index and ISI Alerting

ISSN 1816-112X

Science Citation Index Expanded, Materials Science Citation Index and ISI Alerting

Advanced Steel Construction
an international journal

VOLUME 8 NUMBER 4 DECEMBER 2012

Technical Papers

A Computational Study of the Static and Dynamic Response of a Hybrid Barrel Vault Structure 317
Jianguo Cai, Yixiang Xu, Fang Wang, Jian Feng and Jin Zhang

Compressive Performances of the Concrete Filled Circular CFRP-Steel Tube (C-CFRP-CFST) 331
Y. Che, Q.L. Wang and Y.B. Shao

Research on Effect of Sliding Between Hoop Cable and Cable-Strut Joint on Behavior of Suspen-Dome Structures 359
Hongbo Liu and Zhihua Chen

Strength and Ductility Evaluation Method for Steel Bridge Pier Frames Considering Effect of Shear Failure 366
L. Kang and H.B. Ge

Random Equivalent Initial Bow and Tilt in Steel Frame 383
A. Machowski and I. Tylek

The Effects of Frame Deformation on Welded Gusset Plates for Diagonal Bracing Elements Loaded in Tension 398
J. Kent Hsiao, Donald W. Tempinson and Jianming Li

A COMPUTATIONAL STUDY OF THE STATIC AND DYNAMIC RESPONSE OF A HYBRID BARREL VAULT STRUCTURE

Jianguo Cai [1], Yixiang Xu [2,*], Fang Wang [3], Jian Feng [4,*] and Jin Zhang [5]

[1] *Ph.D., Key Lab. of C&PC Structures of Ministry of Education, Southeast University, China*
[2] *Lecturer, Department of Civil Engineering, Strathclyde University, United Kingdom*
[3] *Graduate Student, School of Civil Engineering, Southeast University, China*
[4] *Professor, Key Lab. of C&PC Structures of Ministry of Education, Southeast University, China*
[5] *Associate Professor, School of Civil Engineering, Southeast University, China*
**(Corresponding author: E-mail: yixiang.xu@strath.ac.uk(Yixiang Xu); seucivilfj@hotmail.com(Jian Feng))*

Received: 29 April 2011; Revised: 21 July 2011; Accepted: 23 September 2011

ABSTRACT: The use of cables as structural members has become very popular in spatial structures. The hybrid barrel vault is an attractive structural form in the design and construction of long-span transparent glass roof structures. These hybrid structures are very slender and lightweight, and hence sequential consideration in the structural behavior is needed. The mechanical characteristic, static and dynamic behaviors of the hybrid barrel vault are investigated in this paper. The effects of the structural parameters, such as rise-to-span ratios, cross-section areas of steel beams, areas and pre-stresses of cables, on the structural behavior have been studied in detail. Results show that cables do increase the structural stiffness of the hybrid barrel vault. The hybrid barrel vault with a good translucence is more efficient in load resistance than the general single-layer reticulated shell structure. Rise-to-span ratio is found to be an important factor influencing the structural behavior. The nodal displacement initially decreases with the increase of the height-to-span ratio and then increases afterwards. Given a specific height-to-span ratio, the increase of the beam section greatly reduces the nodal displacement and member forces and increases the natural frequency. It can also be found that it is not economical to improve the structural behavior by increasing the areas and pre-stresses of cables.

Keywords: Barrel vault, Cable, Anti-symmetrical load, Static analysis, Modal analysis

1. INTRODUCTION

In recent years, space structures have been broadly used all over the world. This has enhanced the rapid development of light weight structures, such as cable structures, membrane structures, and steel lattice structures. These structures are similar such that they are wide spans with a relatively small dead load [1]. Among these, barrel vaults having a form of a single-layer network of slender members are widely accepted as effective lightweight solutions to large span applications, because the barrel vaults carry loads mainly by normal forces. Recent applications have demonstrated that barrel vault structures covering clear spans of 17 m to 30 m have light self-weight of between 0.13 kN/m^2 and 0.20 kN/m^2 [2]. Also, the static and dynamic behavior of barrel vaults has been studied by many researchers [2-7].

With the development of modern buildings, the appeal of glass roofs grows with their translucence. Barrel vaults with quadrangular mesh are one of the best candidates for transparent glass roofs. However, El-Sheikh [2, 3] pointed out that a vault with quadrangular mesh lacks integration between its segments, which is essential for a reliable structural action especially when the vault is acting as a beam or suffers local damage. Moreover, the vaults become most dependent on the joint rigidity. These serious shortfalls in structural performance outweigh the apparent benefits in reducing the number and length of members used and might limit these vaults to applications with short spans and light loadings.

Cables are light and can provide well-defined transmission of forces. They can also been constructed to a structural system with a rational layout of members so as to make the best use of individual material properties [8]. Therefore, they are used in many hybrid string structures, such as beam string structures [9-11], and suspend-dome structures [12, 13]. To achieve high performance of the barrel vault with quadrangular mesh, a hybrid barrel vault roof is proposed [14-17], as shown in Figure 1. The single-layer steel trusses are diagonally stiffened by cables. Note the cables under compression will not become slack when the vault is pre-stressed before applying external loads. The hybrid barrel vault has a triangular mesh, which is a better structural configuration for barrel vaults [2, 3].

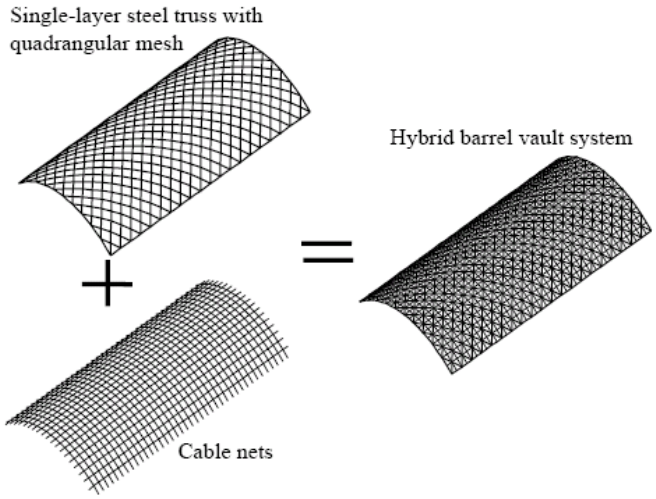

Figure 1. The Hybrid Barrel Vault System

Due to its attractive mechanical properties, the hybrid barrel vault has been widely used, e.g. the Word Trade Center Dresden and Atrium roof of Quartier 203 in Berlin [17], and the glass roof of New Guangzhou Railway station in China (as shown in Figure 2). The geometrical non-linear finite element analysis which considers imperfections of different shapes and scales was performed to study the stability of a hybrid barrel vault [1]. Harris *et al*. [18] described many innovations of creating the Downland Gridshell, a specialist museum workshop completed in the spring of 2002, such as multidisciplinary design, structural modeling, and the creation of new structural components, cladding, and construction processes. The principle of applying the cable pre-stress was investigated by Schlaich [16] based on a four-bar linkage diagonally stiffened by cables. Glymph *et al*. [19] studied the constructability of a hybrid shell using planar quadrilateral glass facets for the Jerusalem Museum of Tolerance project. They developed a simple but robust geometrical method for achieving the structure by incorporating the necessary geometrical principles into a computational parametric framework using the CATIA Version 5 system. The construction techniques and some case studies were concluded by Paoli [20]. He also investigated the development of high performance software and the use of new materials. Although the structural form is used in some projects, there is little research work reported about the structural characteristic of the hybrid vault barrel.

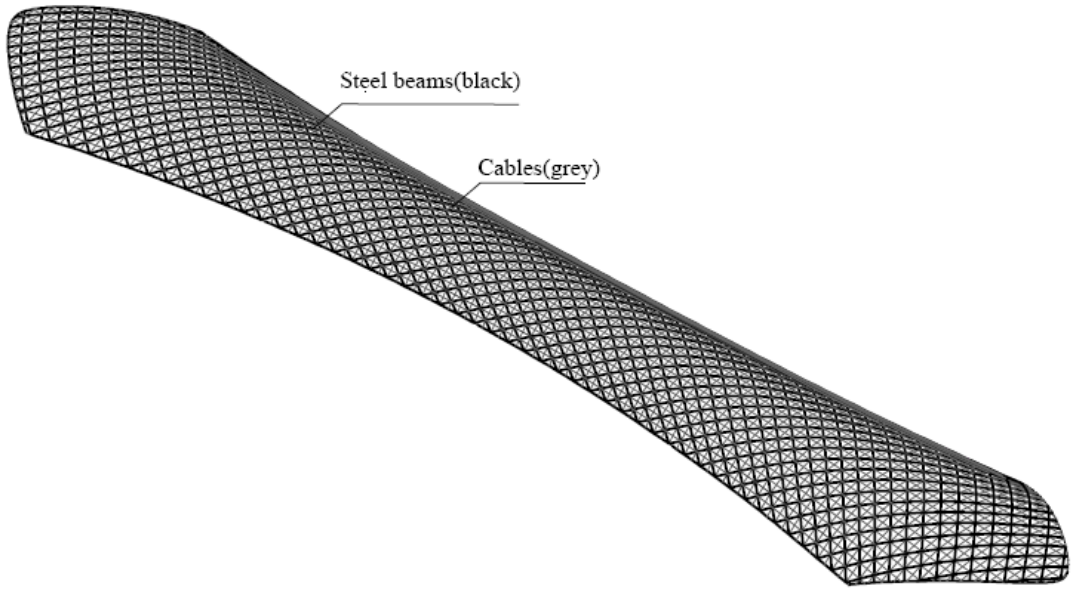

Figure 2. The Glass Roof of New Guangzhou Railway Station in China

This paper addresses several key issues of the hybrid barrel vault as shown in Figure 1. The mechanical characteristic of the hybrid structure is first investigated based on a frame structure stiffened by cables. Then a comparison of the static and dynamic behaviors between the hybrid barrel vault and the corresponding single-layer reticulated shell with quadrangular mesh is discussed in Section 3. Section 4 gives a parametric study of the static and dynamic behavior. Areas of steel bars and cables, pre-stresses of cables, rise-span ratios and different distribution of loads are considered. Section 5 draws some conclusions.

2. MECHANICAL CHARACTERISTIC OF THE HYBRID STRUCTURE

2.1 The Basic Idea of Cable Pre-stress Force in the Hybrid System

Unlike the tensegrity system, this hybrid system is stable before the cables are pre-stressed. Therefore, it does not require form-finding calculations. The pre-tensioned thin cables stiffen the quadrangular mesh barrel vault in two different ways. First, for a pin-connected four bar linkage, the cables transform the un-stiffened kinematic system into a statically determinate or indeterminate structure. For a single-layer rigid truss structure, the cables transform the system into a triangular meshed structure, which only allows in-plane flow of membrane forces resulting almost no bending stress in beams. The other method for cables to stiffen the hybrid system is that applying pre-tensions of cables transforms unfavorable compressive stresses into favorable tension stresses. Figure 3 shows a quadrangle of rigid beams with diagonal cables. One of diagonal cables will slack as it receives compression when the structure is under a lateral force. However, if cables have been pre-tensioned before applying the lateral load, neither cable will carry compression, and one cable carries a relatively higher tension leaving the other with a lower tension. It must be pointed out that the pre-stressed cables do not require a very high pre-stress, but ideally just large enough to prevent cables from slack when the structure is under service loads. It should be allowed that the cables be slack when the structure is in the ultimate state.

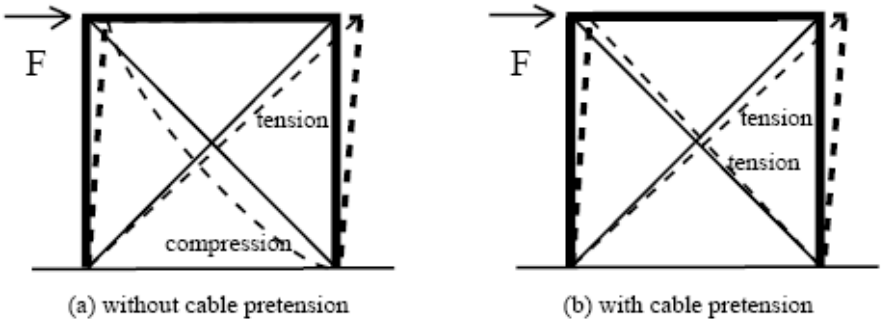

Figure 3. The Principle of Cable Pretension

2.2 Effects of Cables

Four load cases shown in Figure 4 are considered to investigate the effect of cables on the hybrid structure. Figure 5 shows the load-displacement curves for the braced and unbraced system. The load is plotted against the maximum displacement of a node. It is clear from the figure that the structural stiffness is rapidly reduced in the absence of pre-stressed cables for all load cases.

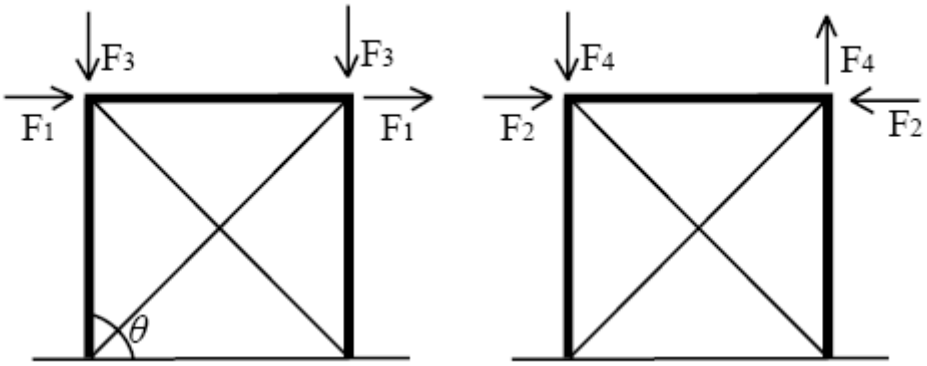

Figure 4. Four Different Load Cases

The load-displacement curves for the structure with different included angles are shown in Figure 6. The included angle θ is defined as the angle between two adjacent elements as shown in Figure 4. The included angle θ shown in Figure 6 corresponds to 15°, 30°, 45°, 60°, 75° and 90°, respectively. It can be seen from the figure that the stiffness of the structure with cables is higher than the structure without cables. Furthermore, the structural stiffness of an unbraced structure decreases with an increase of the included angle. However, for a braced structure, the structural stiffness reduces initially and increases afterward with the increase of included angles.

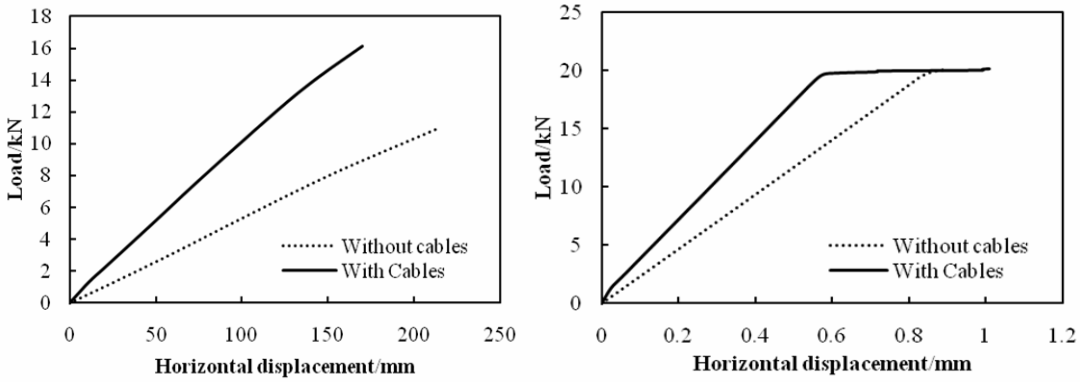

(a) Load F_1 (b) Load F_2

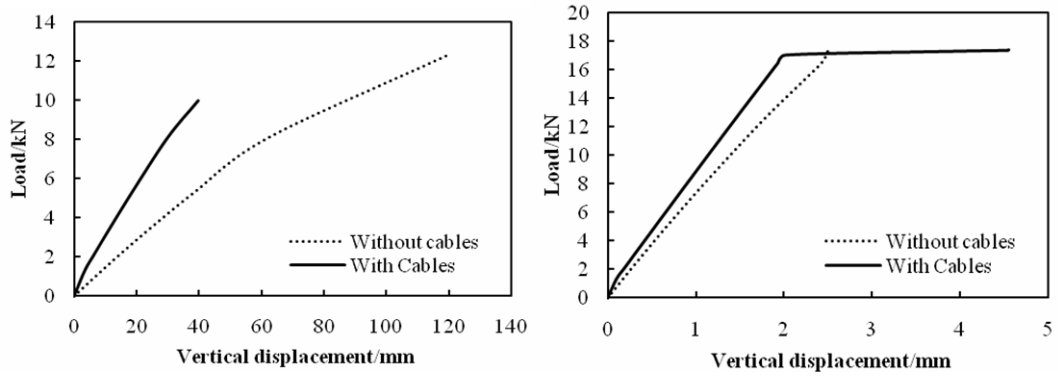

(c) Load F_3 (d) Load F_4

Figure 5. Load-displacement Curves for Different Load Cases

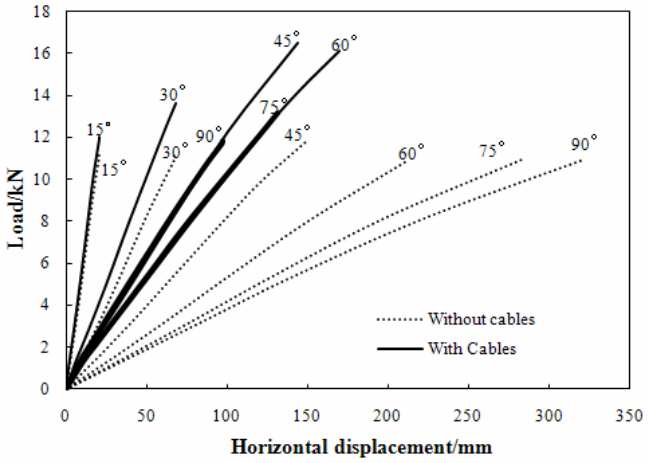

Figure 6. Load-displacement Curves for included Angles

3. STRUCTURAL BEHAVIOR OF A HYBRID VAULT BARREL

3.1 The Design Model

The design example used in this study is shown in Figure 7. The span and rise of the barrel vault structure are 20 m and 5.2 m, respectively (making the rise-span ratio 0.26). All nodes at the perimeter are hinged to the fixed support. Many types of connections are commonly used in space structure constructions such as welded hollow ball connections and bolt ball connections [13]. The welded hollow ball connection is adopted in this study, which is assumed to be rigid. The principal members of the single-layer steel trusses are made of steel with a Young's modulus of 206 GPa, and the cross-section is 120 mm × 60 mm × 4 mm (height × width × thickness). The yield strength of the steel beam is 345 MPa. The diameter of cables is 10 mm and the Young's modulus is 180 GPa. The initial stress of cables is 100 MPa.

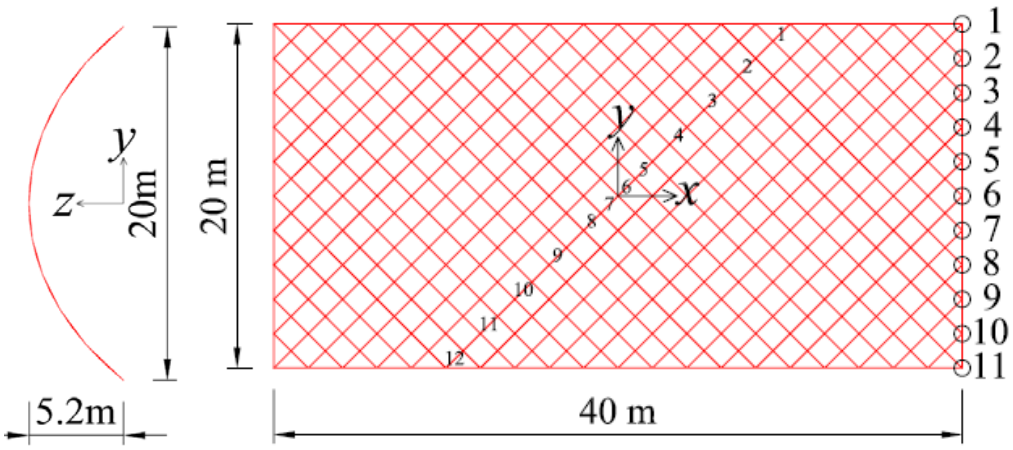

Figure 7. The Design Model of the Hybrid Barrel Vault with Typical Node and Element Numbers (Shown Without Cables)

The symmetrical load case *g+s* (dead load +snow load) has been taken into account in all computations. The dead load *g* consists of a self-weight of 0.5 kN/m^2 including all beams and cables. The snow load is applied to the top surface of the structure in the vertical direction with a magnitude of 0.5 kN/m^2.

The Finite Element Analysis software ANSYS is employed in all structural analyses that have taken into account the geometrical non-linearity. Tension-only element LINK10 is used to model cables and BEAM 189 is chosen to simulate steel beams. Due to the pre-stresses, all the cables remain in tension throughout the analysis.

3.2 Comparison between the Hybrid Barrel Vault and the Single-layer Lattice Structure

Static and dynamic analyses are carried out for the hybrid barrel vault structure and the corresponding single-layer lattice structure. The latter structure is formed by removing all the cables in the hybrid structure of the same dimension. By comparing the simulated results, one can evaluate the relative efficiency of those two structures.

3.2.1 Static analysis

The construction process of a pre-stressed space structure can be divided into three configurations: the zero state, the initial state and the loaded state. The structure in zero state is not pre-stressed. The initial state, also called pre-stressed state, is corresponding to the configuration under self-weight and initial forces. The loaded state is the shape under external actions.

In order to study the behavior of the hybrid structure under external loads, an analysis is carried out in three phases. In Phase I, only initial cable forces are applied to the finite element model to calculate the structural deformation and resultant forces of all members without any external load. In Phase II, based on a pristine unstressed numerical model, simulation is carried out to calculate the deformation and forces of members again after applying both the initial stresses and external loads. In Phase III, the overall structural responses of the hybrid barrel vault under external loads only can then be obtained by subtracting the results of Phase 1 from Phase 2. With the help of this approach, it is easy to identify individual member stress and nodal displacement due to external load only.

The typical nodes and elements of the barrel vault structure are shown in Figure 7. The vertical displacements for the typical nodes of the two structures are given in Figure 8. The vertical deflections of the single-layer lattice structure are much larger than those of the hybrid barrel vault structure. In general, the nodal displacements of the hybrid structure are less than 60% of the corresponding single-layer lattice structure.

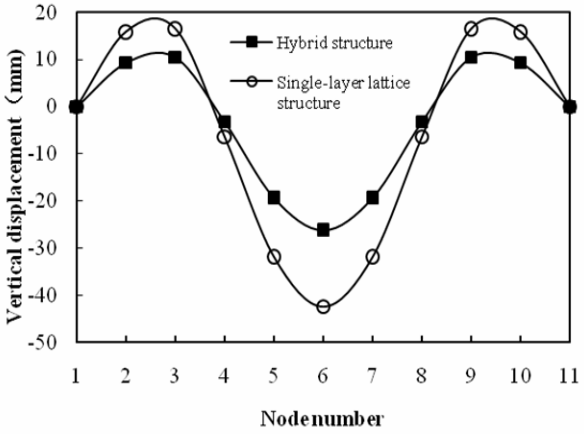

Figure 8. Vertical Displacement for Typical Nodes

In addition to the deformation, Figure 9 shows the cables also greatly reduce axial forces. It is clear from the figure that the magnitudes of the axial forces in the hybrid structure are much smaller than those of the corresponding single-layer lattice structure, especially for the members adjacent to the center of the span. With the help of the cables, the axial force of element 6, as labeled in Figure 7, decreases from 11.24 kN to 10.23 kN in the presence of an external load.

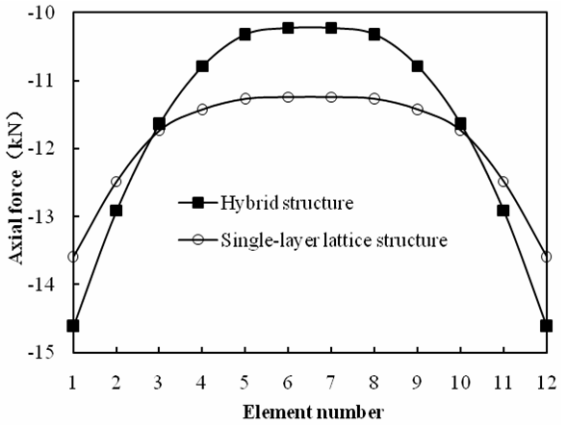

Figure 9. Axial Forces for Typical Members

3.2.2 Dynamic analysis

Modal analyses of two barrel vault structures are carried out, and the natural frequencies of the first thirty modes are plotted in Figure 10. For the first three natural frequencies, it shows little difference between two structures. However, the hybrid barrel vault structure has higher natural frequencies from the fourth mode because the pre-stressed cables result in a higher stiffness of the structure. Hence, the natural frequencies of the system increase.

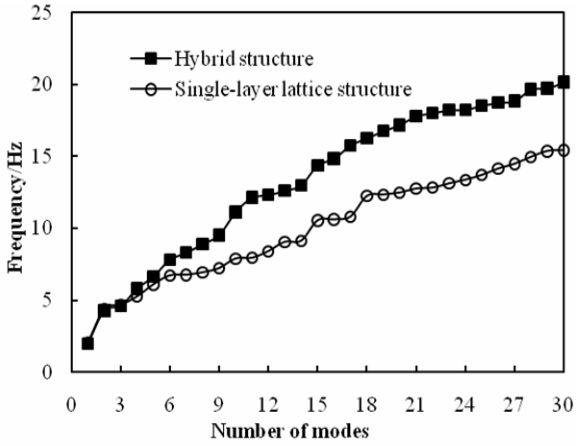

Figure 10. The Natural Frequencies of the First 30 Modes

The criterion of a good design should include a high stiffness of the overall structure thus reducing nodal displacement etc. when fully loaded as well as a higher natural frequency to minimize vibration effects. The results of the static and dynamic analyses have shown that the hybrid structure is a more efficient structural form compared with the single-layer lattice system.

4. PARAMETRIC STUDY OF STRUCTURAL CHARACTERISTICS

The effects of rise-to-span ratios, cross-sections of steel beams, areas of cables, initial cable stresses and anti-symmetric loads on the static and dynamic behavior of the hybrid barrel vault roof are studied.

4.1 Influence of Rise-to-span Ratio

The rise-to-span ratio is an important factor that affects the structural behavior of hybrid systems. By changing the rise of the primary model in 5 cases, five hybrid barrel vault models can be constructed. The axial forces of typical members and the vertical nodal deformations are calculated and shown in Figure 11. For the axial forces of typical members, Figure 11 shows that the higher the rise-to-span ratios, the lower the axial forces will be. However, a similar trend cannot be found for the nodal vertical displacements. If the rise-span ratio is smaller than 0.2, an increase in rise-to-span ratio will result in a decrease in nodal displacements. If the rise-to-span ratio is greater than 0.2, the deformation will increase with the rise-to-span.

Apart from the concerns of the static behavior, changes in the dynamic behavior of hybrid system due to different rise-to-span ratios have also been studied. Modal analyses of the five hybrid structures have been carried out, and the natural frequencies of the first three modes are summarized in Table 1. It shows that when the rise-to-span ratio increases, the natural frequencies of the hybrid barrel vault will decrease.

It can be concluded that there exists an optimal value of rise-to-span ratio for a specific hybrid barrel vault roof to be an effective long-span structural system, because an either too large or too small rise-to-ratio will induce larger nodal displacements. The optimal value of the ratio is found to be between 0.2 and 0.26 from the simulation study presented in this paper.

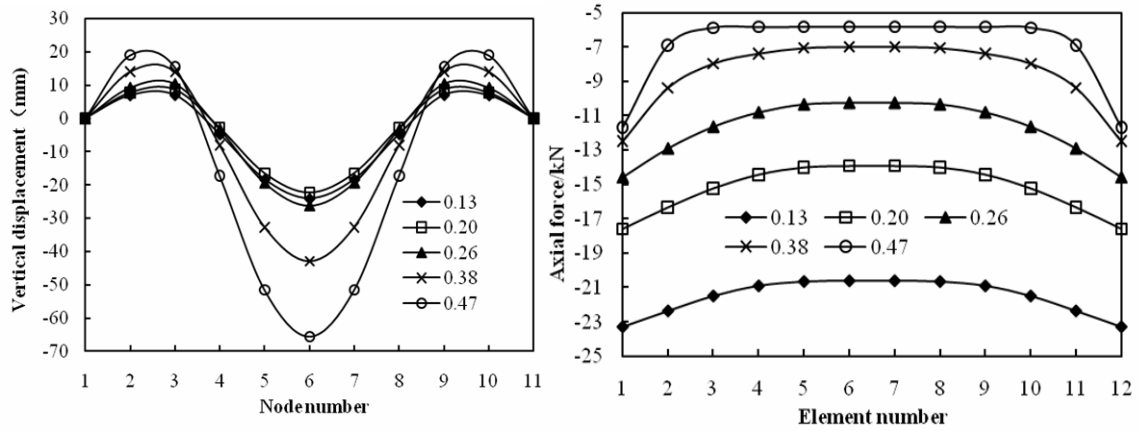

(a) Nodal displacement (b) Axial force of members

Figure 11. Effects of Rise-to-span Ratio on the Structural Behavior

Table 1. The Natural Frequencies (Hz) with Different Rise-to-span Ratios

Rise-to-span ratio	0.13	0.2	0.26	0.38	0.47
First mode	2.2751	2.1974	1.9923	1.5451	1.2481
Second mode	4.7335	4.6033	4.2915	3.5539	3.0076
Third mode	5.1347	4.9729	4.6135	3.7898	3.1899

4.2 Influence of Cross-sections of Steel Beams

A series of analyses have been carried out using the example structure with different cross-sections to study the effect of rigidity of beams on structural behavior. The nodal displacements and axial forces of typical elements with respect to different cross-sections of steel beams are shown in Figure 12 where four cross-sections, 110 mm × 55 mm × 3 mm, 120 mm × 60 mm × 4 mm, 150 mm × 75 mm × 4 mm, 170 mm × 80 mm × 5 mm, are considered in this study.

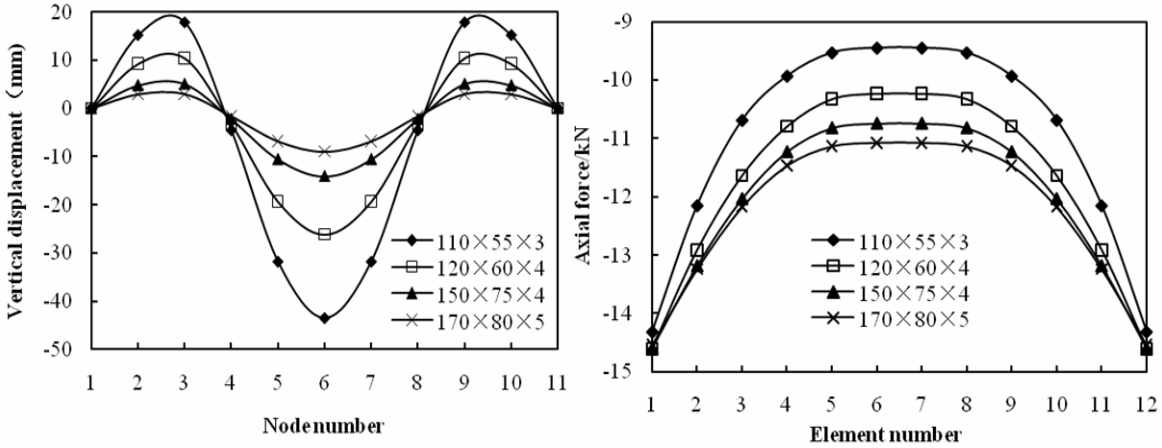

(a) Nodal displacement (b) Axial force of members

Figure 12. Effects of Cross-section of Steel Beams on the Structural Behavior

It can be seen that the vertical displacement reduces significantly when the structure has a larger beam cross-section. When the cross-section increases from 110 mm × 55 mm × 3 mm to 170 mm × 80 mm × 5 mm, the maximal nodal vertical displacement decreases from -43.4 mm to -8.9 mm under an external load only. It can also be found that the axial forces of members also decrease with the increase of the beam cross-section. However, the influence of beam section on axial forces of members is limited.

The natural frequencies of the first three modes for the hybrid structure with different beam sections are given in Table 2. It shows that the natural frequencies increase significantly with the increase of the beam section. It can be concluded that the beam section is very important for stiffening the structure.

Table 2. The Natural Frequencies (Hz) with Different Cross-sections of Steel Beams

Cross-section of steel beams/mm	110×55×3	120×60×4	150×75×4	170×80×5
First mode	1.6589	1.9923	2.681	3.0752
Second mode	3.7407	4.2915	5.6059	6.3571
Third mode	4.044	4.6135	5.997	6.7856

4.3 Influence of Cables

The pre-stresses and areas of cables are also important factors that affect the static and dynamic behavior of the hybrid barrel vault.

4.3.1 Cable area

The typical nodal displacements and axial forces of typical elements under external loads, corresponding to different diameters of cables at a specified pre-stress of 100 MPa are shown in Figure 13. The diameter of cables corresponds to 8 mm, 10 mm, 12 mm, 15 mm and 20 mm in Figure 13, respectively. It can be seen that the influence of cable areas on vertical displacements and axial forces of typical members is very limited. When the area of cables is multiplied by 6.25 (where the diameter of cables increases from 8 mm to 20 mm), the vertical displacement of node 6 and the axial forces of element 6 decrease by about 30 percent.

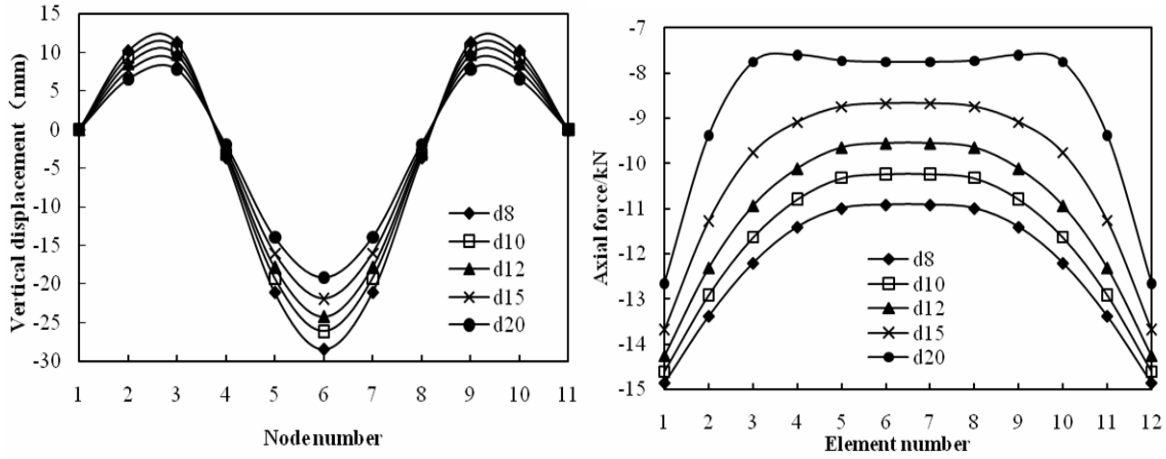

(a) Nodal displacement (b) Axial force of members

Figure 13. Effects of Area of Cables on the Structural Behavior

The natural frequencies of the hybrid structure with different areas of cables are given in Table 3. It can be found that the natural frequencies decrease slightly with the increase of the cable area. This is actually expected since a higher weight will generally result in a lower natural frequency.

Table 3. The Natural Frequencies (Hz) with Different Areas of Cables

Diameter of cables/mm	8	10	12	15	20
First mode	2.0137	1.9923	1.9666	1.9207	1.8297
Second mode	4.3352	4.2915	4.2385	4.1438	3.9552
Third mode	4.6519	4.6135	4.5646	4.4742	4.2881

4.3.2 Cable pre-stress

Different levels of initial stresses are set to 0 MPa, 50 MPa, 100 MPa, 150 MPa, 200 MPa and 300 MPa, respectively. The typical nodal displacements and axial forces of typical elements against the specified cable pre-stresses are shown in Figure 14. It should be noted that the results illustrated in Figure 14 are obtained from Phase III of the method described in Section 3.2.1. It shows that the differences in vertical nodal displacements among the hybrid structures due to different pre-stress values of the cable are very small. However, the model with zero initial stress gives highest nodal displacements. It should be noted that the cable prestress will have small effect when it is between 0MPa and 50MPa, so there is a step change between these two curves. However, when the cable prestress is 50MPa, the axial force of the cable is very small, so the smaller cable prestresses, such as 10MPa, 20MPa, were not considered by the authors. Moreover, when the cable prestress is under 50MPa, the cable may be slack under temperature loads.

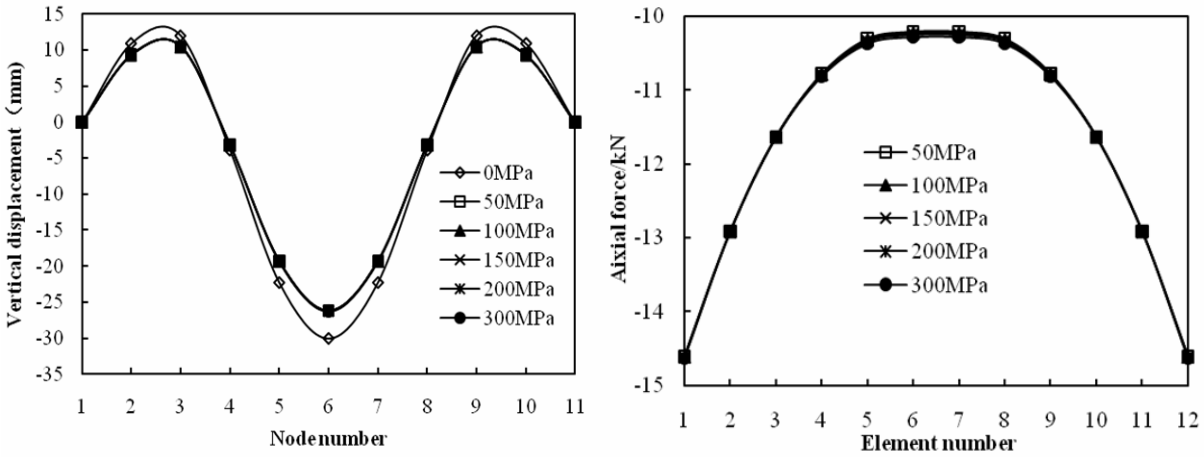

(a) Nodal displacement (b) Axial force of members

Figure 14. Effects of Cable Pre-stress on the Structural Behavior

Table 4. The Natural Frequencies (Hz) with Different Cable Pre-stress

Cable pre-stress/MPa	50	100	150	200	300
First mode	1.9941	1.9923	1.9888	1.9853	1.9783
Second mode	4.294	4.2915	4.2846	4.2776	4.2637
Third mode	4.6079	4.6135	4.6085	4.6035	4.5935

It can also be seen from Figure 14 that the increase of cable pre-stress leads to a very slight rise of axial forces of typical elements. However, from the method described in Section 3.2.1, it should be noted that the axial forces given in Figure 14 are only resulted from an external load. If both the pre-stress and external loads are considered, a higher pre-stress will result in a higher member force. Thus, it is not an economical way to improve the structural behavior simply by increasing the level of pre-stress only.

Modal analyses of the hybrid structure with different areas of cables have been carried out, and the natural frequencies of the first three modes are given in Table 4. It can be found that differences in natural frequencies among the five cases are very small.

4.4 Influence of Anti-symmetrical Load

Another factor to be considered in this study is the anti-symmetrical load. One type of anti-symmetrical load is the half-span load which can be induced during construction or by snow. The anti-symmetrical load case $g+s/2$ (dead load+ snow load on half span of the structure) is considered in this study. The symmetrical load case is denoted as Load 1, and the anti-symmetrical load case Load 2.

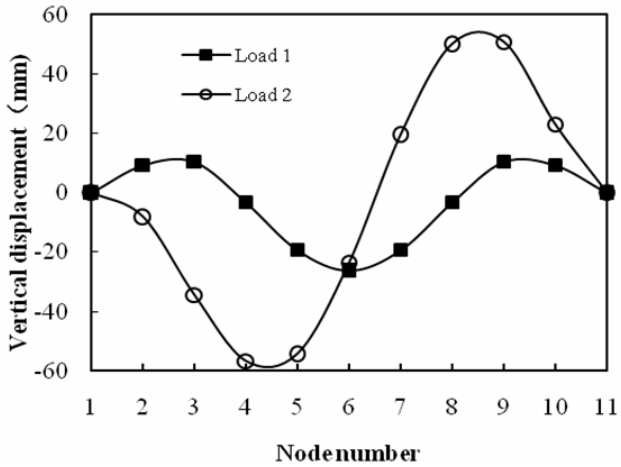

Figure 15. Effects of Anti-symmetrical Loads on the Nodal Vertical Displacement

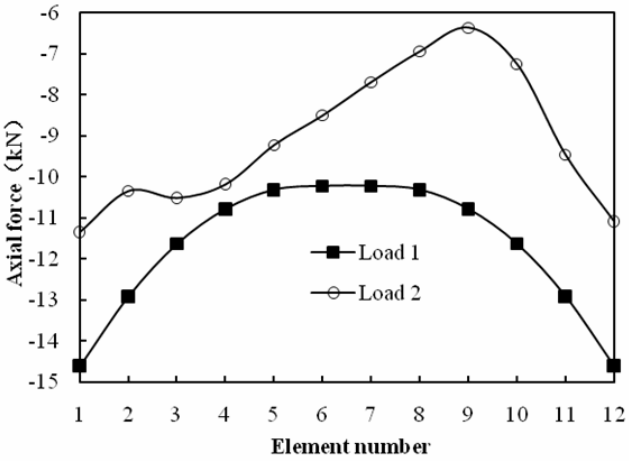

Figure 16. Effects of Anti-symmetrical Loads on the Axial Forces of Elements

The vertical nodal displacements of the hybrid structure under two load cases are given in Figure 15. It shows the anti-symmetrical distribution of load imposes very large effect on the vertical nodal displacement. The vertical displacements under Load 2 are larger than Load 1, and the deformed shapes are different as shown in Figure 15. Figure 16 shows the axial forces of elements under both symmetrical and anti-symmetrical load cases. It can be seen that the axial forces are smaller than those from full-span load, and are unevenly distributed along the span.

5. CONCLUSIONS

The mechanical characteristic of the hybrid structure was investigated based on a quadrangle of slats with cross cables. Comprehensive static and dynamic analyses were carried out on the hybrid barrel vault and the single-layer reticulated shell. Then a numerical parametric analysis of the hybrid structure was performed. Based on the results, the following conclusions are drawn:

1. Cables will increase the structural stiffness of the four-beam element. Moreover, the structural stiffness is dependent on the included angle θ. It initially decreases with the increase of the include angle and then increases afterwards.

2. Introducing cables, causes the hybrid system, when compared with the single-layer reticulated shell, to acquire smaller structural deformations, lower member forces, and higher natural frequencies.

3. Hybrid barrel vaults have high stiffness given the rise-to-span range of 0.20-0.26 and consequently possess good dynamic performance. For different loading conditions, the optimal rise-to-span ratio of hybrid barrel vaults may be different from above ratios.

4. Cross-sections are one of the most important factors influencing the static and dynamic behavior of the hybrid structure. In order to achieve excellent performance, it is very important to stiffen the structure, and thus reduce nodal displacements and member forces, yielding higher natural frequencies. However, adjusting both the areas and pre-stress of cables are not effective method for improving the structural behavior.

5. The static behavior of a hybrid barrel vault is sensitive to the anti-symmetrical distribution of load. The anti-symmetric load increases the nodal displacements and reduces the axial forces of members.

ACKNOWLEDGEMENTS

The work presented in this article was supported by the National Natural Science Foundation of China (Grant No. 50478075), Jiangsu “Six Top Talent” Program of China (Grant No.07-F-008), a Project Funded by the Priority Academic Program Development of Jiangsu Higher Education Institutions and Scientific Research Foundation of Graduate School of Southeast University (Grant No. YBJJ0817). The first author would like to thank the China Scholarship Council for sponsoring his stay at the California Institute of Technology.

REFERENCES

[1] Bulenda, T. and Knippers, J., “Stability of Gird Shells”, Computers & Structures, 2001, Vol. 79, pp. 1161-1174.
[2] El-Sheikh, A., “Configurations of Single-Layer Barrel Vaults”, Advances in Structural Engineering, 2001, Vol. 4, No. 2, pp. 53-64.
[3] El-Sheikh, A., “Performance of Single-layer Barrel Vaults with Different Configurations”, International Journal of Space Structures, 2001, Vol. 16, No. 2, pp. 111-123.
[4] El-Sheikh, A., “Effect of Geometric Imperfections on Single-layer Barrel Vaults”, International Journal of Space Structures, 2002, Vol. 17, No. 4, pp. 271-283.
[5] Hanaor, A., “Design and Behaviour of Reticulated Spatial Structural Systems”, International Journal of Space Structures, 1995, Vol. 10, No. 3, pp. 139-149.
[6] Makowski, Z.S., “Analysis, Design and Construction of Braced Barrel Vaults”, Elsevier Applied Science Publishers, London, 1985.
[7] Manning, M.W. and Dallard, P., “Lattice Shells: Recent Experiences”, The Structural Engineer, 1998, Vol. 76, No. 2, pp. 105–110.

[8] Hosozawa, O., Shimamura, K. and Mizutani, T., “The Role of Cables in Large Span Spatial Structures: Introduction of Recent Space Structures with Cables in Japan”, Engineering Structures, 1999, Vol. 21, pp. 795-804.
[9] Saitoh, M. and Okada, A., “The Role of String in Hybrid String Structures”, Engineering Structures, 1999, Vol. 21, pp. 756-769.
[10] Xue, W. and Liu, S., “Studies on a Large-Span Beam String Pipeline Crossing”, Journal of Structural Engineering, 2008, Vol. 134, No. 10, pp. 1657-1667.
[11] Xue, W. and Liu, S., “Design Optimization and Experimental Study on Beam String Structures”, Journal of Constructional Steel Research, 2009, Vol. 65, pp. 70-80.
[12] Kitipornchai, S., Kang, W., Lam, H.F. and Albermani, F., “Factors Affecting the Design and Construction of Lamella Suspen-dome Systems”, Journal of Constructional Steel Research, 2005, Vol. 61, pp. 764-785.
[13] Kang, W., Chen, Z., Lam, H.F. and Zuo, C., “Analysis and Design of the General and Outmost-ring Stiffened Suspen-dome Structures”, Engineering Structures, 2003, Vol. 25, pp. 1685-1695.
[14] Schlaich, J. and Schober, H., “Glass-covered Gird-shells”, Structural Engineering International, 1996, Vol. 6, pp. 88-90.
[15] Schlaich, J. and Schober, H., “Glass Roof for the Hippo House at the Berlin Zoo”, Structural Engineering International, 1997, Vol. 7, pp. 252-254.
[16] Schlaich, J., “Concept Design of Light Structures”, Journal of the International Association for Shell and Spatial Structures, 2004, Vol. 45, pp. 157-168.
[17] Schlaich, J. and Schober, H., “Recent Glass Roofs”, Journal of the International Association for Shell and Spatial Structures, 1999, Vol. 40, pp. 193-205.
[18] Harris, R., Romer, J., Kelly, O. and Johnson, S., “Design and Construction of the Downland Gridshell”, Building Research & Information, 2003, Vol. 31, No. 6, pp. 427-454.
[19] Glymph, J., Shelden, D., Ceccato, C., Mussel, J. and Schober, H., “A Parametric Strategy for Free-form Glass Structures Using Quadrilateral Planar Facets”, Automation in Construction, 2004, Vol. 13, pp. 187-202.
[20] Paoli, C., “Past and Future of Grid Shell Structures”, Massachusetts Institute of Technology, 2007.

COMPRESSIVE PERFORMANCES OF THE CONCRETE FILLED CIRCULAR CFRP-STEEL TUBE (C-CFRP-CFST)

Y. Che [1], Q.L. Wang [2,*] and Y.B. Shao [3]

[1] *Ph. D. Student, School of Civil Engineering, Shenyang Jianzhu University, Shenyang, P. R. China; School of Civil Engineering, Dalian University of Technology, Dalian, P. R. China*
[2] *Professor, School of Civil Engineering, Shenyang Jianzhu University, Shenyang, P. R. China*
[3] *Associate Professor, School of Civil Engineering, Yantai University, Yantai, P. R. China*
**(Corresponding author: E-mail: ceqlwang@sjzu.edu.cn)*

Received: 25 July 2011; Revised: 7 December 2011; Accepted: 14 December 2011

ABSTRACT: This paper presents the results of axial compressive tests of the concrete filled circular CFRP-steel tubular (C-CFRP-CFST) stub columns. The test results showed that the CFRP jackets enhanced the load bearing capacity of the stub columns effectively. Enhancement of the columns' stiffness due to the CFRP jackets was also observed. Also, the steel tube and the CFRP tube work concurrently before failure. A constitutive relationship suitable for concrete confined by circular CFRP-steel composite tube was proposed, and a finite element model was established by using ABAQUS for analyzing load-deformation relationship of the composite stub columns and it shows that the results predicted check well with that of the test and were on the safe side. Analysis based on ABAQUS indicates that, outer tube of the C-CFRP-CFST stub columns can provide confinement force for concrete core even during initial loading period. Additionally, the initial stress in the steel tube can postpone the mutual reaction between the steel tube and the concrete, while it has a little influence on the peak value of the confinement force; adhesive strength has little effect on compressive performances of the stub columns. Finally, the index and parametric expression of load bearing capacity of the C-CFRP-CFST stub columns were proposed, and the proposed equations can be used to calculate the load bearing capacity reasonably.

Keywords: Circular CFRP-steel tube, In-filled concrete, Stub columns, Compressive performances, Confinement force, Load bearing capacity

1. INTRODUCTION

Concrete filled steel tube (hereinafter referred to CFST) structures were adopted more and more widely in industry building, high-rising building, bridge structures and so on due to the advantage of high strength for tri-axially compressed concrete, and excellent effects were obtained (Han [1]; Tao et al. [2]; Georgios and Lam [3]; Uy [4]). On the other hand, Fiber Reinforced Plastic (hereinafter referred to FRP) is characterized by its high strength to weight ratio, high corrosion resistance, and ease of installation, and was used more and more in structural engineering, in which FRP confined (reinforced) concrete is one of the typical styles and it includes two kinds of applications: one is casting concrete into pre-fabricated FRP tube to form a members for carrying load, the other is by wrapping FRP externally around members to strengthen or repair existing (reinforced) concrete structures (Wang and Restrepo [5]; Teng et al. [6]).

FRP-metal (steel, iron and so on) composite tank/tube also used in other engineering fields. Figure 1 (a) shows a gas tank used in motor vehicle, and its inner shell is made of steel and outer shell is made of Carbon Fiber Reinforced Plastic (hereinafter referred to CFRP), which utilize rigidity and strength of the steel and tensile strength of the CFRP; Figure 1 (b) shows pipeline system for transporting high pressure gas/liquid usually used in municipal engineering or chemical engineering, and its inner tube is made of steel or iron, and outer tube is made of Glass Fiber Reinforced Plastic (hereinafter referred to GFRP), which also use rigidity and strength of the metal materials and tensile strength of the GFRP, additionally, wrapping FRP externally around the tube is beneficial to corrosion resistance of the pipe. Figure 1 (b) has another form: wrapping CFRP on the outer surface of the tube to repair corroded metallic tubes that have fulfilled function for a long

term, its cost is much lower than that of rebuilding a new set of pipeline system. There are many these kinds of engineering in P. R. China.

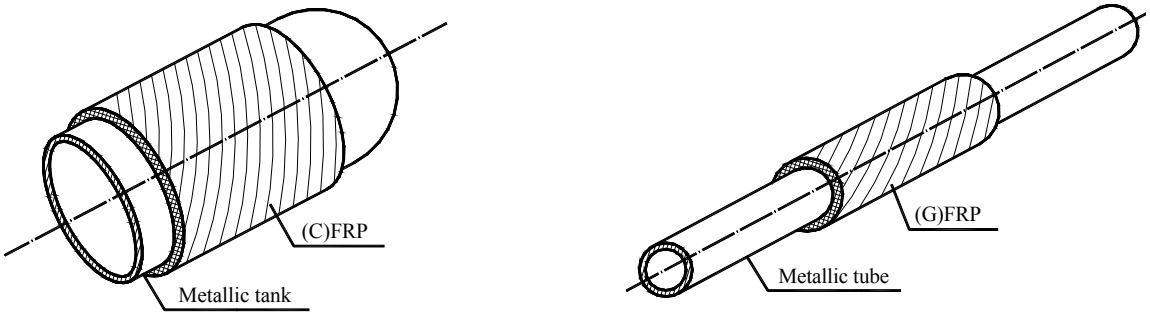

(a) Gas Tank (b) Municipal/Chemical Industry Pipeline

Figure 1. FRP-metal Composite Tank/Tube Used in Engineering Practice

Therefore, it is believed that CFRP-metal composite tube also can be used in civil engineering, for example, casting concrete into pre-fabricated CFRP-steel tube to form members which are mainly subjected to compression (Wang, Guan and Zhao [7]), or it is necessary to reinforce, repair or strengthen the existed CFST structures, which are needed to add new functions or have slight damage, by using CFRP (Tao, Han and Zhuang [8]). The two reinforcements can both form the so-called concrete filled CFRP-steel tubular (hereinafter referred to as CFRP-CFST) structures.

Similarly to CFST, CFRP-CFST can take advantage of the tri-axial compressed concrete sufficiently, meanwhile, it can avoid local buckling of the steel tube and has higher load bearing capacity and better durability, also, combination of the CFRP and the steel tube can remedy the defect of abrupt failure of the CFRP confined (reinforced) concrete, and it is a good choice for repairing or strengthening CFST structures that has fulfilled function for a long time or damaged slightly.

However, it is well known that FRP composites have limited fire resistance because of the low transition temperature of their epoxy resins. Until the high temperature mechanical properties of the FRP materials are improved significantly, it is believed that FRP materials will perform poorly in fires, and thus result in unsatisfactory fire endurance for FRP-steel-concrete composite structural members. From fire experiments reported in the literature (Han [9]) however, it appears that CFRP-CFST have demonstrated satisfactory fire endurance under load when supplemental insulation to the FRP composites has been applied. Therefore, FRP composites are apt to be used as strengthening materials only provided they are properly designed.

Studies on CFST structures mainly focus on concrete filled circular steel tube (hereinafter referred to C-CFST) and concrete filled square steel tube (hereinafter referred to S-CFST). Similarly, the studies on CFRP-CFST structures also focus on concrete filled circular CFRP-steel tube (hereinafter referred to as C-CFRP-CFST, Figure 2) and concrete filled square CFRP-steel tube (hereinafter referred to as S-CFRP-CFST).

There are some research studies in this field in the literature. Research of using CFRP to repair CFST structures after exposed to fire were conducted (Tao, Han and Zhuang [10]). A new C-CFST column system, where CFRP composites were used as additional confinement to the potential plastic hinge regions of the composite column was proposed (Xiao, He and Choi [11]), also, a simplified analytical solution in association with a numerical computer program of the CFRP-CFST

column system was developed, and the accuracy of the analytical solution was verified by providing comparisons with existing experimental results and the finite element analysis, but the estimated behaviors of the column system after yielding did not follow the behavior of experimental results (Choi and Xiao [12]).

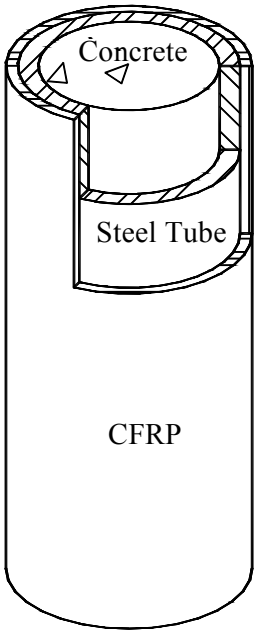

Figure 2. General View of C-CFRP-CFST

In order to understand the compressive performances of the C-CFRP-CFST members theoretically further, in this paper, on the basis of experimental investigation, the whole process stress-strain curves of C-CFRP-CFST stub columns under compressive load are simulated by using finite element software ABAQUS. Furthermore, the confinement effect provided by CFRP for the C-CFST stub columns are analyzed; also, the stress and strain distributions for materials are discussed respectively. Influences of initial stress in the steel tube on the stub columns are investigated. Additionally, influences of adhesive strength between the steel tube and the concrete on stub columns are discussed. Finally, index and parametric equations of the load bearing capacity for the C-CFRP-CFST stub columns are proposed.

2. EXPERIMENTAL PROGRAM

2.1 General

Fifteen specimens, including ten C-CFRP-CFST stub columns and five C-CFST stub columns, were tested. Specimen details are provided in Table 1.

In Table 1, specimens designations starting with CSC refer to Circular Stub Columns, the next letter A, B, C, D and E indicating wall thickness of the steel tube (t_s) are of 1.5mm, 2.5mm, 3.5mm, 4.5mm and 6mm respectively, the last cipher 0, 1 and 2 refer to number of layer(s) of the CFRP (m). The length of the stub columns (L) was chosen to be three times of the outer diameter of the steel tube (D_s). Due to limitation of experimental conditions, the size of the steel tube (D_s) is relatively smaller. This is reasonable since the experimental results are mainly used to verify the accuracy of the proposed theoretical and numerical models. However, full-scale specimens are necessary to be tested in the future work for practical purposes.

Table 1. Specimen Labels and Member Capacities

No.	Specimens label	D_s (mm)	t_s (mm)	L (mm)	m (layer (s))	f_{ck} (MPa)	$\varepsilon_{cf\theta r}'$ (με)	DI	N_u^e (kN)	$E_{cfsce}A_{cfsc}$ (10^3kN)	r (%)
1	CSC A-0	127	1.5	381	0	36.2	-	12.9	866	499	0
2	CSC B-0	129	2.5	387	0	36.2	-	10.5	990	621	0
3	CSC C-0	131	3.5	393	0	36.2	-	11.7	1219	765	0
4	CSC D-0	133	4.5	399	0	36.2	-	13.0	1301	899	0
5	CSC E-0	136	6.0	408	0	36.2	-	14.8	1493	1101	0
6	CSC A-1	127	1.5	381	1	36.2	4124	3.8	1018	628	17.6
7	CSC B-1	129	2.5	387	1	36.2	6370	7.4	1186	745	19.8
8	CSC C-1	131	3.5	393	1	36.2	1780	9.3	1406	774	15.3
9	CSC D-1	133	4.5	399	1	36.2	5499	12.6	1559	884	19.8
10	CSC E-1	136	6.0	408	1	36.2	7163	12.3	1891	1192	26.7
11	CSC A-2	127	1.5	381	2	36.2	6035	2.6	1228	659	41.8
12	CSC B-2	129	2.5	387	2	36.2	8008	3.5	1384	761	39.9
13	CSC C-2	131	3.5	393	2	36.2	7044	5.0	1714	744	40.6
14	CSC D-2	133	4.5	399	2	36.2	3380	5.6	1865	834	43.4
15	CSC E-2	136	6.0	408	2	36.2	6132	9.2	2105	1145	41

2.2 Material Properties

Seamless steel tube was used. Tensile tests on steel coupons cut from the original steel tubes were conducted. The measured properties of the steel tubes obtained from these tests are given in Table 2, where E_s, f_y, ε_{sy}, v_s, f_u and δ_s are elasticity modulus, yield strength, yield strain, elasticity Poisson' ratio, ultimate strength and elongation percentage of the steel tube, respectively.

Table 2. Material Properties of the Steel Tube

E_s (GPa)	f_y (MPa)	ε_{sy} (%)	v_s	f_u (MPa)	δ_s (%)
203	330	0.17	0.28	462	12.8

All the specimens were cast with one type of concrete. In all the concrete mixture, Portland cement was used, and the fine aggregate used was silica-based sand. The course aggregate was limestone with the largest size of 20mm, and 1% (in weight) water reducing agent was added. The mixture proportions of the concrete are summarized in Table 3.

Table 3. Mixture Proportions of Concrete (kg / m^3)

Cement	Water	Sand	Course aggregate
490	172	662	1078

To determine the compressive strength of the resulting concrete, six 150 mm cubes were cast and cured in conditions similar to that of the related specimens. The average cubic strength (f_{cu}) at 28 days was 54 MPa. Elasticity modulus of the concrete (E_c) was 34.5GPa, and Poisson's ratio of the concrete (v_c) was 0.22. Thus the designed axial compressive strength of the concrete (f_{ck}) is determinated by follow and listed in Table 1

$$f_{ck}=0.67f_{cu} \tag{1}$$

Carbon fiber sheet used is made in EPO Company, Germany, which is a kind of high quality one-way sheet fabricated with TORAY T 700 12K that made in Japan, the tensile properties of the CFRP, determined from tensile tests of six flat coupons (Figure 3), are given in Table 4, in which f_{cf}', E_{cf}, δ_{cf} and w_{cf} are tension strength, elasticity modulus, elongation percentage and unit weight of the carbon fiber sheet, and t_{cf} is thickness of 1 layer carbon fiber sheet.

Table 4. Main Technical Properties of the Carbon Fiber Sheets

Model number	f'_{cf} (GPa)	E_{cf} (GPa)	δ_{cf} (%)	w_{cf} (gm^{-2})	t_{cf} (mm)
C300/300	4.5	228	1.98	300	0.167

JGN-C, a kind of epoxy resin used for building structures that produced by Building Science Research Institute of Liaoning Province, P. R. China, was used for adhering the CFRP to the steel tube, another epoxy resin, JGN-P was adopted for gluing CFRPs together.

Figure 3. Typical Failed CFRP Coupon

2.3 Specimen Preparations

In preparing the C-CFST specimens, the concrete was filled in layers and was vibrated by a poker vibrator. These specimens were then placed upright to air-dry until testing. Prior to testing, the top surfaces of the C-CFST specimens were ground smooth and flat, using a grinding wheel. A steel plate with a thickness of 20 mm was then welded to the top of each of the specimens.

Carbon fiber sheets were applied using a hand lay-up method. The finishing end of a sheet overlapped the starting end by 150 mm.

2.4 Test Setup and Instrumentation

A 5000 kN capacity testing machine was used for the compression tests on all specimens. Eight strain gauges, including four in the longitudinal direction and another four in the circumferential direction, mounted on the steel tube surface of each specimen, were used to measure longitudinal strain of the steel tube (ε_{sl}) and circumferential strain of the steel tube ($\varepsilon_{s\theta}$) at the mid-height cross-section, respectively. Also, four strain gauges in the circumferential direction, mounted on the CFRP surface of each specimen, were used to measure circumferential strain of the CFRP ($\varepsilon_{cf\theta}$) at the mid-height cross-section. Two Linear Variable Displacement Transducers (LVDTs) were used to measure axial shortening of the specimens (Δ) during the tests. UCAM70A was used for data logging. Test arrangement is shown in Figure 4.

To assure uniform compression, preliminary tests within the elastic range were conducted by carefully adjusting the position of the specimen, based on the measurements of the strain gauges attached at the mid-height cross-section of the test specimen. The adjustment was terminated when the difference between the measured strain and the average value was no more than 5%. A load interval of less than one tenth of the estimated load capacity was used. Each load interval was maintained for about 2 to 3 min.

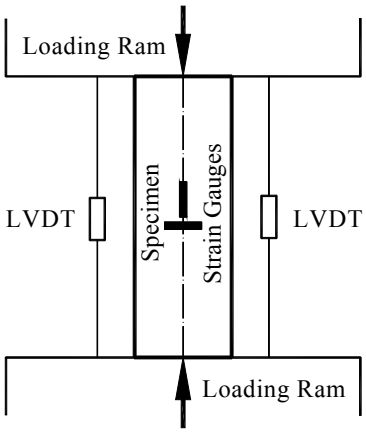

Figure 4. Test Arrangement

2.5 Test Observations and Failure Models

For C-CFRP-CFST columns, during the initial loading stage, in general, the axial load (N) is approximately proportional to the axial strain. There is no obvious change in the appearance of the specimens. The epoxy layers began to peel when the load attained 50% of the maximum load in the pre-peak stage. Almost all the epoxy layers spalled off when the load attained 70% of the maximum load. Local buckling occurred when the load attained 80% of the maximum load. After their peak loads had been attained, the specimens exhibited a sudden failure as a result of the rupture of CFRP jackets at mid-height cross-section. In each series, the more layers of CFRP used, the more sudden the failure was. Several specimens after loading are shown in Figure 5.

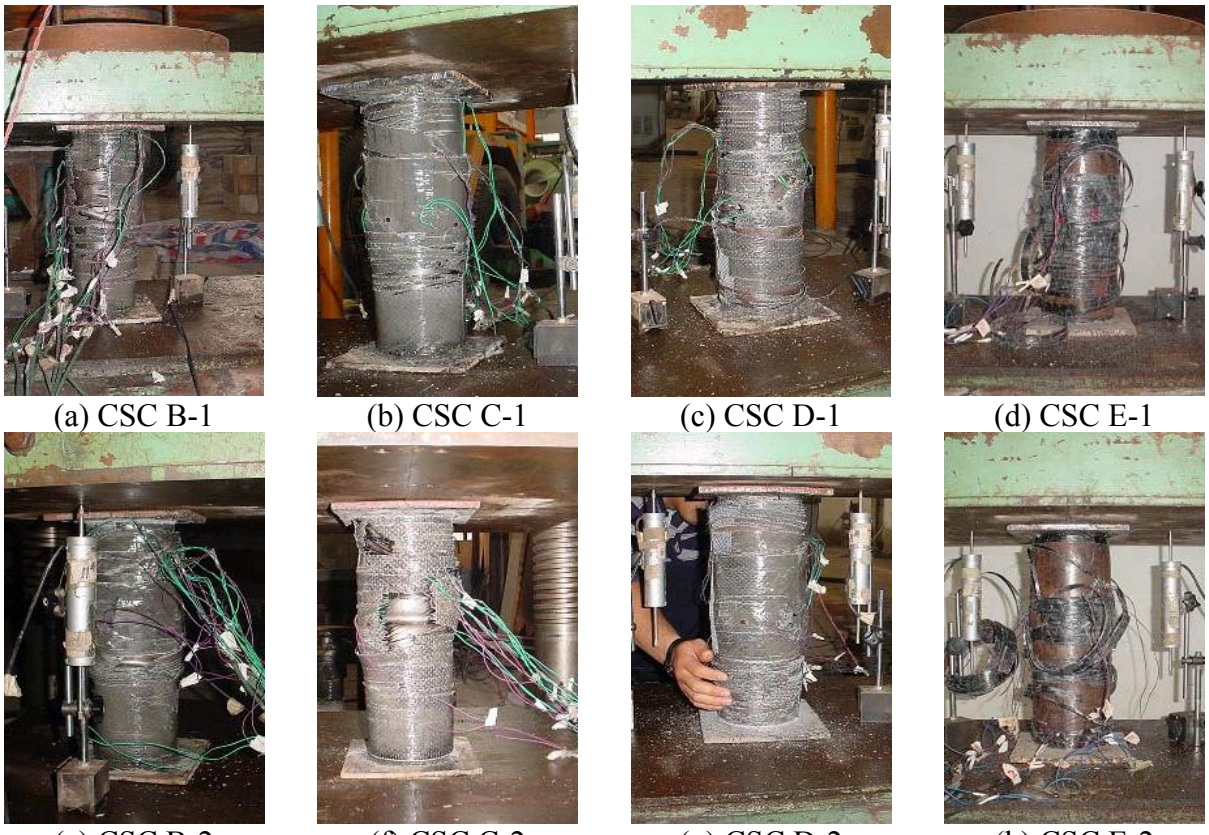

(a) CSC B-1 (b) CSC C-1 (c) CSC D-1 (d) CSC E-1

(e) CSC B-2 (f) CSC C-2 (g) CSC D-2 (h) CSC E-2

Figure 5. Several Specimens after Loading

2.6 Test Results and Analysis

2.6.1 Stress-strain curves

The tested nominal compression stress versus longitudinal strain (ε) curves of the specimens are shown in Figure 6. For C-CFST specimens, nominal compression stress $\sigma_{sc}=N/A_{sc}$, in which A_{sc} is cross-sectional area of the C-CFST specimens, $A_{sc}=A_s+A_c$, A_s and A_c are cross-sectional area of the steel tube and the concrete respectively; while for C-CFRP-CFST specimens, nominal compression stress $\sigma_{cfsc}=N/A_{cfsc}$, A_{cfsc} is cross-sectional area of the C-CFRP-CFST specimens, $A_{cfsc} \approx A_{sc}$, cross-sectional area of the CFRP ($A_{cf\theta}$) is ignored here. The value of ε is identical to the value of ε_{sl} before failure of the gauges mounted on the surface of the steel tube, while the value of ε can be obtained from Δ after failure of the gauges.

Figure 6 indicates that, for C-CFRP-CFST specimens, when σ_{cfsc} is small, ε is small too and approximately proportional to σ_{cfsc}. When σ_{cfsc} reached about 60-70% of the maximum value, ε started to increase significantly. It means that there is an increasing stage from the end point of the elasticity to the maximum σ_{cfsc} in the stress versus longitudinal strain curves, which is different from such curves of C-CFST specimens. After the maximum σ_{cfsc} was reached, σ_{cfsc} started to decrease. There is a decreasing stage in the stress versus longitudinal strain curves due to the fracture of the CFRP, which is also different from such curves of C-CFST specimens. The rest of the curve is similar to that of the corresponding C-CFST specimens. Additionally, the maximumσ_{cfsc} as well as the corresponding maximum compressive strain of the C-CFRP-CFST specimens has some increase with more layers of CFRP.

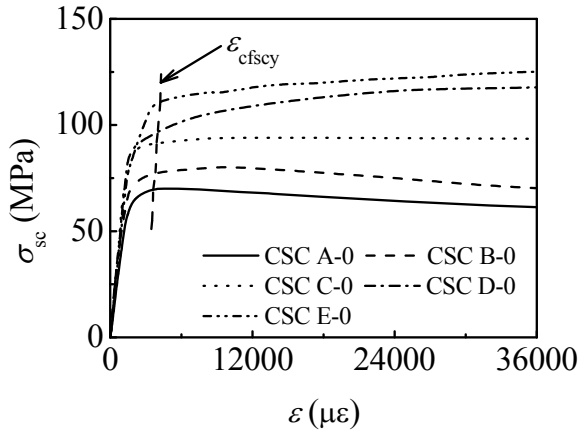

(a) m=0

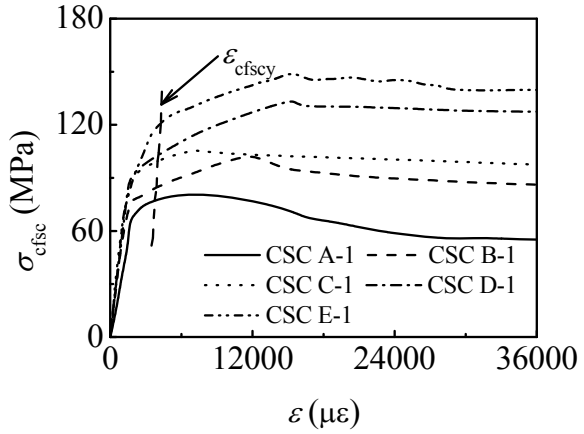

(b) m=1

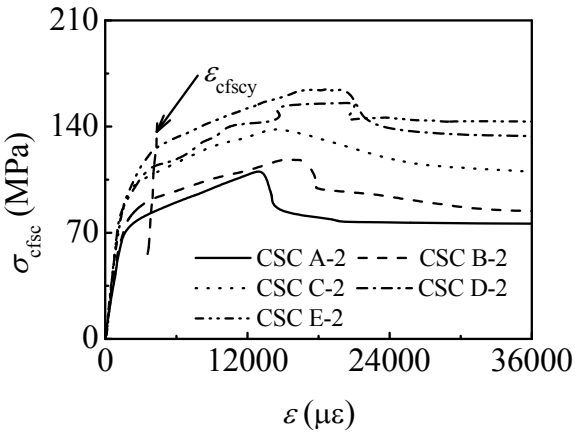

(c) m=2

Figure 6. Tested Nominal Compression Stress versus Longitudinal Strain Curves of the Specimens

2.6.2 Cooperation between steel tube and CFRP

Figure 7 illustrates the tested axial load (N) versus circumferential strain (ε_θ) curves for C-CFRP-CFST stub columns. It can be seen from Figure 7 that $\varepsilon_{s\theta}$ and $\varepsilon_{cf\theta}$ are the same approximately from initial stage of loading till the CFRP rupturing, and it means that wrapping CFRP in accordance with the procedure used in this paper would ensure the steel tube and the CFRP work concurrently before failure.

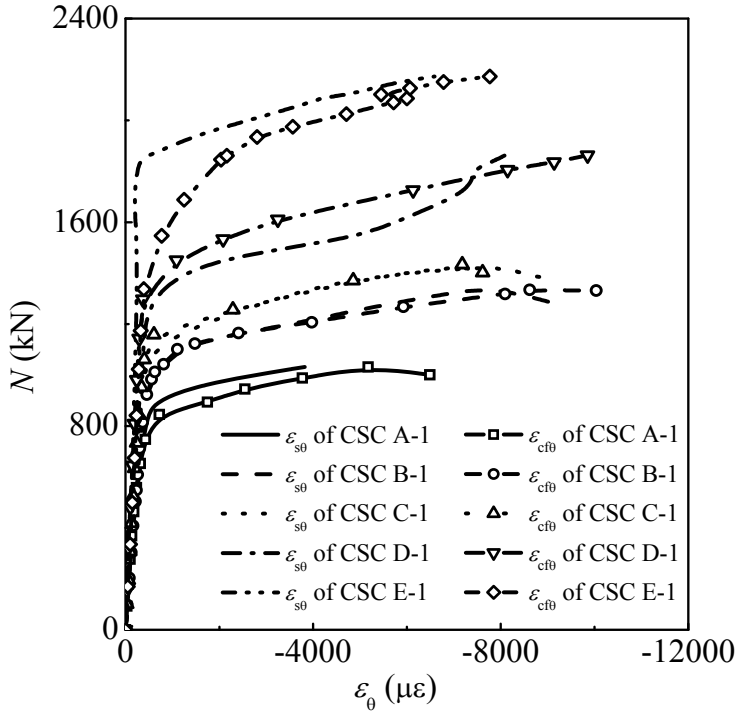

(a) m=1

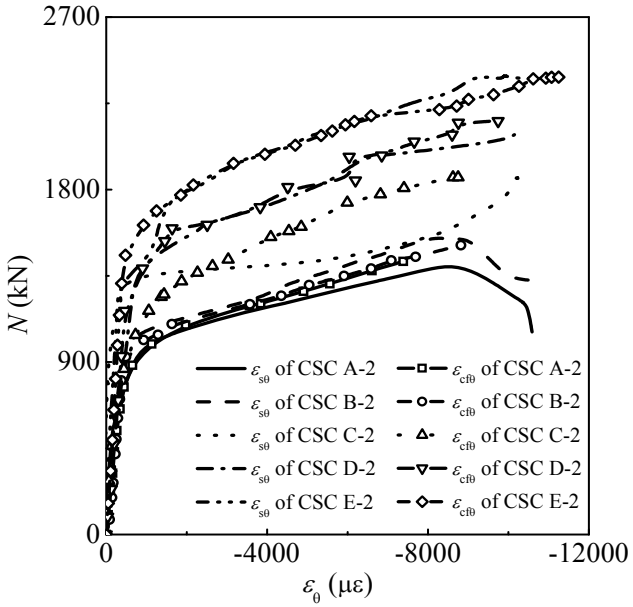

(b) m=2

Figure 7. N versus ε_θ Curves for C-CFRP-CFST Stub Columns

2.6.3 Ductility

In order to quantify the effect of CFRP jackets on section ductility, a ductility index (DI) (Tao, Han and Wang [13]) is used:

$$DI=\varepsilon_{85\%}/\varepsilon_y \tag{2}$$

$$\varepsilon_y=\varepsilon_{75\%}/0.75 \tag{3}$$

where $\varepsilon_{85\%}$ is the longitudinal strain when the load falls to 85% of the maximum load, and $\varepsilon_{75\%}$ is the longitudinal strain when the load attains 75% of the maximum load in the pre-peak stage.

The ductility indices are given in Table 1 and plotted in Figure 8 for all specimens, where ξ_{cf} is confinement factor of the CFRP (Wang, Guan and zhao [7])

$$\xi_{cf}=A_{cf\theta}f_{cf\theta}/(A_c f_{ck}) \tag{4}$$

in which $f_{cf\theta}$ is the ultimate tensile strength of the CFRP, and

$$f_{cf\theta}=E_{cf}\varepsilon_{cf\theta r} \tag{5}$$

where $\varepsilon_{cf\theta r}$ (=5500με) is the average value of the fracture strains ($\varepsilon_{cf\theta r}'$) of CFRP on all C-CFRP-CFST specimens, $\varepsilon_{cf\theta r}'$ is obtained from the strain gauges glued on the CFPR of all the C-CFRP-CFST specimens and listed in Table 1.

It should be noted that rupture strain value of the CFRP mounted on the specimens is not the same as that of coupon tests as listed in Table 4 (δ_{cf}=1.98%, 19800με), this deviation is perhaps due to the different curvature of the CFRPs (Yu et al. [14]), and the real reason should be investigated in the future. $\varepsilon_{cf\theta r}$ was used later for finite element modelling and calculation of the load bearing capacity.

It can be seen from Figure 8 that the ductility of the C-CFRP-CFST specimens generally decreases with the increasing of confinement factor of the CFRP. This can be attributed to the abrupt rupture of CFRP jackets. The more layers of CFRP jacket used, the more abrupt the failure.

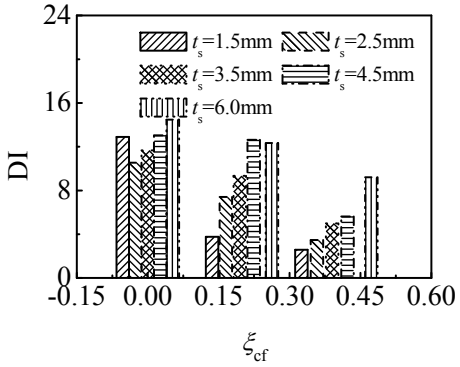

Figure 8. Ductility Index

3. FE SIMULATION

3.1 Stress-Strain Relationship of the Materials

3.1.1 Steel

A 5-stages stress-strain relationship of steel (Han, Yao and Tao [15]) is used here.

3.1.2 Concrete

For concrete confined by circular CFRP-steel tube under compression, stress-strain property is given based on experimental investigation as well as considering corresponding reported research about concrete confined by circular steel tube under compression (Wang, Zhu and Gao [16]) as follow

$$\sigma_{cl}/\sigma_0=\begin{cases}2(\varepsilon_{cl}/\varepsilon_0)-(\varepsilon_{cl}/\varepsilon_0)^2 & & (\varepsilon_{cl}\le\varepsilon_0)\\ \left[1-q+q(\varepsilon_{cl}/\varepsilon_0)^{0.1\xi}\right](\varepsilon_{cl}/\varepsilon_0)^C & (\xi_s\ge 1.12) & (\varepsilon_0<\varepsilon_{cl}\le\varepsilon_u)\\ \dfrac{(\varepsilon_{cl}/\varepsilon_0)^{1+D}}{\beta(\varepsilon_{cl}/\varepsilon_0-1)^2+\varepsilon_{cl}/\varepsilon_0} & (\xi_s<1.12) & (\varepsilon_0<\varepsilon_{cl}\le\varepsilon_u)\\ \dfrac{\varepsilon_{cl}/\varepsilon_0}{\beta_s(\varepsilon_{cl}/\varepsilon_0-1)^2+\varepsilon_{cl}/\varepsilon_0} & & (\varepsilon_{cl}>\varepsilon_u)\end{cases} \quad (6)$$

Where σ_{cl} is longitudinal stress of the concrete; σ_0 is the ultimate compressive stress of the concrete, ε_{cl} is longitudinal strain of the concrete and ε_0 is the ultimate compressive strain of the concrete. q is a quantity related to total confinement factor ξ (Wang, Guan and zhao [7]); C and D are all coefficients; β is a quantity related to ξ before fracture of the CFRP; β_s is a quantity related to ξ_s; ξ_s is confinement factor of the steel tube (Han, Yao and Tao [15]); ε_u is the longitudinal strain of the specimen (ε) when CFRP is fractured, and

$$\sigma_0=f'_c(\text{MPa}) \quad (7)$$

$$\varepsilon_0=\varepsilon_{cc}+(600+32.4f'_c)\xi^{0.2}\times10^{-6} \quad (8)$$

$$\varepsilon_{cc}=(1300+12.09f'_c)\times10^{-6} \quad (9)$$

$$q=\xi^{0.745}/(2+\xi) \quad (10)$$

$$\xi=\xi_s+\xi_{cf} \quad (11)$$

$$C=\xi'(2.231-4.611\xi') \quad (12)$$

$$D=\xi'(1.545-1.238\xi') \quad (13)$$

$$\beta=3.28\left(2.36\times10^{-5}\right)^{0.25+(\xi-0.5)^7} f'^{2}_c\times10^{-4} \quad (14)$$

$$\beta_s=0.5\left(2.36\times10^{-5}\right)^{0.25+(\xi_s-0.5)^7} f'^{2}_c\times10^{-4} \quad (15)$$

$$\xi_s=A_s f_y/(A_c f_{ck}) \quad (16)$$

$$\varepsilon_u=\varepsilon_0+51659\xi_{cf}-38904\xi_{cf}^2 \quad (17)$$

in above equations, f'_c is compressive strength of the circular concrete specimens, and its relationship with f_{cu}, can be found in relative literature (Tao, Han and Wang [13]); ξ' is confinement factor ratio (Wang, Guan and Zhao [7]), and

$$\xi'=\xi_{cf}/\xi_s \quad (18)$$

The softening property for concrete under tensile stress is simulated by energy criterion, as shown in Figure 9.

In Figure 9, w is concrete crack width; w_1 is the maximum crack width; σ_t is tensile stress of the concrete; G_f is rupture energy of the concrete (for f'_c=20MPa, G_f is of 40N/m, for f'_c=40MPa, G_f is of 120N/m, and for other value of f'_c between 20 MPa and 40 MPa, the value of G_f can be obtained by using interpolation method); σ_{t0} is the ultimate tension stress of the concrete.

$$\sigma_{t0}=0.26(1.5f_{ck})^{2/3} \quad (19)$$

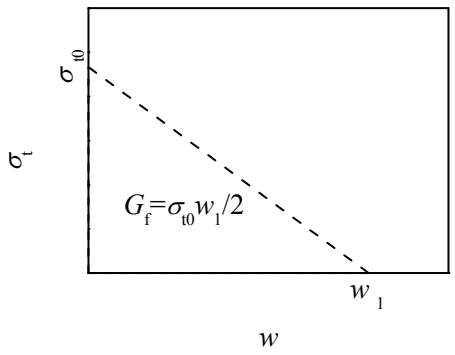

Figure 9. Constitutive Relationship of the Tensile Concrete

3.1.3 CFRP

The CFRP is assumed to be subjected to circular tension, and the stress value in other direction is assumed to be 0.001MPa. Before fracture, the stress-strain relationship is in accordance with Hooke's Law

$$\sigma_{cf\theta}=E_{cf}\varepsilon_{cf\theta} \tag{20}$$

where $\sigma_{cf\theta}$ is circumferential stress of the CFRP.

3.2 FE Model

3.2.1 Element type selection

The element of the steel tube adopts shell element S4 with full integration. To satisfy the computing accuracy, Simpson integration with 9 integrating points in the shell thickness direction is used. For the concrete, 3-D brick elements C3D8R with reduced integration are used for modeling. Membrane element M3D4 with four nodes is used for modeling the CFRP.

3.2.2 Mesh discritization

The convergent analysis is carried out by using refined mesh in FE analysis. In this scheme, an original relative coarse mesh is used to conduct FE analysis, and then the mesh is doubled to carry out FE analysis again to assess the convergence of the numerical results. If the FE results with original and refined meshes converge, i.e., the relative error is less than 1%, the original mesh is suitable for numerical analysis. Otherwise, the mesh will be refined again to conduct additional analysis till the convergence of the FE results is satisfied. Figure 10 is the view of the FE mesh.

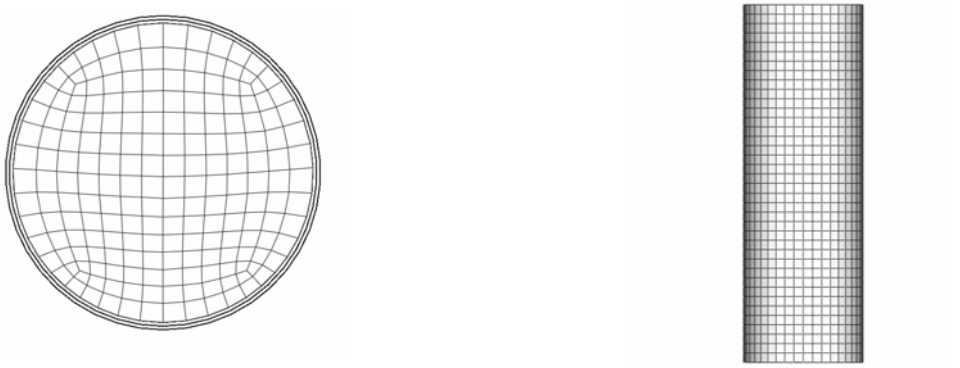

(a) Transverse Element (b) Longitudinal Element

Figure 10. Mesh Discritization

3.2.3 Interface model

Hard contact is used for contact interface between the steel tube and the concrete, i.e., the pressure perpendicular to the contact surfaces (p) can be transferred completely between the two surfaces (Han, Liu and Yang [17]). The tangential force between the steel tube and the concrete surfaces is simulated by using Columb model, i.e., shear force can be transferred between surfaces (Han, Liu and Yang [17]). According to the test results, the CFRP is bound to steel tube, and it is assumed no slip exists between CFRP and steel tube. Same nodal freedoms are used for the contact elements between CFRP and steel tube. When CFRP reaches its ultimate strength and is fractured, CFRP loses its confinement to the steel tube. In the tangential direction of the contact surfaces between

the end plate and the concrete, there is no slipping, and hard contact assumption is used in normal direction of contact surfaces.

3.2.4 Boundary conditions

Only the axial freedom at the load applied end is released, and all the freedoms at the other end are fixed. The displacement is applied along the axis of the columns. To avoid the deformation of the end plate and to model the boundary condition more accurately, the stiffness of the end plate is set to be very large in the FE analysis. The elastic modulus and Poisson's ratio are 10^{12} MPa and 0.0001, respectively.

3.3 FE Results and Parametric Analysis

3.3.1 FE results

To verify the reliability of the above presented FE method, overall 10 C-CFRP-CFST specimens are analyzed by using ABAQUS software. The FEM results together with the tested measured results are plotted in Figure 11. It can be found from Figure 11 that the FEM results agree reasonably well with the experimental results.

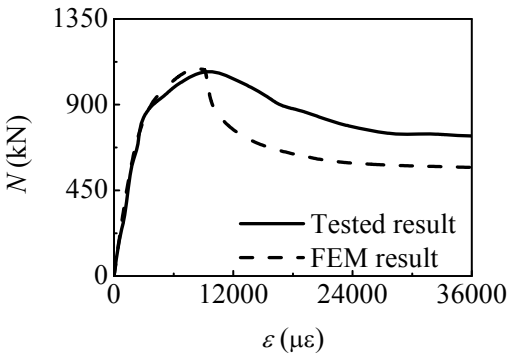

(a) CSC A-1

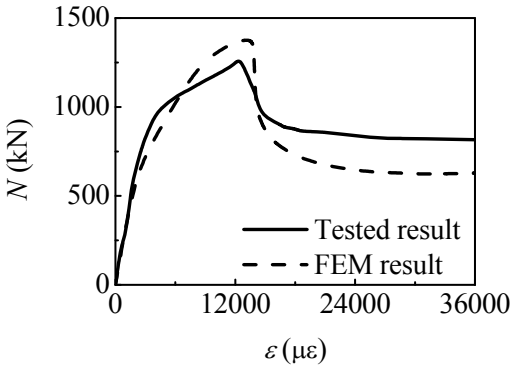

(b) CSC A-2

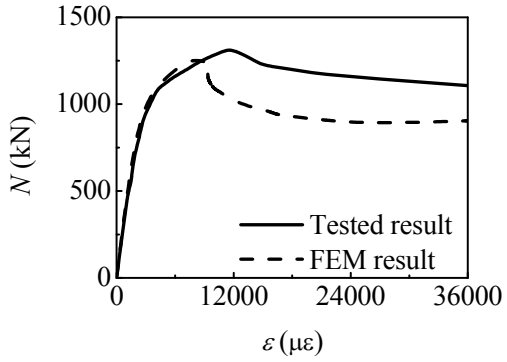

(c) CSC B-1

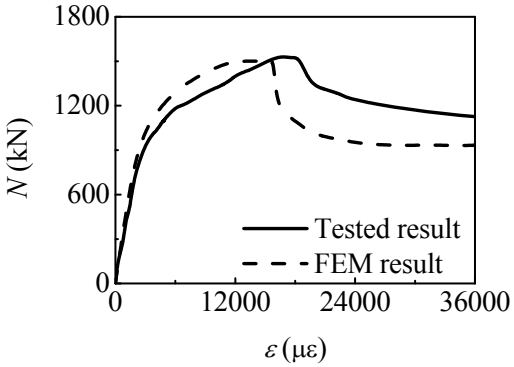

(d) CSC B-2

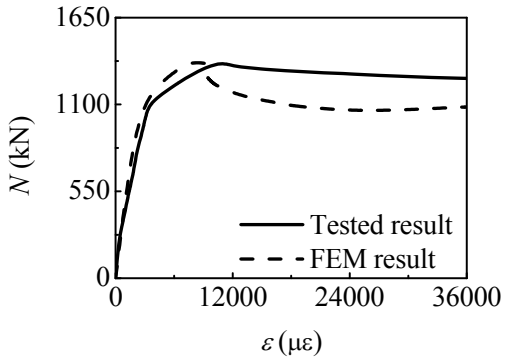

(e) CSC C-1

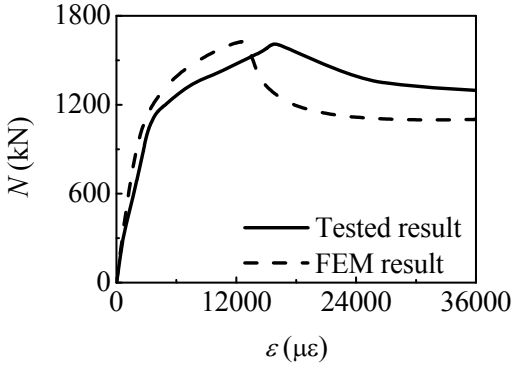

(f) CSC C-2

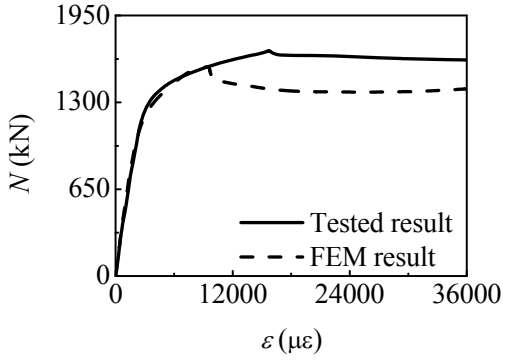

(g) CSC D-1

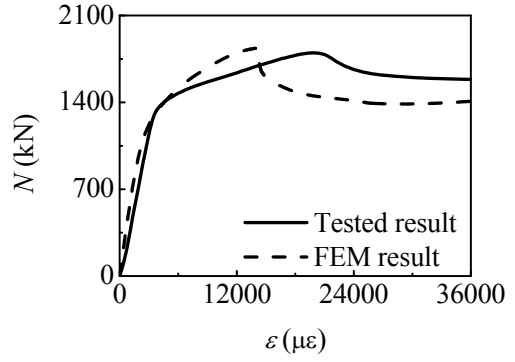

(h) CSC D-2

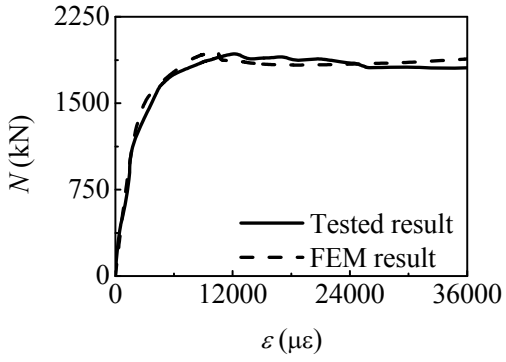

(i) CSC E-1

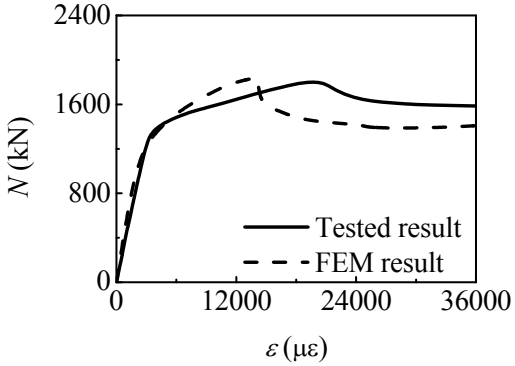

(j) CSC E-2

Figure 11. Comparison between FEM Results and Tested Results of *N*-*ε* Curves of the C-CFRP-CFST Stub Columns

3.3.2 Failure modes

Figure 12 (a) shows failure mode of the C-CFRP-CFST stub column. For comparing purpose, failure modes of the C-CFST stub column and circular steel tubular stub column are also given, and they are shown in Figure 12 (b) and 12 (c), respectively. It can be seen from Figure 12 (c) that local buckling occurs at both ends of the circular steel tubular stub column. For C-CFST stub column, it convexes at the mid-height cross-section. Similarly, C-CFRP-CFST stub column also convexes at the mid-height cross-section. However, its deformation is relatively smaller due to the confinement of the un-fractured CFRP.

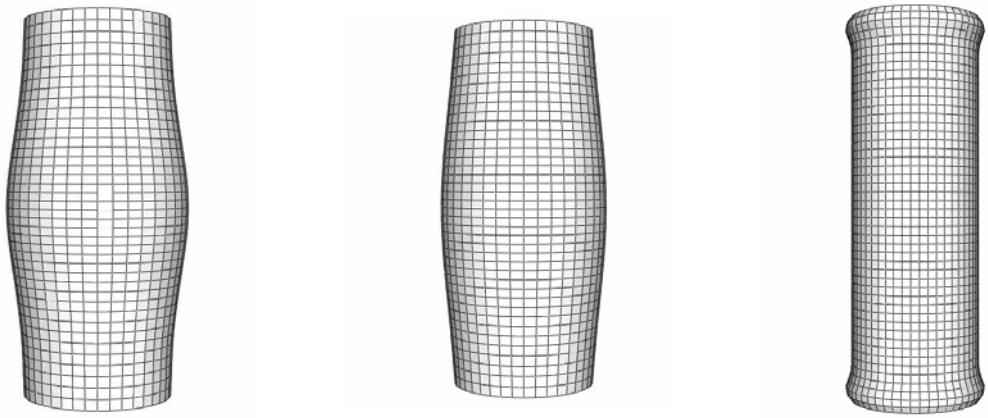

(a) C-CFRP-CFST (b) C-CFST (c) Circular Steel Tube

Figure 12. Failure Modes

3.3.3 Parametric study

Figure 13 (a) illustrates the N-ε curves of a series of specimens. For these specimens, the value of ξ_s is fixed to be 1.314, and ξ_{cf} has different values. For other parameters, f_{cu}=55MPa, f_y=350MPa, $f_{cf\theta}$=1.26GPa, D_s=129mm, L=400mm, E_c=4700$f'_c{}^{0.5}$ (MPa) and v_c=0.2.

It is found from Figure 13 (a) that the maximum load bearing capacity and the ultimate compressive strain increase as ξ_{cf} increases when the value of ξ_s is constant. Whatever value of ξ_{cf} is taken,, the curves of C-CFRP-CFST specimens after fracture almost concurrent, which are all classified as the curves of unwrapped stub columns.

The N-ε curves for the specimens with constant ξ_{cf} (the value is 0.245) and with different values of ξ_s are plotted in Figure 13 (b). For other parameters: f_{cu}=60MPa, f_y=350MPa, $f_{cf\theta}$=1.26GPa, D_s=129mm, L=400mm, E_c=4700$f'_c{}^{0.5}$ (MPa) and v_c=0.2. It is found from Figure 13(b) that the ultimate strain does not vary much with different values of ξ_s. However, the maximum load bearing capacity increases as ξ_s increases.

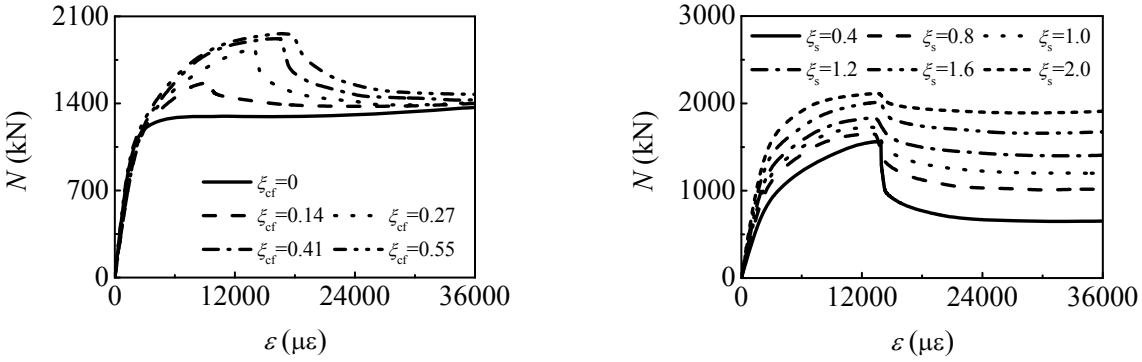

(a) ξ_s=1.314 (b) ξ_{cf}=0.245

Figure 13. Influence of Confinement Factor on N-ε Curves

4. FURTHER ANALYSIS

The details of the typical model are listed as follows: L=1200mm, D_s=400mm, t_s=9.3mm, f_y=345MPa, ξ_{cf}=0.191, ξ_s=0.857, f_{cu}=60MPa, E_c=4700$f'_c{}^{0.5}$ (MPa) and v_c=0.2.

4.1 Stress-Strain Curves

Figure 14 gives stress (σ)-strain curves of the C-CFST stub columns under axial compression. For a clear expression, longitudinal stress of the steel tube (σ_{sl}) is divided by 10, and the confinement force (p) is multiplied by 5. It can be found from Figure 14 that the confinement force in the initial stage (ε<800με) is negative. This means there is minor tensile stress on the steel and the concrete interface because Poisson's ratio of the steel is bigger than that of the concrete at this time, and the steel and the concrete have an apart tendency.

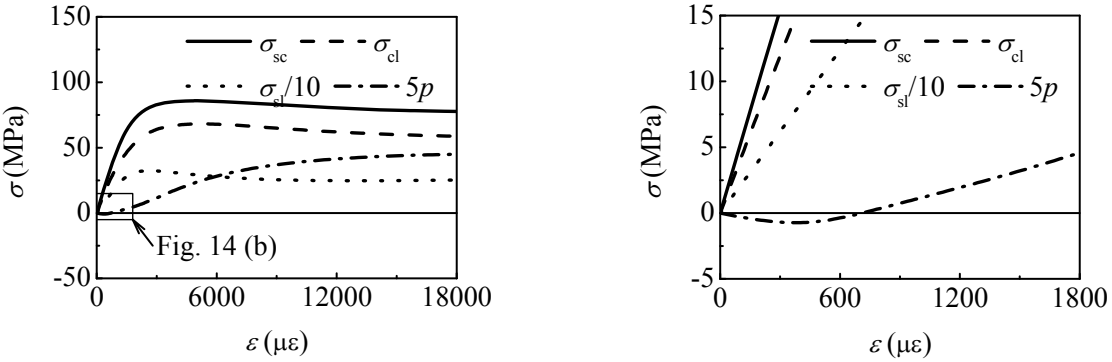

(a) Full View (b) Magnified Part

Figure 14. σ versus ε Curves of the C-CFST Stub Columns

Figure 15 shows stress-strain curves of the C-CFRP-CFST stub columns under axial compression. Similarly, longitudinal stress of the steel and circular stress of the CFRP are also divided by 10, and the confinement force is multiplied by 5. As shown in Figure 15, the steel tube always provides positive confinement force to the concrete for C-CFRP-CFST stub columns due to the existence of CFRP. In elasto-plastic stage, steel begins to yield before the stub columns reach the ultimate tensile strength. At this time, the confinement force between the steel tube and the concrete is increasing steadily. When CFRP reaches its ultimate tensile strength and is fractured, the stress-strain curve of the concrete has steep decreasing segment and then it becomes gradual. Meanwhile, the confinement force of outer tube begins to decrease because CFRP does not work now, and only steel tube provides confinement to the concrete. Before fracture, CFRP is always in linear and elastic stage. However, the stresses in CFRP reduce to zero rapidly after fracture.

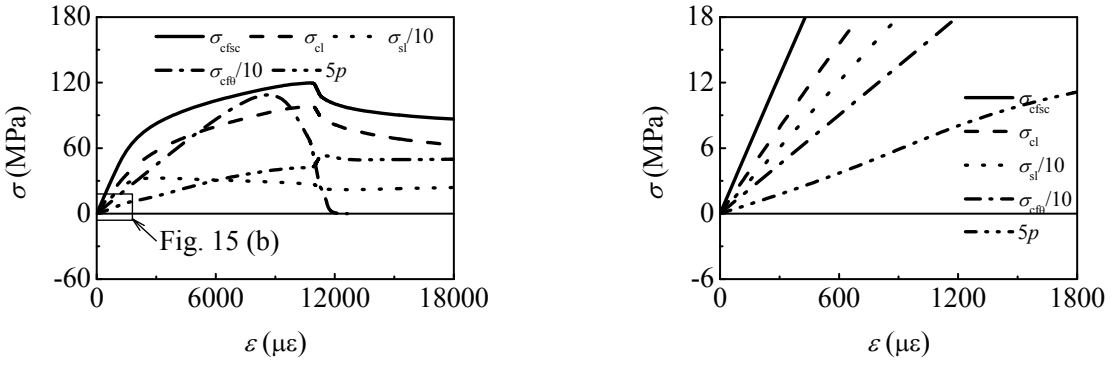

(a) Full View (b) Magnified Part

Figure 15. σ versus ε Curves of the C-CFRP-CFST Stub Columns

Additionally, the elasto-plastic stage of C-CFRP-CFST stub columns is longer than that of C-CFST stub columns due to the confinement of CFRP to the tube. The maximum load bearing capacity also increases, and the stress decreasing stage of the concrete is much different due to the existence of the CFRP.

4.2 Stress Analysis

Distribution of σ_{cl} on the mid-height cross-section of the C-CFRP-CFST stub columns is shown in Figure 16. Point 1 is the yield point of steel tube, and the specimen reaches its maximum load bearing capacity at point 2, the strain at point 3 is 20000με. From Figure 16, it can be found that the longitudinal stresses of concrete on mid-height cross-section are almost uniform when steel tube becomes yielding, and the value is about f'_c. Before reaching the maximum load bearing capacity, the longitudinal stress in concrete is the maximum, and the value is about $2f'_c$. The stress values become smaller when the distance from the center is bigger. When the strain is equal to 20000με, the longitudinal stress at the centroid of concrete has a little drop and the stresses of outer concrete also decrease. However, the stresses along circular direction always keep uniformly.

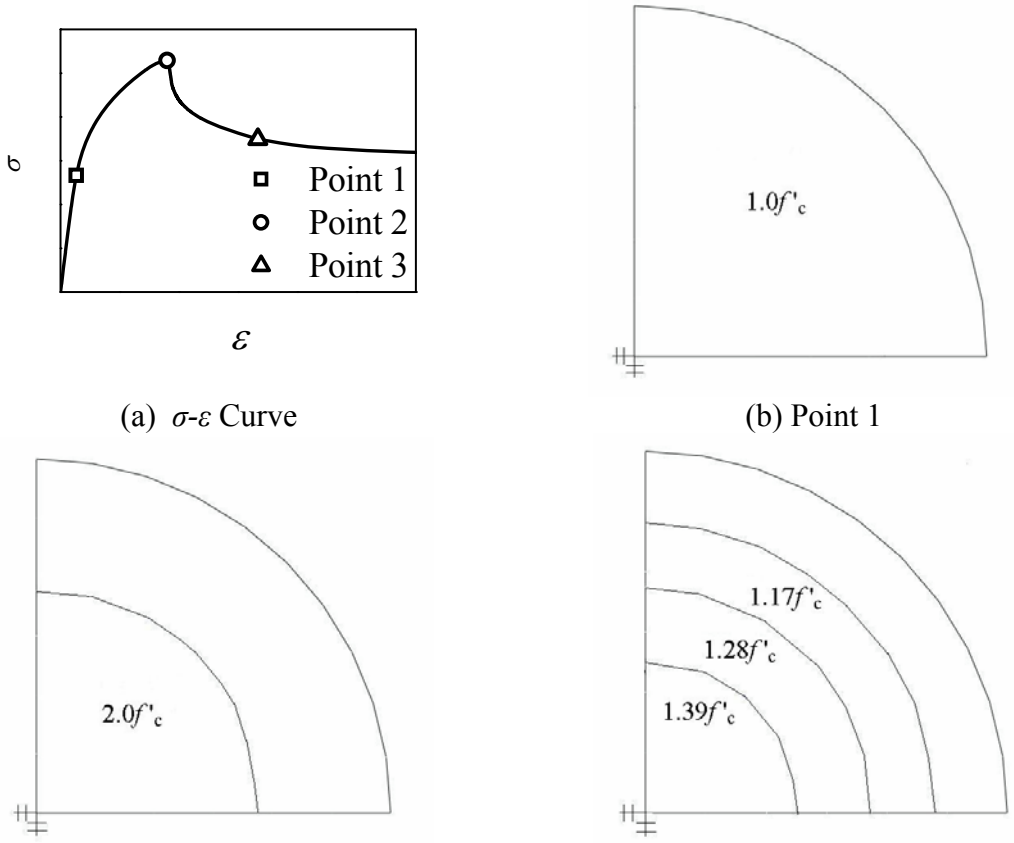

(a) σ-ε Curve (b) Point 1

(c) Point 2 (d) Point 3

Figure 16. Distribution of σ_{cl} on Mid-height Cross-section of the C-CFRP-CFST Stub Columns

The variations of the steel tube stresses in longitudinal direction (σ_{sl}) and in circular direction ($\sigma_{s\theta}$) on the mid-height cross-section of C-CFST stub columns and C-CFRP-CFST stub columns under compression are plotted together in Figures 17 (a) and 17 (b), where σ_s is stress of the steel tube. It is noted that Figures 17 (a) and 17 (b) only provide the stress magnitude and ignore the stress sign. It can be seen from Figure 17 that the variation of σ_s of the C-CFRP-CFST stub columns under axial compression is much similar with that of the C-CFST stub columns before the fracture of CFRP whereas the circular stress of the steel tube increases rapidly and the longitudinal stress decreases sharply due to rupture of the CFRP.

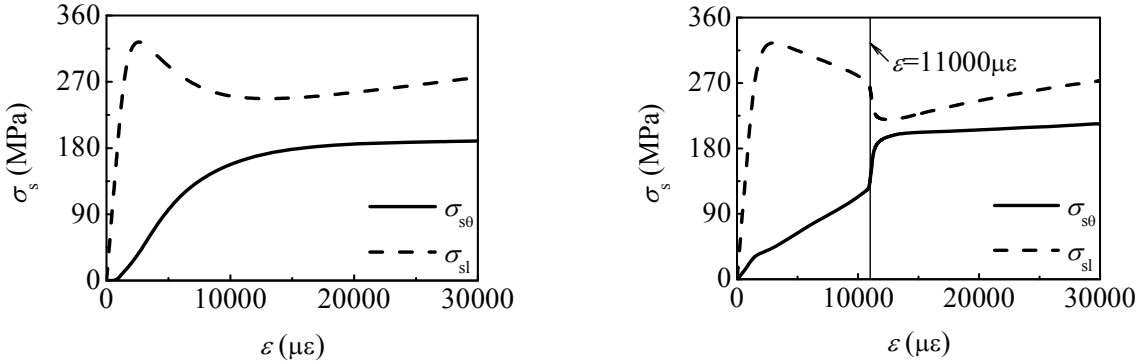

(a) C-CFST (b) C-CFRP-CFST

Figure 17. Stress versus Strain Curves of the Steel Tube

The longitudinal and circular stress distributions of the steel tube at different heights of the C-CFRP-CSFT stub columns under axial compression are shown in Figure 18, where $\sigma_{s\theta,\,L/4}$, $\sigma_{s\theta,\,3L/8}$ and $\sigma_{s\theta,\,L/2}$ are circumferential stresses of the steel tube at $L/4$, $3L/8$ and $L/2$ from the end plate of the specimen respectively, and $\sigma_{sl,\,L/4}$, $\sigma_{sl,\,3L/8}$ and $\sigma_{sl,\,L/2}$ are longitudinal stresses of the steel tube at $L/4$, $3L/8$ and $L/2$ from the end plate of the specimen respectively. It is found that $\sigma_{s\theta}$ increase as the distance from the end of the specimen increases. However, the longitudinal stresses have an inverse tendency. During the load applying process, loads transfer from two ends of the stub columns to the midst. The midst of the steel tube yields firstly and then the yielding region propagates toward to both ends of the column. Finally, the CFRP is fractured at the midst of the column. The numerical results agree well with the experimental observation.

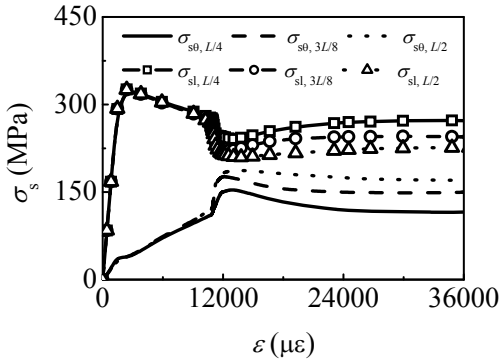

Figure 18. Distribution of σ_s along Height of the C-CFRP-CFST Stub Columns

Figures 19 and 20 are circular stress and principle stress vector (red arrows) of the CFRP for C-CFRP-CFST stub columns, respectively. It can be seen from Figures 19 and 20 that the stub is still in elastic stage at point 1. In this time, the circumferential tensile stress of CFRP is less than its tensile strength, and the principle stresses in the direction of the stub height distribute uniformly. At point 2, CFRP at the mid of the specimen begins to fracture because its stresses reach the tensile strength. At point 3, most of the CFRP are fractured and don't work again. The numerical failure process agrees with experimental observation very well.

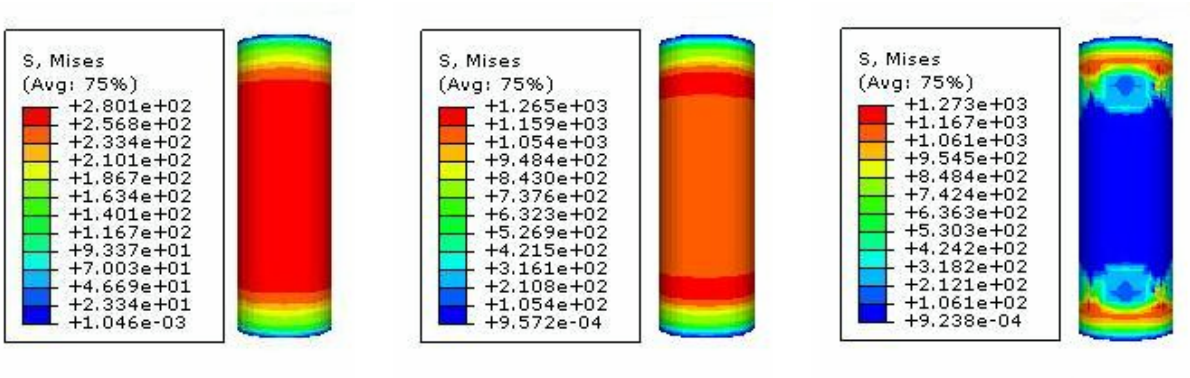

(a) Point 1 (b) Point 2 (c) Point 3

Figure 19. $\sigma_{cf\theta}$ of the C-CFRP-CFST Stub Columns

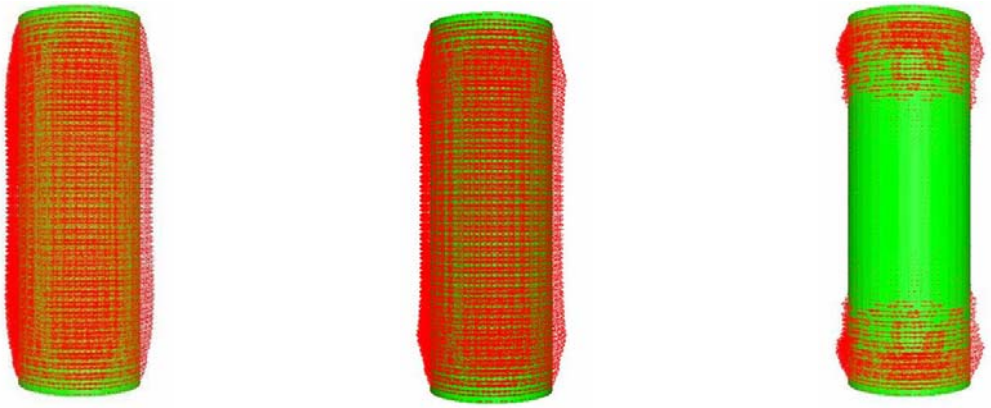

(a) Point 1 (b) Point 2 (c) Point 3

Figure 20. Principle Stress Vector of CFRP of the C-CFRP-CFST Stub Columns

4.3 Strain Analysis

The longitudinal stress-strain relationships for C-CFRP-CFST (f_{cu}=60MPa, f_y=350 MPa, $f_{cf\theta}$=1.26GPa, D_s=129mm, L=400mm, E_c=4700$f'_c{}^{0.5}$ (MPa) and v_c=0.2) with same CFRP confinement factors and different steel tube confinement factors are studied. Similarly, such relationships for C-CFRP-CFST (f_{cu}=60MPa, f_y=350MPa, $f_{cf\theta}$=1.26GPa, D_s=133mm, L=400mm, E_c=4700$f'_c{}^{0.5}$ (MPa) and v_c=0.2) with same steel tube confinement factors and different CFRP confinement factors are also investigated. These results are illustrated in Figures 21 (a) and 21 (b) respectively. As shown in Figure 21, the peak stress of concrete increases as ξ_s becomes bigger and ξ_{cf} is kept constant. However, the variation of the peak stress value is not very remarkable. When ξ_s is kept constant and ξ_{cf} becomes bigger, the peak stress and strain both increase.

Figure 22 and Figure 23 are distributions of circular strains of the steel tube for C-CFST stub columns and C-CFRP-CFST stub columns, respectively. Comparing the results in Figures 22 and 23, it is found that CFRP is in elastic stage at point 1, and the CFRP can still provide confinement to the steel tube. Therefore, the circumferential strains of the steel tube of C-CFRP-CFST are a little smaller than those of C-CFST. At point 2, the circumferential strains of the steel tube are much smaller than those of C-CFST, and this means CFRP has remarkable confinement to the steel tube in circumferential direction at this time. At point 3, the CFRP at the mid of the C-CFRP-CFST is fractured, and thus it loses the confinement to the steel tube. Based on the above reasons, the circumferential strains of the steel tube for the two specimens are almost the same.

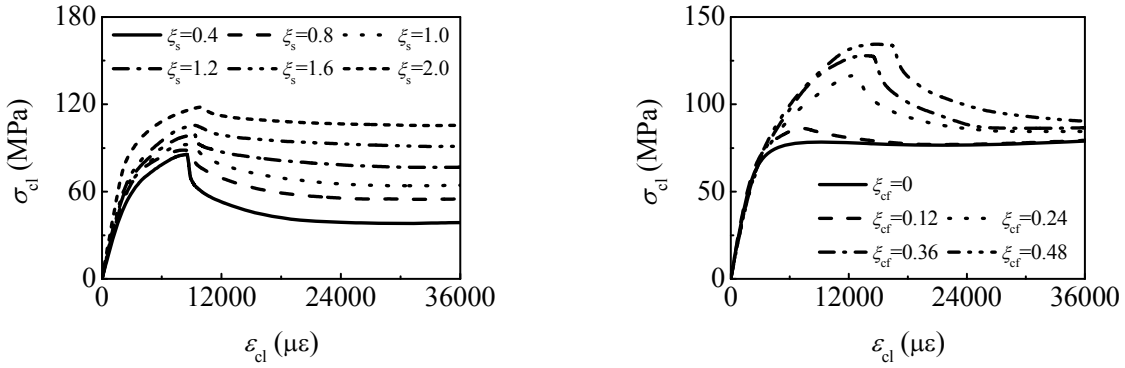

(a) ξ_{cf}=0.132 (b) ξ_s=1.3

Figure 21. Longitudinal Stress versus Strain Curves of the Concrete for C-CFRP-CFST Stub Column

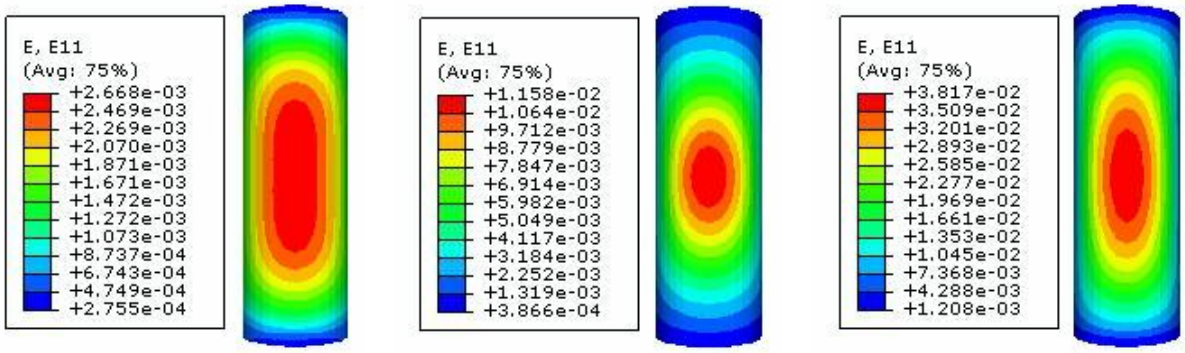

(a) Point 1 (b) Point 2 (c) Point 3

Figure 22. $\varepsilon_{s\theta}$ of the C-CFST Stub Columns

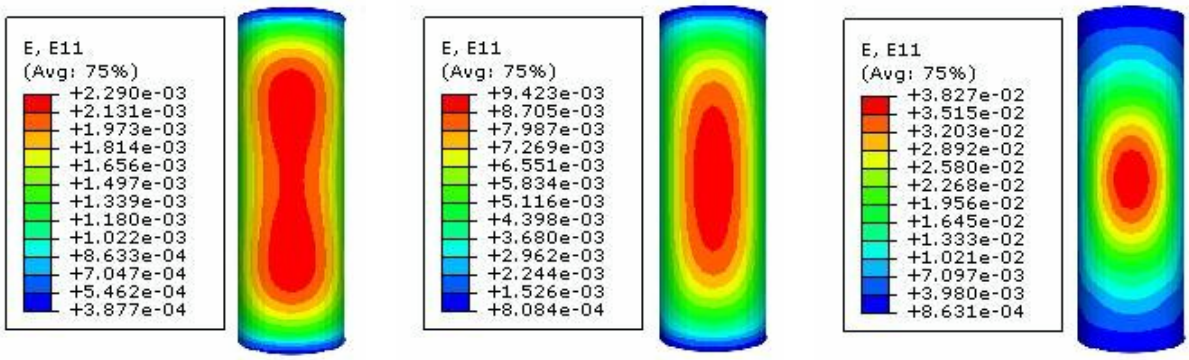

(a) Point 1 (b) Point 2 (c) Point 3

Figure 23. $\varepsilon_{s\theta}$ of the C-CFRP-CFST Stub Columns

4.4 Effect of Initial Stress in the Steel Tube on Properties of the Columns

Figure 24 shows load-strain curves of the C-CFRP-CFST stub columns under axial compression with different initial stress coefficients (β_0), and

$$\beta_0=\sigma_{s0}/(\phi_s f_y) \tag{21}$$

where σ_{s0} is initial stress in the steel tube, and ϕ_s is stability coefficient of the circular steel tube.

As shown in Figure 24, the initial stress in the steel tube can reduce the stiffness in elastic stage of the C-CFRP-CFST stub columns under axial compression, and the load bearing capacity decreases as the initial stress coefficient increases.

A series of p-ε curves for C-CFRP-CFST stub columns under axial compression with different initial stress coefficients are plotted in Figure 25. The initial stress in the steel tube produces initial compressive strain in the steel tube before the steel tube and the concrete are subjected to loading jointly, which can postpone the mutual reaction between the steel tube and the concrete. Generally, the initial stress of steel tube has a little influence on the peak value of the confinement force.

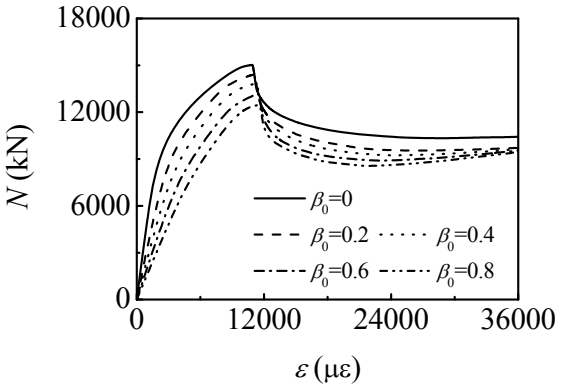

Figure 24. Influence of σ_{s0} on N-ε Curves of the C-CFRP-CFST Stub Columns

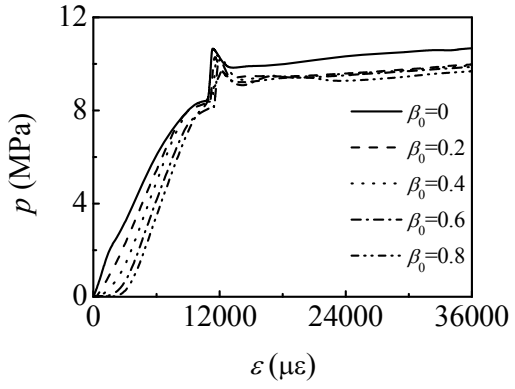

Figure 25. Influence of σ_{s0} on p-ε Curves of the C-CFRP-CFST Stub Columns

Figure 26 shows the longitudinal stress distribution on the cross-section of the column midst before ultimate state for the C-CFRP-CFST stub columns under axial compression with different initial stress coefficients of the steel tube. It can be seen from Figure 26 that the initial stress in the steel tube has very little effect on the longitudinal stress distribution on the mid-height cross-section of the concrete before the specimen reaches the ultimate state, and the longitudinal stress values decrease as the initial stress coefficients become bigger.

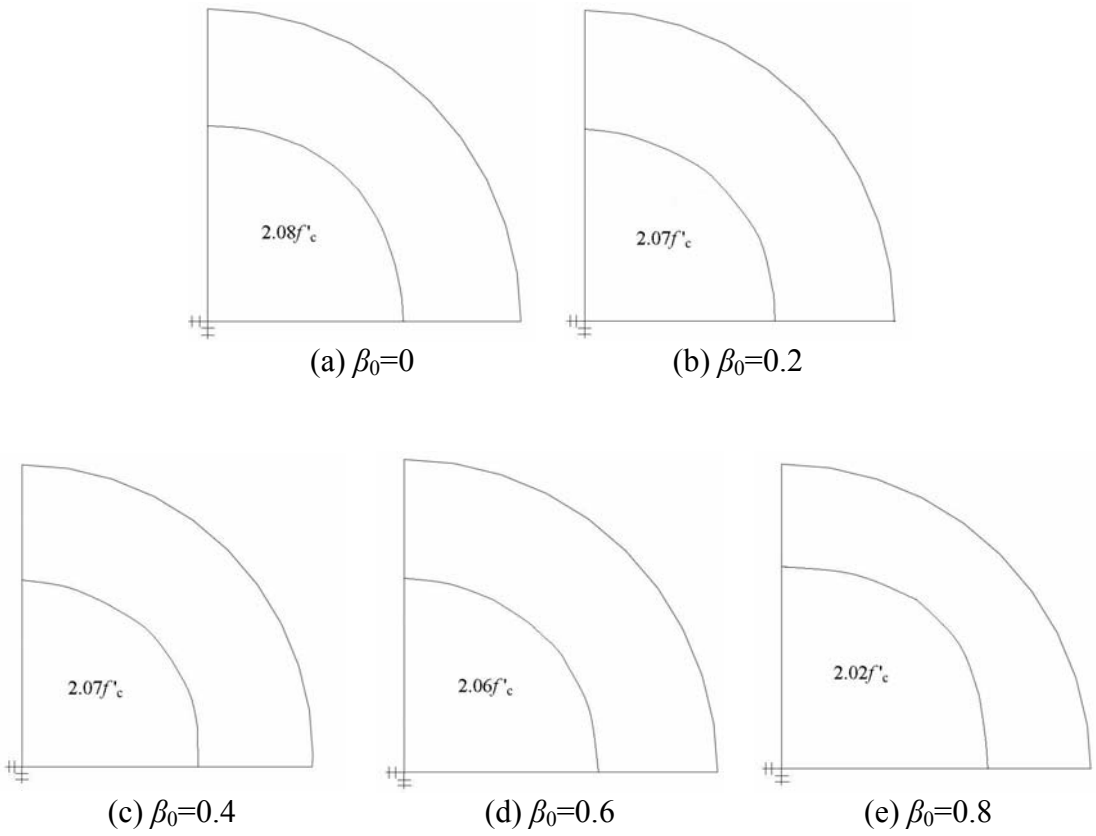

(a) β_0=0 (b) β_0=0.2

(c) β_0=0.4 (d) β_0=0.6 (e) β_0=0.8

Figure 26. Influence of σ_{s0} on Longitudinal Stress Distribution of the Concrete at Mid-height Cross-section for C-CFRP-CFST Stub Columns

4.4 Effect of Adhesive Strength on Properties of the Columns

Three friction factors with values of 0, 0.3 and 0.6 are used to model the different adhesive strength between steel tube and the concrete. Figure 27 shows the influence of adhesive strength on *N*-*ε* curves of the C-CFRP-CFST stub columns. As shown in Figure 27, the effect of adhesive strength on the *N*-*ε* curves is very little.

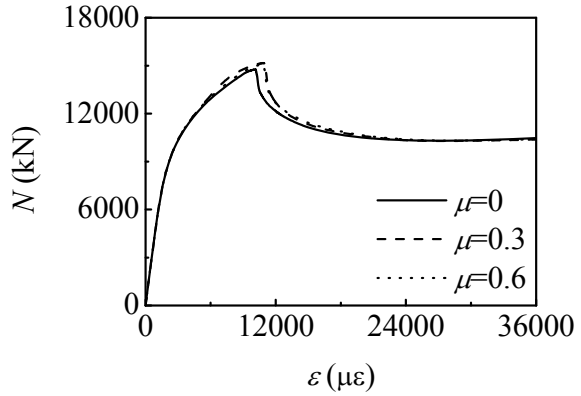

Figure 27. Influence of Adhesive Strength on *N*-*ε* Curves of the C-CFRP-CFST Stub Columns

5. LOAD BEARING CAPACITY INDEX

5.1 Expression

The stress-strain relationship of the C-CFRP-CFST stub column is investigated based on the FE analysis of many models. The validity range of these models is: f_y=200-400MPa, f_u=30-120MPa, ξ_s=0.2-4, ξ_{cf}=0-0.6. Finally, the load bearing capacity at the longitudinal strain ε_{cfscy} (Figure 6) which is determined from the stress-strain curves is defined as the load bearing capacity index of axial compressive strength (f_{cfscy}). ε_{cfscy} is expressed as follow

$$\varepsilon_{cfscy}=1300+12.5f'_c+(600+33.3f'_c)\xi^{0.2}\ (\mu\varepsilon) \tag{22}$$

The relationship between γ_c ($=f_{cfscy}/f_{ck}$) and ($\xi_s+3\xi_{cf}$) can be expressed with simple equation as shown in Figure 28 (a).

The equation is obtained from regression analysis and f_{cfscy} is listed as follow

$$f_{cfscy}=[1.14+1.02(\xi_s+3\xi_{cf})]f_{ck} \tag{23}$$

The load bearing capacity (N_u) of the C-CFRP-CFST stub column under axial compression can be calculated by using the following equation

$$N_u=A_{cfsc}f_{cfscy} \tag{24}$$

In case of no CFRP (C-CFST), Eqs. (22)-(24) are reduced to the corresponding calculating equations of the C-CFST stub columns (Han, Yao and Zhao [18]).

Figure 28 (b) shows the comparison of the estimated results of N_u (N_u^c) and the experimental results of N_u (N_u^e) for the stub columns. It is found that the simplified equation can produce reasonably accurate estimations. The average of N_u^c/N_u^e is 0.902 and the mean square deviation is 0.0536. In general, the predicted results from the equation are safe.

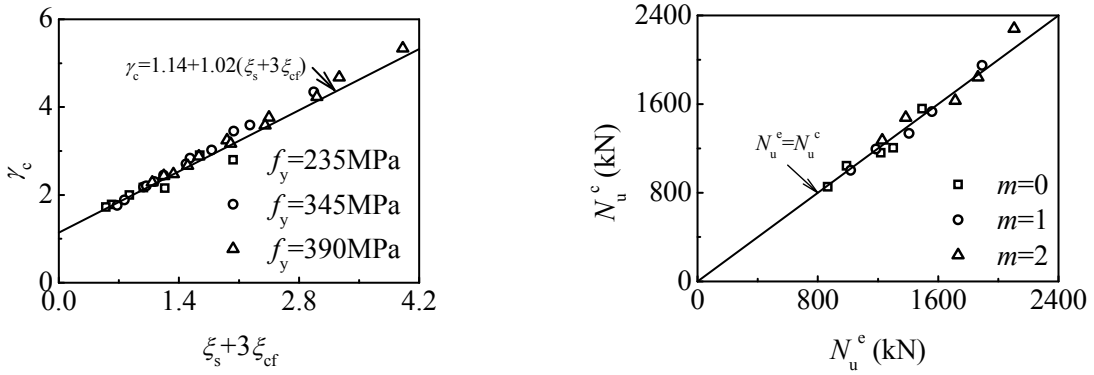

(a) Curve-fitting Expression

(b) Comparison between Predicted Results and Tested Results for N_u

Figure 28. Load Bearing Capacity Index

5.2 Load Bearing Capacity Increment Ratio

For specimens with the same t_s, named N_u^e of C-CFST as N_{u0}^e, and that of C-CFRP-CFST as N_{um}^e, then r is load bearing capacity increment ratio,

$$r=(N_{um}^e-N_{u0}^e)/N_{u0}^e\times100\% \tag{25}$$

r are listed in Table 1 and plotted against ξ_{cf} in Figure 29. Figure 29 shows that comparing with the C-CFST stub columns, N_{um}^e are all enhanved, and r increases nearly linearly with the increment of m.

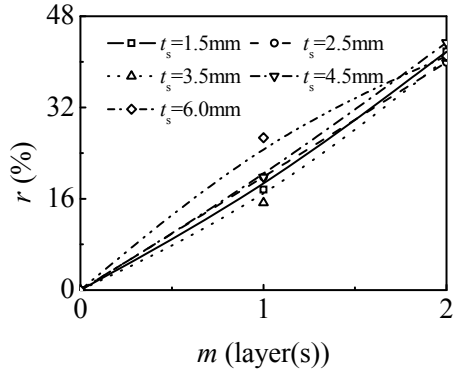

Figure 29. Influence of m on Load Bearing Capacity Increment Ratio (r)

5.3 Stiffness

Referring to corresponding study (Han, Yao and Zhao [18]), it is found from computation that the following equation can be used to calculate the longitudinal stiffness ($E_{cfsce}A_{cfsc}$) of the C-CFRP-CFST stub columns

$$E_{cfsce}=f_{cfscp}/\varepsilon_{cfscp} \tag{26}$$

$$f_{cfscp}=[0.192/(1-0.6\xi_{cf})^2(f_y/235)+0.488(1-2.4\xi_{cf})]f_{cfscy} \tag{27}$$

$$\varepsilon_{cfscp}=3.25\times10^{-6}f_y \tag{28}$$

where f_{cfscp} is nominal proportional limit of the C-CFRP-CFST stub columns, and ε_{cfscp} is the corresponding strain at the nominal proportional limit.

Eqs. (26)-(28) are also suitable for C-CFST stub columns (ξ_{cf}=0).

The $E_{cfsce}A_{cfsc}$ of the tested specimens are tabulated in Table 1 and shown in Figure 30. As can be seen that the specimens exhibited an increase in their stiffness after being wrapped with CFRP and their stiffness increased with the increasing number of m.

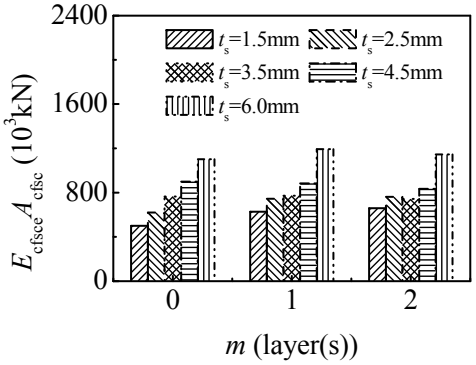

Figure 30. Stiffness Comparison for Specimens

6. CONCLUSIONS

The following conclusions can be drawn based on the study: (1) The load carrying capacity and the longitudinal stiffness of the concrete filled circular CFRP-steel tubes (C-CFRP-CFST) increase while their ductility decreases with the increasing number of CFRP layers. The failure mode of the C-CFRP-CFST stub columns under axial compression is similar with that of the concrete filled circular steel tubular (C-CFST) stub columns, but the deformation from the midst toward to both ends is relatively smaller. The steel tube and the CFRP tube work concurrently before failure. (2) The outer tube of the C-CFRP-CFST stub columns always provides confinement force to the concrete. When the CFRP is fractured, the circular stress of steel tube increases rapidly whereas the longitudinal stress decreases sharply, and stress redistribution exists at this time. (3) The load-strain curves are analyzed using ABAQUS and it is found that the numerical results agree well with experimental results although they are generally safe. (4)The initial stress in the steel tube can postpone the mutual reaction between the steel tube and the concrete, while it has a little influence on the peak value of the confinement force; adhesive strength has little effect on compressive performances of the C-CFRP-CFST stub columns. (5) The proposed parametric expression can be used to calculate load bearing capacity of the C-CFRP-CFST stub columns reasonably.

Besides studying on static performance of the C-CFRP-CFST stub column, other systematic researches like monotonic behaviour of the C-CFRP-CFST flexural member, the C-CFRP-CFST beam-columns and cyclic behaviour of the C-CFRP-CFST beam-columns which are investigated by authors' group are operating. The relevant results may be presented in other papers.

ACKNOWLEDGEMENTS

The research reported in the paper is part of the project NCET-08-0865 supported by New Century Excellent Talent of the Ministry of Education of China, and the Project 2007R31 supported by Colleges and Universities Excellent Talent of Liaoning Province, China. The financial support is highly appreciated.

NOMENCLATURE

A_c : Cross-sectional area of the concrete
A_{cfsc} : Cross-sectional area of the C-CFRP-CFST stub columns
$A_{cf\theta}$: Cross-sectional area of the CFRP
A_s : Cross-sectional area of the steel tube
A_{sc} : Cross-sectional area of the C-CFST stub columns
C : Coefficient
C-CFRP-CFST : Concrete filled circular CFRP-steel tubes
C-CFST : Concrete filled circular steel tubes
CFRP : Carbon fiber reinforced plastic/polymer
CFRP-CFST : Concrete-filled CFRP-steel tubes
CFST : Concrete-filled steel tubes
D : Coefficient
DI : Ductility index
D_s : Outer diameter of the steel tube
E_c : Elasticity modulus of the concrete
E_{cf} : Elasticity modulus of the carbon fiber sheets
$E_{cfsce}A_{cfsc}$: Longitudinal stiffness of the specimens
E_s : Elasticity modulus of the steel tube
FRP : Fiber reinforced plastic/polymer
f_{cfscp} : Nominal proportional limit of the specimens
f_{cfscy} : Load bearing capacity index of axial compressive strength of the specimens
$f_{cf\theta}$: Ultimate tensile strength of the CFRP
f_{ck} : Designed axial compressive strength of the concrete
f_{cu} : Cubic strength of the concrete
f_u : Ultimate strength of the steel tube
f_y : Yield strength of the steel tube
f'_c : Compressive strength of the circular concrete specimens
f'_{cf} : Tension strength of the carbon fiber sheet
G_f : Rupture energy of the concrete
GFRP : Glass fiber reinforced plastic/polymer
L : Length of the stub columns
m : Number of layer(s) of the CFRP
N : Axial load
N_u : Load bearing capacity
N_u^c : Estimated results of N_u
N_u^e : Experimental results of N_u
N_{u0}^e : N_u^e of the C-CFST stub columns
N_{um}^e : N_u^e of the C-CFRP-CFST stub columns
p : Confinement force
q : A quantity related to total confinement factor
r : Load bearing capacity increment ratio
S-CFRP-CFST : Concrete filled square CFRP-steel tube
S-CFST : Concrete filled square steel tube
t_{cf} : Thickness of 1 layer carbon fiber sheet
t_s : Wall thickness of the steel tube
v_c : Elasticity Poisson's ratio of the concrete
v_s : Elasticity Poisson' ratio of the steel tube
w : Concrete crack width
w_1 : The maximum concrete crack width

w_{cf} : Unit weight of the carbon fiber sheet
β : A quantity related to total confinement factor before fracture of the CFRP
β_0 : Initial stress coefficients
β_s : A quantity related to confinement factor of the steel tube
δ_{cf} : Elongation percentage of the carbon fiber sheet
δ_s : Elongation percentage of the steel tube
Δ : Axial shortening of the specimens
ε : Longitudinal strain of the specimens
ε_0 : Ultimate compressive strain of the concrete
$\varepsilon_{75\%}$: Longitudinal strain when the load attains 75% of the maximum load in the pre-peak stage
$\varepsilon_{85\%}$: Longitudinal strain when the load falls to 85% of the maximum load
ε_{cfscp} : Strain corresponding to f_{cfscp}
ε_{cfscy} : Strain corresponding to f_{cfscy}
$\varepsilon_{cf\theta}$: Circumferential strain of the CFRP
$\varepsilon_{cf\theta r}'$: Fracture strain of CFRP on the specimen
$\varepsilon_{cf\theta r}$: Average value of all $\varepsilon_{cf\theta r}'$
ε_{cl} : Longitudinal strain of the concrete
ε_{sl} : Longitudinal strain of the steel tube
ε_{sy} : Yield strain of the steel tube
$\varepsilon_{s\theta}$: Circumferential strain of the steel tube
ε_u : Longitudinal strain of the specimen (ε) when CFRP is fractured
ε_θ : Circumferential strain
ϕ_s : Stability coefficient of the circular hollow steel tube
μ : Friction factor
σ : Stress
σ_0 : Ultimate compressive stress of the concrete
σ_{cfsc} : Nominal compression stress of the C-CFRP-CFST specimens
$\sigma_{cf\theta}$: Circumferential stress of the CFRP
σ_{cl} : Longitudinal stress of the concrete
σ_s : Stress of the steel tube
σ_{s0} : Initial stress in the steel tube
σ_{sc} : Nominal compression stress of the C-CFST specimen
σ_{sl} : Longitudinal stress of the steel tube
$\sigma_{s\theta}$: Circumferential stress of the steel tube
σ_t : Tensile stress of the concrete
σ_{t0} : Ultimate tensile stress of the concrete
ξ : Total confinement factor
ξ_{cf} : Confinement factor of the CFRP
ξ_s : Confinement factor of the steel tube
ξ' : Confinement factor ratio

REFERENCES

[1] Han, L. H., "Tests on Concrete Filled Steel Tubular Columns with High Slenderness Ratio", Advances in Structural Engineering, 2000, Vol. 3, No. 4, pp. 337-344.

[2] Tao, Z., Uy, B., Han, L.H. and Wang, Z.B., "Analysis and Design of Concrete-filled Stiffened Thin-walled Steel Tubular Columns under Axial Compression", Thin-Walled Structures, 2009, Vol. 47, No. 12, pp. 1544-1556.

[3] Georgios, G. and Lam, D., "Axial Capacity of Circular Concrete-filled Tube Columns", Journal of Constructional Steel Research, 2004, Vol. 60, No. 7, pp. 1049-1068.

[4] Uy, B., "Strength of Short Concrete Filled High Strength Steel Box Columns", Journal of Constructional Steel Research, 2001, Vol. 57, No. 2, pp. 113-34.

[5] Wang, Y.C. and Restrepo, J.I., "Investigation of Concentrically Loaded Reinforced Columns Confined with Glass Fiber-reinforced Polymer Jackets", Structure Journal, 2001, Vol. 98, No. 3, pp. 377-385.

[6] Teng, J.G., Chen, J.F., Smith, S.T. and Lam, L., "FRP Strengthened RC Structures", John Wiley & Sons Ltd., 2002.

[7] Wang, Q.L., Guan, C.W. and Zhao, Y.H., "Theoretical Analysis about Concentrically Compressed Concrete Filled Hollow CFRP-Steel Stub Columns with Circular Cross-section", Proceeding of the 2nd International Conference on Steel and Composite Structures, Seoul, Korea, 2004, pp. 684-695.

[8] Tao, Z., Han, L. H. and Zhuang, J.P., "Using CFRP to Strengthen Concrete-filled Steel Tubular Columns: Stub Column Tests", Proceeding of the 4th International Conference on Advances in Steel Structures, Shanghai, China, 2005, Vol. 1, pp. 701-706.

[9] Han, L.H., "Advanced Composite and Mixed Structures-Testing, Theory and Design Approach", China Science Press, 2009. (in Chinese)

[10] Tao, Z., Han, L.H. and Wang, L.L., "Compressive and Flexural Behaviour of CFRP Repaired Concrete-filled Steel Tubes after Exposure to Fire", Journal of Constructional Steel Research, 2007, Vol. 63, No. 8, pp. 1116-1126.

[11] Xiao, Y., He, W.H. and Choi, K.K., "Confined Concrete-filled Tubular Columns." Journal of Structural Engineering, 2005, Vol. 131, No. 3, pp. 488-497.

[12] Choi, K.K. and Xiao, Y., "Analytical Model of Circular CFRP Confined Concrete-filled Steel Tubular Columns under Axial Compression", Journal of Composites for Construction, 2010, Vol. 14, No. 1, pp. 125-133.

[13] Tao, Z., Han, L.H. and Wang, Z.B., "Experimental Behaviour of Stiffened Concrete-filled Thin-walled Hollow Steel Structural (HSS) Stub Columns", Journal of Constructional Steel Research, 2005, Vol. 61, No. 7, pp. 962-983.

[14] Yu, T., Wong, Y.L., Teng, J.G., Dong, S.L. and Lam, E.S.S., "Flexural Behavior of Hybrid FRP-concrete-steel Double-skin Tubular Members", Journal of Composites for Construction, 2006, Vol. 10, No. 5, pp. 443-452.

[15] Han, L.H., Yao, G.H. and Tao, Z., "Performance of Concrete-filled Thin-walled Steel Tubes under Pure Torsion", Thin Walled Structures, 2007, Vol. 45, No. 1, pp. 24-36.

[16] Wang, Q.L., Zhu, H.F. and Gao, Y.F., "Constitutive Relationship of Concrete Confined by Circular CFRP-steel Composite Tube under Concentrical Load", Journal of Shenyang Jianzhu University (Natural Science), 2007, Vol. 23, No. 2, pp. 199-203. (in Chinese)

[17] Han, L.H., Liu, W. and Yang, Y.F., "Behaviour of Concrete-filled Steel Tubular Stub Columns Subjected to Axially Local Compression", Journal of Constructional Steel Research, 2008, Vol. 64, No. 4, pp. 377-387.

[18] Han, L.H., Yao, G.H. and Zhao, X.L., "Tests and Calculations for Hollow Structural Steel (HSS) Stub Columns Filled with Self-consolidating Concrete (SCC)", Journal of Constructional Steel Research, 2005, Vol. 61, No. 9, pp. 1241-1269.

RESEARCH ON EFFECT OF SLIDING BETWEEN HOOP CABLE AND CABLE-STRUT JOINT ON BEHAVIOR OF SUSPEN-DOME STRUCTURES

Hongbo Liu [1] and Zhihua Chen [1,2,*]

[1] *Department of Civil Engineering, Tianjin University, Tianjin 300072, China*
2. Tianjin Key Laboratory of Civil Engineering Structures and New Materials, Tianjin 300072, China
**(Corresponding author: E-mail: zhchen@tju.edu.cn)*

Received: 1 August 2011; Revised: 5 October 2011; Accepted: 21 November 2011

ABSTRACT: For suspen-dome structures, the construction process is very complex and may have an effect on its structural behavior during service time. During construction, a remarkable pre-stressing loss may be induced by sliding friction between hoop cable and cable-strut joint, and the sliding friction can be any value in construction stage and service time. In this paper, the effect of pre-stressing loss and sliding friction during construction on the structural behavior of suspen-dome structures is investigated. The analysis results show that the construction process has a remarkable effect on the structural behavior of suspen-dome structures and a security risk can be induced by it. Therefore, it is suggested that the construction process should be considered in the design process of suspen-dome structures.

Keywords: Suspen-dome structures, Construction process, Pre-stressing loss, Sliding friction, Structural behavior

1. INTRODUCTION

Weight reduction and span increase of structures are typical tendencies in the development of spatial structures, which can be accomplished by the application of new high-strength materials. Steel cable is a high-strength material. It has been widely introduced into traditional steel structures, such as beams, trusses, single-layer lattice shell and barrel vault structure and so on, forming beam string structures [1], truss string structures [1] and suspen-dome structures [2] and cable supported barrel vault structure [3] and so on. Suspen-dome structure is a pre-stressed spatial steel structure and presented by Kawaguchi [2]. It has a good structural behavior under loading and has been widely used in sport facilities, convention & exhibition centers in Japan and China [4,5].

Many investigations have been carried out to reveal the structural behavior of suspen-dome structures through both experiments and numerical analysis [6-14], and these research results have played an important role in suspen-dome constructions. However, with the development of researches and engineering practice, it is found that construction process may have a remarkable effect on the structural behavior of suspen-dome structures. The reasons induced the effect are mainly indicated on two aspects as follows: 1) There is a large pre-stressing loss induced by sliding friction between hoop cable and cable-strut joints during pre-stressing construction; 2) sliding cable-strut joint, recently used in suspen-dome, can be in any state during construction and service time, such as allow hoop cable sliding without friction, allow hoop cable sliding with any friction and don't allow hoop cable sliding and so on [15]. Therefore, it is important to study the effect level of above aspects on the structural behavior in order to give instruction to the suspen-dome structures application.

2. NUMERICAL SIMULATION METHOD OF CABLE SLIDING CONSIDERING FRICTION

Before studying the effect of pre-stressing loss, a numerical simulation method, which can consider the sliding friction, must be found. From the published literatures, four methods is available: 1) coupling the degrees of freedom of hoop cable joint and brace strut lower joint and adjusting stiffness spring element in ANSYS software[13]; 2) modified original cable length method[14]; 3) frozen-heated method[9]; 4) cable-sliding criterion equation[16]. Considering the accuracy and time cost, the cable-sliding criterion equation is used to simulate the sliding friction.

The following is the general procedure to simulate the cable sliding considering the friction in ANSYS:

1) A finite element model is firstly established in ANSYS. Two-node LINK10 elements are adopted to simulate the cable member in suspen-dome structures without considering the sliding behavior between two sides of a cable-strut joint.

2) A nonlinear FE analysis is further conducted to obtain the tensions of all cable elements.

3) If the tensions of both side cables of a cable-strut joint are not in equilibrium, the cable may slide around the joint. The sliding lengths around each joint can be obtained by solving the cable-sliding criterion equations [16]. According to these sliding lengths around each joint, the virtual temperature of both sides of each joint can be evaluated using thermal expansion theory.

4) After that, a virtual temperature is applied to the corresponding cable element. A re-analysis on the suspen-dome structure is fulfilled to obtain the tensions of all cable elements.

5) Finally, the tensions of both sides of cable-strut joint are verified. If they are in equilibrium, the analysis is completed. If not, Step 3 through Step 5 is repeated until the equilibrium is achieved.

3. EFFECT OF PRE-STRESSING LOSS INDUCED BY SLIDING FRICTION

3.1 The Studied Model

In order to study the structural behavior of suspen-dome with sliding cable joint, a model was designed as shown in Fig. 1 and Fig. 2. This suspen-dome structure is with a span of 91.4 m and a rise of 17.03 m. Steel pipes of ϕ 203mm×6mm, ϕ 219mm×7mm, ϕ 245mm×7mm, ϕ273mm×8mm, ϕ299mm×8mm are used as the principal members of the upper single layer shell, and steel pipes of ϕ219mm×7mm are used as vertical struts. Seven radial steel bars (ϕ80mm) and seven hoop cables (ϕ7mm×121) are arranged in the bottom of the structure. The elastic modulus of steel and cable are 2.1×105 N/mm2 and 1.8×105N/mm2, respectively. The boundary conditions are assumed to be pined. The inner hoop cable forces are uniformly 90kN, 140kN, 350kN, 540kN, 630kN, 820kN, 1230kN, when the gravity of steel members and the pre-stressing force were applied on the structure.

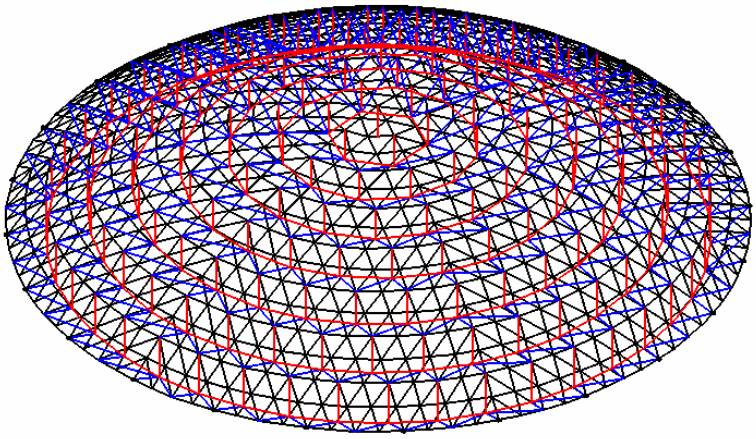

Figure 1. Axonometric View of Suspen-dome Structure

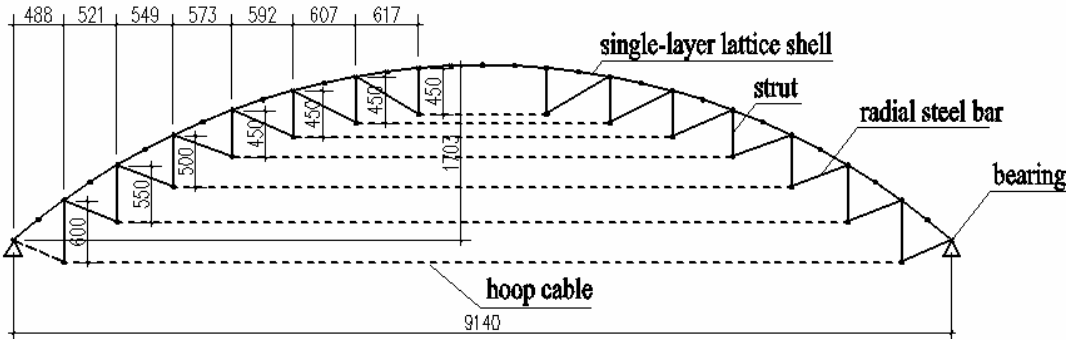

Figure 2. Sectional View of Suspen-dome Structure

3.2 Result Analysis

For the sake of convenient contrast, two construction schemes were studied. One scheme is considering the pre-stressing loss induced by sliding friction (hereinafter referred to as Case 1); the other scheme is not (hereinafter referred to as Case 2). Using the numerical method presented in section 3.1, the pre-stressing construction process was analyzed considering the sliding friction. In this analysis, only gravity and pre-stressing force were considered. And the sliding friction coefficient between hoop cable and cable-strut joint is assumed to be 0.40 based on the site monitoring [13].

For the case1, the maximum inner cable force, minimum inner cable force and the variance from design inner force are listed in Table 1. The inner hoop cable forces referring to Case 2 are also listed in Table 1. It can be seen that the inner cable force for each hoop cables are very no-uniform and the variance from design pre-stressing is up to 71.01% under Case 1, which is induced by sliding friction. In the process of pre-stressing construction by pre-tensioning hoop cables, the pre-stressing of hoop cables away from the tension points was introduced by hoop cable sliding around cable-strut joint; if friction exists between hoop cable and cable-strut joint, the pre-stressing of hoop cable away from tension point is reducing. Therefore, it can be concluded that the sliding friction in pre-stressing construction of suspen-dome structures can induce notable variance.

Table 1. Hoop Cable Force Distribution

Cable groups		1	2	3	4	5	6	7
Case 1	Minimum force (kN）	26.65	76.02	205.06	348.89	452.99	571.29	827.46
	Maximum force (kN）	89.01	131.56	342.18	539.88	583.85	759.58	1127.50
	Variance (%)	71.01	45.98	42.51	35.97	28.48	30.40	32.94
Case 2	Cable force (kN)	91.95	140.72	356.66	544.92	633.37	820.84	1234.00

Note: Cable group 1 is the innermost hoop cables, and Cable group 7 is the outmost hoop cables.

In order to investigate the variance of structural behavior between Case 1 and Case 2 in the service time, the static analysis of suspen-dome were carried out for both cases considering gravity, dead load (1.0 kN/m^2) and live load (0.5 kN/m^2) and pre-stressing force. Compared with the maximum equivalent stress of 88MPa and the maximum node displacement of 30 mm of Case 2, the corresponding values of Case 1 are 126MPa (43.2% increased) and 46 mm (53.3% increased), respectively. Therefore, the pre-stressing loss induced by sliding friction during pre-stressing construction has a remarkable effect on the mechanical behavior of suspen-dome under dead load and live load.

The member number of upper single-layer latticed shell in the studied model in this paper is 3504. The distribution of maximum equivalent stress in upper single-layer latticed shell for both Case 1 and Case 2 are given in Table 2. From Table 2, the member number of which the maximum equivalents stress is larger than 50 Mpa is 771 in Case 2 and corresponding number in Case 1 is 1177, which is 52.66% more than that of Case 2. It is verified that the pre-stressing loss induced by sliding friction during pre-stressing construction has a remarkable effect on the mechanical behavior of suspen-dome in the service time again. Therefore, it is important that there is enough equipment and corresponding technical backup to reduce the pre-stressing loss induced by sliding friction during pre-stressing construction.

Table 2. Distribution of Equivalent Stress for Each Case

	0~50(Mpa)	50~100(Mpa)	≥100(Mpa)
Case 1	2327	1088	89
Case 2	2733	771	0

4. EFFECT OF THE CABLE JOINT STATE

For the new cable-strut joint referred in Section 1 during construction process, it can be locked by clamp plates and the hoop cables can not slide around cable-strut joint in this states; it also can be a state that allows the hoop cables to slide around cable-strut joint with friction. The above states can be obtained by controlling the pressure force between hoop cable and clamp plates. In order to obtain a good state for suspen-dome, it is needed to study the structural behavior of suspen-dome under any states. It is well known that the inner force of each hoop cables is nearly uniform under uniform loads, so the structural behaviors of suspen-some structure with any state of cable-strut joint have not obvious difference. However, there is obvious difference under asymmetrical load, such as half-span load. In this paper, the load combination of uniform load (1.0 kN/m^2) and half-span load (1.0 kN/m^2) was considered in the following analysis.

Based on the pressure force between hoop cable and cable-strut joint, five cases are designed to study the structural behavior of suspen-dome under asymmetrical load:

Case 1: the hoop cables can slide around cable-strut joint with no friction.

Case 2: the hoop cables can slide around cable-strut joint with friction, and the friction coefficient is 0.15.

Case 3: the hoop cables can slide around cable-strut joint with friction, and the friction coefficient is 0.30.

Case 4: the hoop cables can slide around cable-strut joint with friction, and the friction coefficient is 0.45.

Case 5: the hoop cables can not slide around cable-strut joint.

The member number of upper single-layer latticed shell in the studied model in this paper is 3504. The distributions of maximum equivalent stress for each member in upper single-layer latticed shell for Case 1 to Case 5 are given in Table 4. The maximum equivalent stress and nodal displacement in upper single-layer latticed shell for Case 1 to Case 5 are given in Table 5.From Table 4 and Table 5, it is clear that:

1) The structural behavior of Case 5 (hoop cable can not slide around cable-strut joint) is best and Case 1(hoop cable can slide around cable-strut joint with no friction) is worst;

2) The friction coefficient between hoop cables and cable-strut joints is larger, the structural behavior of suspen-dome structures is better;

3) Compared with the maximum equivalent stress of 106MPa and the maximum node displacement of 26 cm of Case 5, the corresponding values of Case 1 are 216MPa (103.77% increased) and 70 cm (169.23% increased), respectively.

Therefore, it is clear that when the hoop cables can not slide around the cable-strut joints, the structural behavior of suspen-dome structures is best.

Table 3. Distribution of Equivalent Stress for Each Case

Stress range (Mpa)	0~30	30~6	60~90	90~120	120~150	≥150
Case 1	904	1644	626	172	64	94
Case 2	952	1817	501	118	74	42
Case 3	1162	1724	472	88	58	0
Case 4	1362	1740	360	42	0	0
Case 5	1143	1426	591	44	0	0

Table 4. The Maximum Equivalent Stress and Nodal Displacement for Each Case

	Case 1	Case 2	Case 3	Case 4	Case 5
maximum nodal displacement（cm）	70	57	47	40	26
maximum equivalent stress（Mpa）	216	182	149	116	106

6. CONCLUSIONS

In this paper, a systematic study has been carried out in order to reveal the effect of construction process on the structural behavior of suspen-dome structures, and the following conclusions were obtained from the stability analysis results:

1) The pre-stressing loss induced by sliding friction during pre-stressing construction has a remarkable effect on the mechanical behavior of suspen-dome under dead load and live load.

2) The structural behavior of suspen-dome structure is different under asymmetrical load when the sliding friction coefficient between hoop cable and cable-strut joint is changing. When the sliding friction coefficient is large enough to make the hoop cable not sliding around joint, the structural behavior is the best case; when the sliding friction coefficient is equal to zero, the structural behavior is the worst case.

3) The construction process of suspen-dome structures has a remarkable effect on its structural behavior during service time under dead load and live load.

ACKNOWLEDGEMENTS

This work is sponsored by the Committee of National Natural Science Foundation of China (Grant No.: 50778122) and the Program for New Century Excellent Talents in University of Ministry of Education in China (Grant No.: NCET-06-0228).

REFERENCES

[1] Saitoh, M. and Okada, A., “The Role of String in Hybrid String Structure”, Engineering Structures, 1999, Vol. 21, No. 8, pp. 280–284.

[2] Mamoru Kawaguchi, M., Abe, M, Hatato, T., et al., “On a Structural System “suspen-dome” System”, Proc. of IASS Symposium, Istanbul, 1993, pp. 523-530.

[3] Chen, Z.H., Qiao, W.T. and Yan, X.Y., “Cable Supported Barrel Vault Structure System and Research on Mechanics Feature”, Advanced Steel Construction, 2010, Vol. 6, No. 3, pp. 867-878.

[4] Chen, Z.H., Liu, H.B., Wang, X.D., et al., “Review and Forecast of Suspen-dome Structures”, Journal of Building Structures, 2010, Supplementary Issue Vol. 1, pp. 210-215. [In Chinese]

[5] Zhang, Y.G., “Development of Cable-supported Structures in the Last Ten Years (2) : Application and Developments of Two-way Cable-supported Structures and Spatial Cable-supported Structures”, Industrial Construction, 2009, Vol. 39, No. 11, pp. 93-99. [In Chinese]

[6] Shi, K.O., Guo, Z.X. and Luo, B., “Method for Determining the Prestress of Elliptical Suspen-dome Structures”, China Civil Engineering Journal, 2010, Vol. 43, No. 9, pp. 88-98. [In Chinese]

[7] Kang, W.J., Chen, Z,H. and Lam, H.F., et al., “Analysis and Design of the General and Outmost-ring Stiffed Suspen-dome Structures”, Engineering Structures, Vol. 25, 2003, pp. 1685-1695.
[8] Kitipornchai, S., Kang, W.J., Lam. H.F., et al., “Facters Affecting the Design and Construction of Lamella Suspen-dome Systems” Journal of Constructional Steel Research, 2005, Vol. 61, No. 6, pp. 764-785.
[9] Cui, X.Q. and Guo, Y.L., “Influence of Gliding Cable Joint on Mechanical Behavior of Suspen-dome Structures”, International Journal of Space Structure, 2004, Vol. 19, No. 3, pp. 149-154
[10] Cao, Q.S. and Zhang, Z.H., “A Simplified Strategy for Force Finding Analysis of Suspen-domes”, Engineering Structures, 2010, Vol. 32, No. 1, pp. 306-310.
[11] Zhang, Z.H., Cao, Q.S., Dong, S.L. and Fu, X.Y., “Structural Design of a Practical Suspen-dome”, Advanced Steel Construction, 2008, Vol. 4, No. 4, pp. 323-340.
[12] Zhang, A.L., Liu, X.C., Wang, D.M., et al., “Static Experimental Study on the Model of the Suspen-dome of the Badminton Gymnasium for 2008 Olympic Games”, Journal of Building Structures, 2007, Vol. 28, No. 6, pp. 58-67. [In Chinese]
[13] Wang, S., Zhang, G.J., Zhang, A.L., et al., “The Prestress Loss Analysis of Cable-strut Joint of the Badminton Gymnasium for 2008 Olympic Games”, Journal of Building Structures, 2007, Vol. 28, No. 6, pp. 39-44. [In Chinese]
[14] Zhang, G.F., Dong, S.L., et al., “Research on Sliding Cable in Construction of Suspen-dome Structures”, Journal of Zhejiang University (Engineering Science) 2008, Vol. 42, No. 6, pp. 1051-1057. [In Chinese]
[15] Liu, H.B., Chen, Z.H., “Influence of Cable Sliding on the Stability of Suspen-dome with Stacked Arches Structures”, Advanced Steel Construction, 2012, Vol. 8, No. 1, pp. 54-70
[16] Chen, Z.H., Liu, H.B., Wang, X.D. and Zhou, T., “Establishing and Application of Cable-Sliding Criterion Equation”, Advanced Steel Construction, 2011, Vol. 7, No. 2, pp. 131-143.

STRENGTH AND DUCTILITY EVALUATION METHOD FOR STEEL BRIDGE PIER FRAMES CONSIDERING EFFECT OF SHEAR FAILURE

L. Kang [1] and H.B. Ge [2, *]

[1]*Post Doctoral Researcher, Dept. of Civil Engineering, Meijo University, Nagoya, 468-8502, Japan*
E-mail: connielan@tom.com
[2]*Professor, Dept. of Civil Engineering, Meijo University, Nagoya, 468-8502, Japan.*
**(Corresponding author: E-mail: gehanbin@meijo-u.ac.jp)*

Received: 25 August 2011; Revised: 4 October 2011; Accepted: 21 November 2011

ABSTRACT: This paper presents a practical evaluation method for predictions of strength and ductility capacity of steel bridge pier frames including effects of shear failure. The shearing behavior of structure is simulated by introducing membrane and truss elements at the mid-span of girder. In order to investigate the effects of shear failure on the strength and ductility capacity, a series of pushover analyses are carried out, comparisons between different methods are conducted and effects of sensitive parameters are discussed. From these investigations and discussions, the availability of the shear ductility prediction method proposed in this study is verified, especially for the unstiffened cases with large web width-thickness ratio of girder. Furthermore, a boundary between bending and shear failure modes is obtained based on discussions.

Keywords: Steel bridge pier frame, Shear failure, Bending failure, Ductility capacity, Membrane element, Web width-thickness ratio of beam

1. INTRODUCTION

Steel bridge piers suffered severe seismic damage during the Hyogoken-Nanbu earthquake, on January 17th, 1995. Some of steel bridge piers' failure during this earthquake mainly resulted from the shear local buckling, as shown in Figure 1. Severe shear damage in such structures caused considerable disruption to the relief work. This resulted in a consensus to be reached that the seismic capacity, especially the ductility, of such structures needs further and extensive investigation. Because no similar damage ever being reported in Japan before, shear failure, especially at the mid-span of girder, was not considered in seismic design prior to this earthquake. However, since then the necessity of accounting for the effect of shear failure in the phase of seismic design has been gradually realized. In the past years, the performance of bending failure has been deeply investigated [1-6]. For the shear failure of steel pier frames due to the shear local buckling, the experimental investigations have been conducted [7, 8], but the corresponding evaluation method is sparse and specific quantitative criterion to relate these failure modes to steel bridge piers is lacking. Besides, for steel bridge pier frames, both bending and shear failure verifications should be conducted in order to identify which type of failure will occur, especially during earthquake loading [9-11].

The shear failure of column-beam joint in building frames has been regarded as important damage mode [12, 13]. Because of the strengthening measures of pier-girder joint in steel bridge pier frames, large shear deformation may occur at the mid-span of girder [14]. Similar to the previous research [14-18], the strength and ductility should be considered and verified at the same time. A pushover analysis is terminated when any of the structure's failure criterion is satisfied and this state is taken as the ultimate state of the structure, based on which the ductility capacity of the structure can be determined. During the past years, there is a considerable amount of literatures on failure criterion. The bending failure criterion has been deeply studied in previous studies [1, 3-5, 19]. Besides, the shear failure criterion was studied [20, 21]. Although a simple analytical model

considering shear deformation was discussed by Chusilp and Usami [21], the complete pushover analysis including shear failure for steel bridge pier frames has not been conducted because of the limitation of previous simulation model. The effect of shear failure on the ductility capacity of structure has not been studied in the previous research. In recent years, with the development of computational technology, the strength and ductility including effect of shear deformation and failure can be calculated and predicted accurately and easily. In the previous studies [20, 21], parameter analysis of shear deformation has been done and these results can provide basis for the proposed study. The aim of this study is to provide an analytical model to check and verify the strength and ductility including bending and shear failure modes for steel bridge pier frames more effectively.

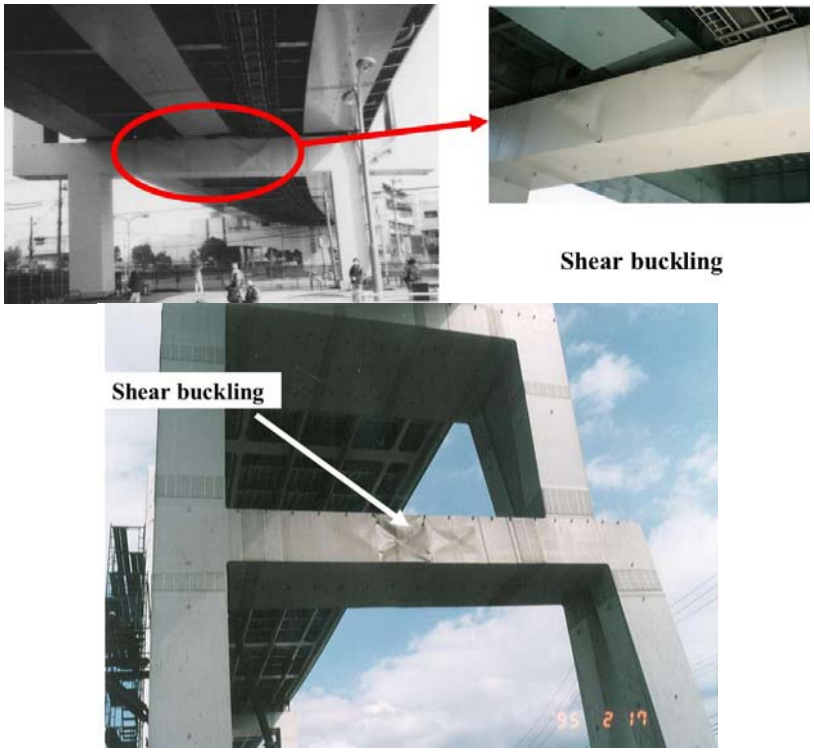

Figure 1. Examples of Shear Failure in Damaged Steel Bridge Pier Frames in the 1995 Kobe Earthquake

Because of the aforementioned lack of verification method about strength and ductility evaluation including shear failure in steel bridge pier frames, a hybrid model including beam, membrane and truss elements is proposed in this paper and a series of pushover analyses are carried out based on this model. First of all, a so-called MB model is established in section 2, in which the details including finite element model, dimensions, cross section, constraint between different elements and so on will be given. Secondly, the previous failure criteria are stated. Furthermore, comparisons between the proposed and previous models' results as well as sensitive parameter analysis are conducted. From the results and discussions, a boundary between bending and shear failure modes is obtained.

2. FINITE ELEMENT ANALYTICAL MODEL OF STEEL BRIDGE PIER FRAMES

In this study, the ABAQUS finite element software [22] was utilized to investigate the structural behavior of steel bridge pier frames. Two different finite element analytical models are established, which are BB and MB models, respectively, as shown in Figure 2. In which, the BB model only includes the beam element, and the MB model consists of the membrane and truss elements at the

mid-span of girder except for the beam element. In the previous study [5], the BB model was employed to evaluate the bending performance of steel structures. In both two models, the P-△ effect is taken into account, and the local buckling is ignored. For different models, the effect of shear behavior is taken into account in different ways. In the BB model, the shear deformation is included by using a type of beam element (i.e., B21) based on the Timoshenko beam theory, and the effect of shear failure is not considered. However, in the MB model, the shear deformation is also considered by introducing the membrane element at the mid-span of girder, which can take the effect of shear failure into account. The BB model only with the beam element can't take the effect of shear failure (as shown in Figure 1) into consideration, because the beam element can't accurately simulate the shear buckling occurring at the mid-span of girder. In this study, because the MB model with membrane element at the mid-span of girder can reveal the shear failure more comprehensively and correctly during pushover analysis, the MB model is employed to replace the traditional model (BB model), and the corresponding seismic verification method including the effect of shear failure by using this hybrid analytical model is developed and established.

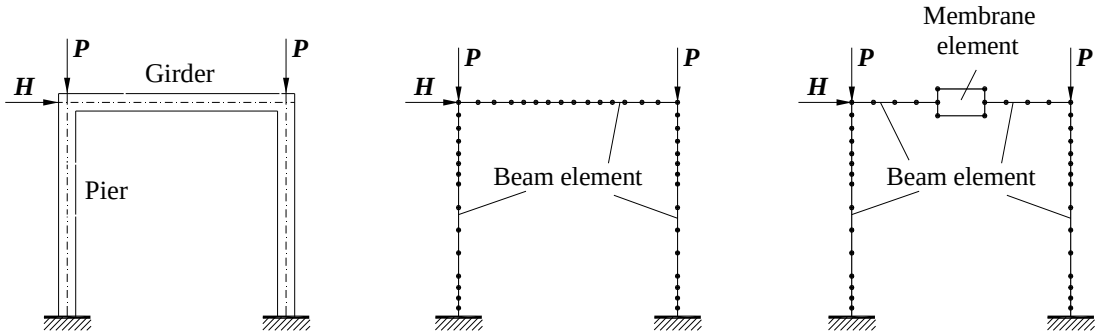

(a) Portal Frame of Steel Bridge Pier (b) BB Model (c) MB Model

Figure 2. Steel Bridge Pier Frame

2.1 Analytical Model

2.1.1 The analytical model only including beam element (BB model)

The beam element (B21) in ABAQUS, which accounts for the shear deformation based on the Timoshenko beam theory, is utilized in this model, and each of girder and piers is divided into 15 beam elements [23]. Since this type of portal frame is commonly subjected to heavy loading, the plates at the pier-girder connections should be strengthened by doubling the plate thickness in order to avoid shear failure [14].

2.1.2 The finite element model with membrane element at the mid-span of girder (MB model)

In this analytical model, the beam element at the mid-span of girder is replaced by the membrane and truss elements. The four-node membrane element (M3D4) in ABAQUS, which has two degrees of freedom at each node, is adopted at the mid-span of girder, and in other parts of beam member the Timoshenko beam element is utilized (same to the BB model). Each pier member is divided into 15 beam elements [23]. The distance between the pier-girder joint and the membrane element is the length of 3 beam elements. Besides, same to the BB model, the plates at the pier-girder connections should be strengthened by doubling the plate thickness in order to avoid shear failure of joints [14]. The only difference between the BB model and MB model is the element type to model the mid-span girder. In order to predict the shear failure mode of steel bridge frame structure, the MB model consists of the membrane and truss elements except for the beam element, and it is then regarded as a hybrid model including three types of elements.

2.2 Dimensions of Analytical Model

In this study, a series of finite element analyses are carried out. As shown in Figure 3, the label of analyzed models (e.g., US35-70A and SS35-40B) is defined as follows. The first letter indicates the type of cross section, where “U” and “S” represent unstiffened box section and stiffened box section, respectively. The following letter S indicates steel bridge pier frame. Accordingly, “US” and “SS” refer to steel bridge pier frames with unstiffened steel box section and stiffened steel box section, respectively. The next two numbers denote the flange width-thickness ratio of column, R_f, and the web width-thickness ratio of beam, R_{wb}, respectively. They are 100 times larger than the actual value. The last letter (A or B) represents the beam length, where “A” means the length of beam is 8300 mm, and “B” indicates the length is 12450 mm. In other words, the values of l/h in two cases are 0.769 and 1.15, respectively. Additionally, for some unstiffened cases, in order to evaluate the effect of stiffened measure on the failure mode, stiffeners are employed and “-S” and “-2S” indicate one stiffener and two stiffeners to strengthen the unstiffened specimens, respectively. Some main parameters of finite element analysis are listed in Table 1. Equivalent web width-thickness ratios of beam R_{wb} of -S and -2S cross sections are given in Table 2. A total of 38 different cases are analyzed in this study.

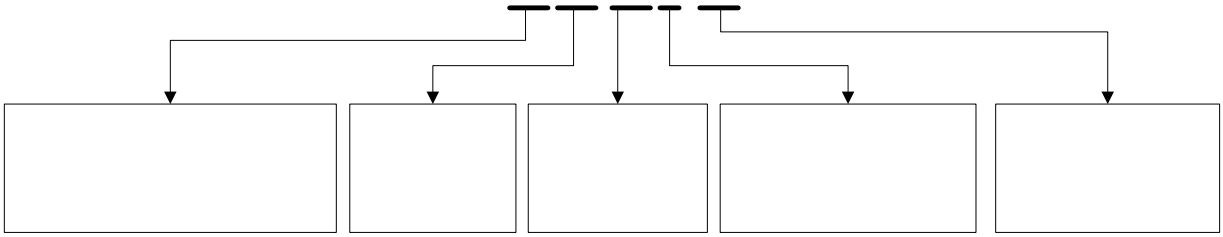

Figure 3. Label of Analytical Cases

Table 1. Main Parameters for Finite Element Analysis

Parameters	Range
Column height, h (mm)	10800
Beam length, l (mm)	8300,12450
Flange width-thickness ratio of column, R_f	0.35~0.45
Web width-thickness ratio of beam, R_{wb}	0.4~1.5
Yield stress of steel (MPa)	314
Stiffness ratio of column stiffener	3.0
Stiffness ratio of beam stiffener	1.0

Table 2. Web Width-thickness Ratio of Beam R_{wb} of -S and -2S Cross Sections

Specimens	US35-60A-S	US35-70A-S	US35-100A-S	US35-150A-S
R_{wb}	0.313	0.372	0.573	0.860
Specimens	US45-60A-S	US45-70A-S	US45-100A-S	US45-150A-S
R_{wb}	0.308	0.363	0.540	0.811
Specimens	US35-100A-2S	US35-150A-2S		
R_{wb}	0.591	0.549		

US35-

US:Unstiffened box section
of steel bridge pier frame
SS: Stiffened box section of

Flange width-
thickness ratio
of column

Web w
thickne
of bean

2.3 Cross Section of Steel Bridge Pier Frame

For the BB model, the beam element at the mid-span of girder is shown in Figure 4(a). In which, m, n are the two nodes of beam element, and the cross section of pier and girder members are introduced by sectional properties and parameters. For the beam cross sections, the web plate of beam is unstiffened belonging to US model and the web plate of beam is stiffened belonging to SS model. A box section with longitudinal stiffeners (SS model) is one of the most common cross-sectional types used for thin-walled steel structures. In the analysis of such structures, the original stiffened section can certainly be used but, for simplification, an equivalent unstiffened section is introduced [5].

However, in the MB model, the beam element at the mid-span of girder is replaced by membrane and truss elements, as shown in Figure 4(b). It is well-known that shear local buckling may occur at the mid-span of girder. In order to accurately predict the shear failure of steel bridge pier frames, one membrane and two truss elements are introduced into the MB model. The analytical method may be suitable for simulating the in-plane deformation of pushover analysis because the out-of-plane deformation can't be taken into account in membrane element. In addition, the two truss elements are used to model the flange plate at the mid-span of girder because the flange works mainly in tension or compression modes. In the Figure 4(b), m, n are the two nodes of side beam elements, and i, j, k, l are the four nodes of membrane element. Membrane and truss elements share the same nodes, in which i and j are two nodes of one truss element, l and k are two nodes of the other one. The thickness of membrane element is twice of the thickness of web plate based on equivalent cross section method. Cross section area of truss element is equal to that of flange plate of beam.

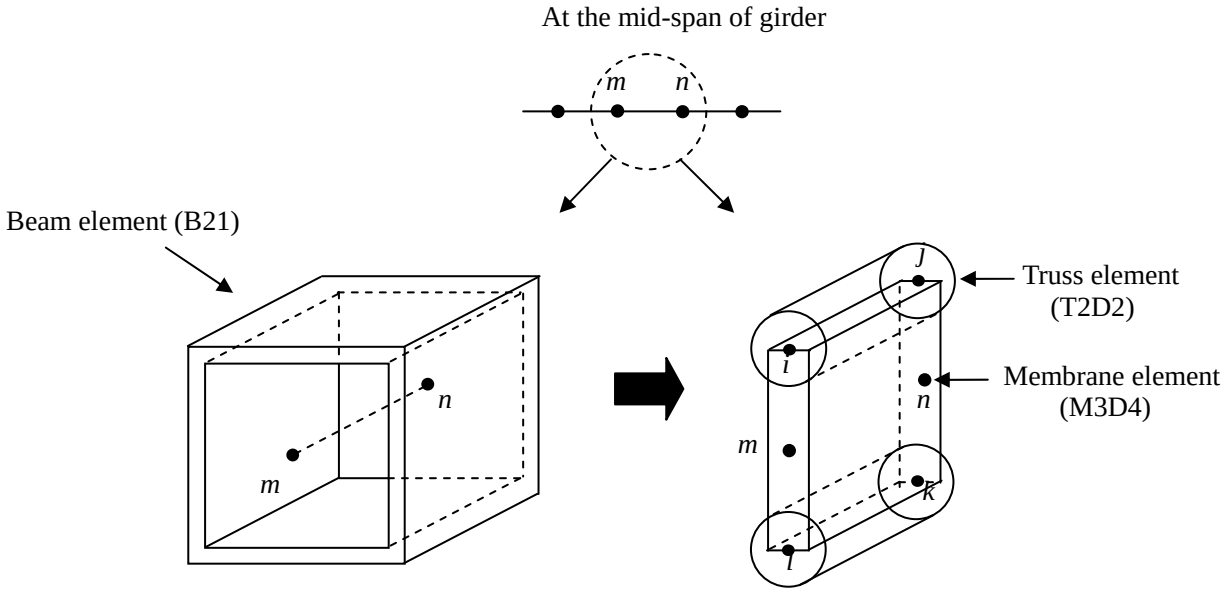

(a) Beam Element of BB Model (b) Membrane and Truss Elements of MB Model

Figure 4. Difference between BB Model and MB Models

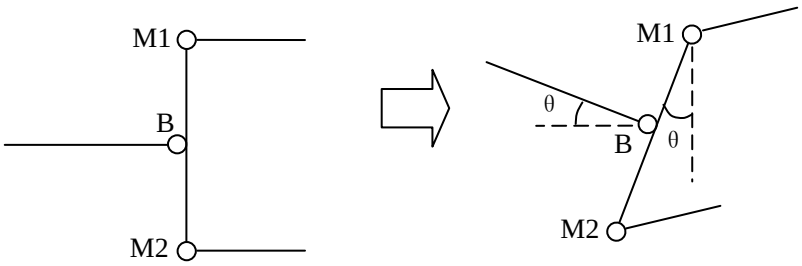

(a) Before Deformation (b) After Deformation

Figure 5. Connection between Membrane and Beam Elements

2.4 Constraint between Membrane and Beam Elements

In the proposed analytical model, the connection between membrane and beam elements is established based on the assumption of plane cross section. In Figure 5, B is the node of beam element, and M1 and M2 represent the nodes of membrane element. There are two following constraint conditions:

(1) The length of the connection part (the length between nodes M1 and M2 in Figure 5), which connects membrane element with beam element, is constant;
(2) At the connection part between membrane and beam elements, the rotation of beam element node B is equal to the rotations of the two nodes (M1 and M2) of membrane element.

The displacement relationship between beam and membrane elements can be expressed as follows:

$$u_M - u_B = (X_A - X_B)(\cos\theta - 1) - (Y_M - Y_B)\sin\theta \tag{1}$$

$$v_M - v_B = (X_M - X_B)\sin\theta + (Y_M - Y_B)(\cos\theta - 1) \tag{2}$$

in which, u and v denote the displacements of X-axis and Y-axis, respectively. X, Y represent the coordinate magnitudes of X-axis and Y-axis after deformation, respectively. The subscript M expresses that the variable belongs to membrane element, and the subscript B expresses that the variable belongs to beam element. θ denotes the rotation of beam element node.

2.5 Weight of Upper Structure

In this study, the weight of upper structure is regarded as vertical loads applying on the steel bridge pier frame. Based on the seismic coefficient method [24], the weight of upper structure is calculated. Considering a certain safety coefficient (in this study, is 1.14, same to the reference [23]), the analytical model is subjected to the horizontal load $H = 0.2P$ and the vertical loads of P at the top of the steel bridge pier frame. The weight of upper structure is obtained. The range of P/P_y is from 0.28 to 0.5.

3. FAILURE CRITERION

The pushover analysis involves applying monotonic lateral loads to approximately simulate the horizontal displacements of steel bridge pier frames. In somewhat different formats, the pushover analysis has been proposed and evaluated mainly as a demand prediction tool for concrete structures [25-27]. In recent work of the authors [23, 28], the pushover analysis has been proposed for steel frame structures serving for both the capacity evaluation and demand prediction. During

the pushover analysis, a proper failure criterion is necessary. For RC structures, the failure criterion is usually based on the rotational capacity of plastic hinges. However, the capacity of frame structures composed of thin-walled steel members is mainly controlled by local buckling. In this paper, a failure criterion including bending and shear failure modes is employed to evaluate bending and shear failure modes. Besides, the locations of failure verification, the damage degree and the effective failure length are described in the following sections.

3.1 Location of Failure Verification

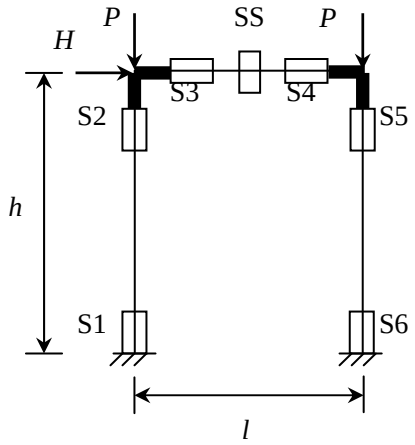

Figure 6. Location of Failure Verification

With the increase of loading, the failure verification locations become wider. Because the steel frame is under combined loading of bending and compression, the compression strain is raised [5]. To completely investigate the bending behavior of steel frames, six bending verification locations (S1~S6) are determined as shown in Figure 6, in which l is the length of girder, h is the height of pier, P and H are vertical and horizontal loads, respectively. Because the stiffness of the pier-girder joint is relatively large (as described in Sections 2.2 and 2.3), in this study, SS at the mid-span of girder is regarded as the shearing verification location, as shown in Figure 6.

3.2 Failure Verification

3.2.1 Bending failure verification

In the proposed ductility evaluation method, the bending failure criterion can be described by a damage index D_{sb}, which is defined:

$$D_{sb} = \frac{\varepsilon_{a,s}}{\varepsilon_{u,s}} \tag{3}$$

when D_{sb} reaches 1.0, the bending ultimate state of structure is considered to be attained. Here, $\varepsilon_{a,s}$ represents the average strain of the compressive flange (for the box section) over a certain effective failure length that will be discussed further below. The value $\varepsilon_{u,s}$ denotes the failure strain and, to define it, the empirical formulas obtained from stub-column analyses are employed.

The empirical formulas of the failure strains were proposed for thin-walled steel stub columns with box sections that are subjected to compression and bending. The behavior of box-sectioned stub-columns with and without longitudinal stiffeners has been extensively investigated under combined compression and bending, and corresponding empirical equations for the failure strains were given as follows [5]:

For unstiffened box stub-columns:

$$\frac{\varepsilon_{u,s}}{\varepsilon_y} = \frac{0.108\left(1-N/N_y\right)^{1.09}}{\left(R_f-0.2\right)^{3.26}} + 3.58\left(1-N/N_y\right)^{0.839} \le 20.0 \tag{4}$$

For stiffened box stub-columns:

$$\frac{\varepsilon_{u,s}}{\varepsilon_y} = \frac{0.8\left(1-N/N_y\right)^{0.94}}{\left(R_f\cdot\bar{\lambda}_s^{0.18}-0.168\right)^{1.25}} + 2.78\left(1-N/N_y\right)^{0.68} \le 20.0 \tag{5}$$

in which, P = axial force; P_y = squash load; R_f = flange width-thickness ratio parameter; and $\bar{\lambda}_s$ = stiffener's slenderness ratio parameter. The definitions of R_f and $\bar{\lambda}_s$ can refer to the reference [19]. In this study, R_f = 0.3~0.7, N/N_y = 0.0~0.5. When the axial force is a tension, it will be taken to be zero.

3.2.2 Shear failure verification

In the proposed ductility procedure, the shear failure criterion can be described by a damage index D_{ss}, which is defined:

$$D_{ss} = \frac{\gamma_s}{\gamma_{u,s}} \tag{6}$$

in which, γ_s is the shearing strain of membrane element, $\gamma_{u,s}$ is the ultimate strain obtained by the equations (7) and (8). Simple formulas are proposed for estimating the ductility capacity of box girders with and without longitudinal web stiffeners as follows [21, 29]:
For unstiffened cross section:

$$\frac{\gamma_{u,s}}{\gamma_y} = \frac{0.142}{\left(R_{wb}-0.18\right)^{4.0}} + 4.0 \le 20.0 \tag{7}$$

For stiffened cross section:

$$\frac{\gamma_{u,s}}{\gamma_y} = 2.5 + \frac{0.5}{R_{wb}^{6.0}} \le 20.0 \tag{8}$$

R_{wb} is the web width-thickness ratio of box girders. The limit scope of the equation (8) is $\gamma_{ws} \ge \gamma_{ws}^{*}$, $1.0 \le \alpha_{wb} \le 2.0$. α_{wb} is the web length-width ratio of the girder. The details can refer to the references [21, 29].

3.3 Effective Failure Length

The effective failure length l_e of a box-sectioned member adopted in this method is assumed as l_e = min{0.7B, l_d} where B is the flange width and l_d is the distance between two adjacent diaphragms [5]. For pipe section stub-columns in compression and bending, an empirical equation for the critical length (i.e., the length giving the lowest strength) was proposed by Gao et al. [3], and this length is found to be about half of the mode length of collapse in local buckling (i.e., the so-called elephant foot bulge) observed in long columns with pipe sections under cyclic lateral loading [30].

On this basis, a modified equation (approximately doubling the critical length equation of short cylinders) is employed to define the effective failure length of thin-walled pipe section structures, which is given by Zheng et al. [5]:

$$l_e = 1.2\left(\frac{1}{R_t^{0.08}} - 1\right)d \tag{9}$$

The critical parts could be in more than one place in a framing structure, and all of them should be checked. In a thin-walled steel structure, the excessive deformation tends to intensify in a local part and consequently the redistribution of the stress becomes unexpected. Thus, once the failure criterion at any one of the critical parts is satisfied, the ultimate state of such a structure is thought to be reached.

4. RESULTS AND DISCUSSIONS

The purpose of this study is to propose an improved analytical model and to evaluate the bending and shear failure modes of steel bridge pier frames by using the proposed model. Therefore, a hybrid model including membrane and truss elements at the mid-span of girder is developed. In this section, first of all, by the comparison of the results between MB and BB models, the reliability of the proposed model is verified. Next, by analyzing the parameters' effect, the relationship between structural parameters and shear failure of steel bridge pier frames is investigated. Finally, by utilizing the proposed method, the cases with stiffened and unstiffened plates are analyzed, and the influences of stiffened measure on the ductility evaluation and failure mode are investigated.

4.1 Comparison between MB and BB Models' Results

Table 3. Comparison of Different Models' Ductility Capacity

Specimens	BB model δ_{ub}/δ_y	MB model δ_{ub}/δ_y	MB model δ_{us}/δ_y	Specimens	BB model δ_{ub}/δ_y	MB model δ_{ub}/δ_y	MB model δ_{us}/δ_y
US35-40A	4.74	4.73	14.1	SS35-40A	3.28	3.96	8.67
US35-50A	4.65	4.71	6.14	SS35-50A	3.37	3.82	9.50
US35-60A	4.48	4.72	3.37	SS35-60A	3.22	3.52	7.13
US35-70A	4.25	4.84	2.78	SS35-70A	3.22	3.28	4.85
US35-100A	3.40	4.45	2.70	SS45-40A	2.48	2.53	6.07
US35-150A	3.42	4.95	2.01	SS45-50A	2.34	2.36	5.98
US45-40A	2.93	2.92	6.86	SS45-60A	2.34	2.34	4.85
US45-50A	2.81	2.93	4.02	SS45-70A	2.34	2.34	3.59
US45-60A	2.75	2.97	2.53	SS35-40B	3.99	3.96	
US45-70A	2.63	2.90	2.03	SS35-50B	3.55	3.55	18.97
US45-100A	2.50	2.89	1.90	SS35-60B	3.57	3.53	11.09
US45-150A	2.47	3.03	1.41	SS35-70B	3.53	3.49	7.92
US35-60A-S	4.53	4.50	27.9	SS45-40B	2.66	2.63	24.4
US35-70A-S	4.21	4.20	19.1	SS45-50B	2.57	2.55	14.7
US35-100A-S	3.42	3.94	7.65	SS45-60B	2.47	2.42	7.26
US35-150A-S	3.49	4.56	2.43	SS45-70B	2.43	2.42	4.97
US45-60A-S	2.74	2.74	12.9				
US45-70A-S	2.66	2.72	9.33				
US45-100A-S	2.47	2.61	5.72				
US45-150A-S	2.51	2.87	1.96				
US35-150A-2S		4.45	5.93				
US45-150A-2S		2.83	4.79				

Notes: Gray section means the minimum value between δ_{ub}/δ_y and δ_{us}/δ_y of MB model.

The computational results for the case of US35-70A by using MB and BB models are shown in Figure 7. Firstly, Figure 7(a) indicates the horizontal load versus horizontal displacement curves obtained from the MB and BB models. It demonstrates the relationship between H/H_y (H is the horizontal load, H_y is the horizontal yield load) and δ/δ_y (δ is the horizontal displacement, δ_y is the horizontal yield displacement) for the steel bridge pier frames. Secondly, Figure 7(b) illustrates the damage degree of steel frame versus horizontal displacement curves obtained from the finite element analysis of MB model. In Figure 7(b), the damage degrees of S2~S4 (S1~S6 are six locations of failure verification as shown in Figure 6) are relatively small, and then the magnitudes of S2~S4 are omitted in Figure 7(b). Lastly, Figure 7(c) demonstrates the damage degree versus horizontal displacement curves of the BB model. Table 3 reveals the ductility capacity of all the analytical examples obtained from finite element analyses of BB and MB models. δ_{ub}/δ_y and δ_{us}/δ_y represent the ratios of bending and shear ultimate-to-yield horizontal displacements, respectively. In this study, they are termed as the bending ductility and shear ductility, respectively.

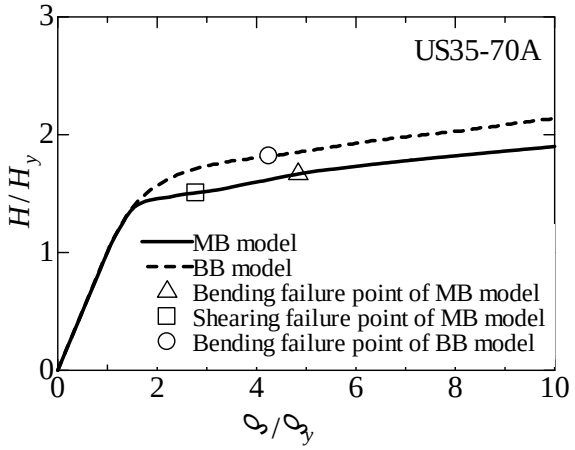

(a) Horizontal Load-displacement Curves and Failure Points of MB and BB Models

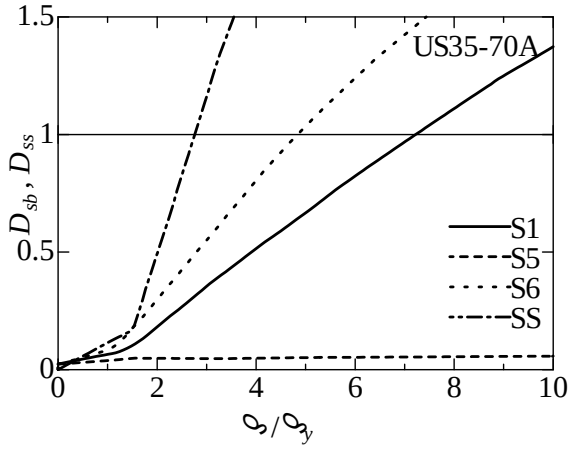

(b) Damage degree of MB Model

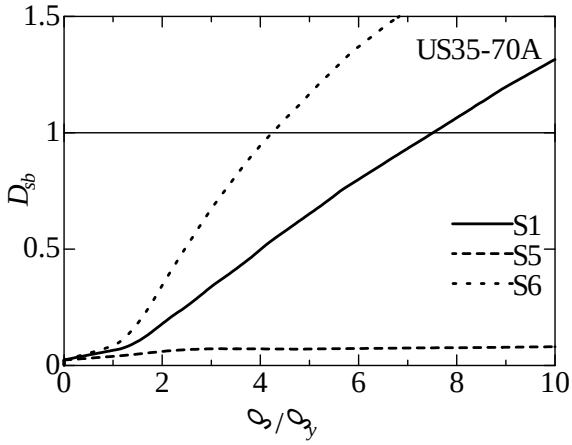

(c) Damage Degree of BB Model

Figure 7. Horizontal Load Displacement Curves and Damage Degree of MB and BB Models

Based on the analytical results of US35-70A as shown in Figure 7, the web width-thickness ratio of beam is comparatively large, and shear failure is predicted to occur at the mid-span of girder. Figure 7(a) reveals that the shear failure occurs before bending failure during the pushover analysis of MB model, and the steel frame may encounter shear failure firstly. Besides, the horizontal displacements of the MB model in this study are larger than that of BB model obtained from the previous method, which is used to evaluate the bending performance. From the analytical responses of Figure 7(b), we can observe that the shear damage degree of SS increases more quickly than the bending damage degree of other locations. Individual differences in simulation results may reflect differences in analytical models, specifically in the damage degree and horizontal displacement. In conclusion, the previous method, which only consists of beam element, can't be employed to predict the shear failure of steel bridge pier frames.

Furthermore, some differences may exist in the load-displacement curves between MB and BB models as shown in Figure 7. On one hand, when the magnitude of δ is near to $1.7\delta_y$, the strength of BB model increases continuously and smoothly, however, for MB model the same phenomenon does not exist. It demonstrates that the web plate at mid-span of MB model's girder has reached the ultimate shear state. Because the shear failure mainly results in the horizontal displacement of steel frames, the strength increase will be delayed. On the other hand, the bending failure points obtained from MB and BB models are different. The large width-thickness ratio parameter leads to the decrease of shearing strength, and meanwhile the bending plastic damage may be delayed during the bending verification procedure because of the relatively large bending plastic deformation capacity. Consequently, for the cases of shearing beam with large width-thickness ratio parameter, the prediction precision of its failure mode will be improved by using the proposed method in this study.

4.2 Effect of Web Width-thickness Ratio of Beam R_{wb}

Relationships between horizontal displacement and web width-thickness ratio of beam, R_{wb}, are illustrated in Figure 8. The shear ductility capacity of steel bridge pier frames is evaluated, and can be expressed as δ_{us}/δ_y. The results of unstiffened and stiffened models are shown in Figure 8, from which it is observed that the shear ductility decreases with the increase of R_{wb}. The similar conclusion is obtained from the previous research [20, 21]. From the results of Figure 8, the shear ductility capacity of the examples with the flange width-thickness ratios of column R_f = 0.35 is relatively larger compared with the examples with R_f = 0.45. Based on the stiffness matching theory, for these analytical examples, the web width-thickness ratio of beam corresponding to large flange

width-thickness ratio of column should be relatively large. Accordingly when the magnitude of model's R_f is equal to 0.45, its R_{wb} should be relatively large. In other words, when the web plate of beam is thick, the shear ductility capacity of steel bridge pier frames might be large. The similar conclusion has been demonstrated in the previous study [20].

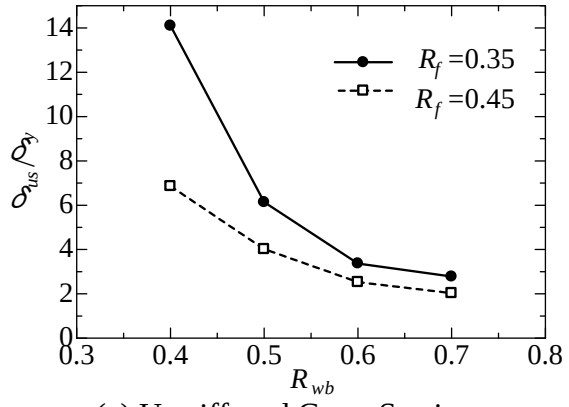

(a) Unstiffened Cross Section

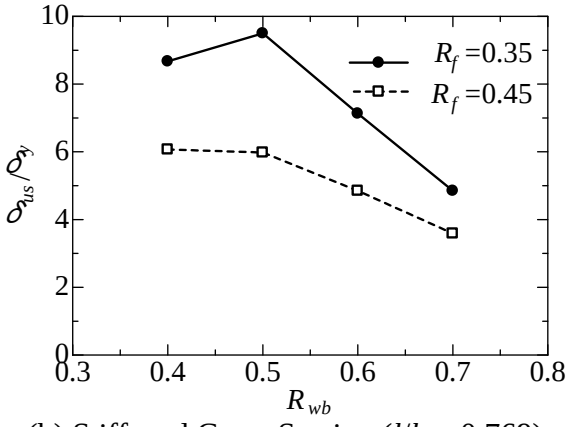

(b) Stiffened Cross Section (l/h = 0.769)

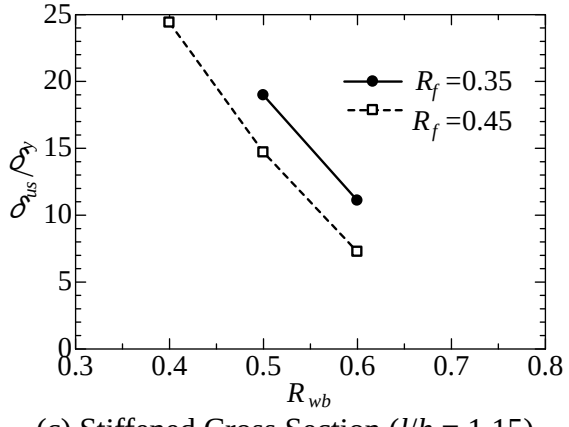

(c) Stiffened Cross Section (l/h = 1.15)

Figure 8. Effect of Web Width-thickness Ratio of Beam, R_{wb}, on Shear Ductility Capacity of Steel Frames

4.3 Comparison between Bending and Shear Failure Modes

The horizontal displacements versus web width-thickness ratio of beam R_{wb} curves are illustrated in Figure 9 obtained from the unstiffened cases. It is observed that the bending ductility of unstiffened structures decreases with the increase of R_{wb}, however, the shear ductility basically

retains constant with the increase of R_{wb}. When R_{wb} is larger than 0.6, although the ultimate bending displacement is near to the ultimate shear displacement, the first appearance of shear failure should not be ignored. In Figure 9, when R_{wb} is equal to 0.4 and 0.5, the bending failure occurs before the shear failure, but on the contrary when R_{wb} is equal to 0.6~1.5, the shear failure occurs before the bending failure. From the point of view of structural ductility, when R_{wb} is equal to 0.4 and 0.5, shear ductility is better than bending ductility, but when R_{wb} is equal to 0.6~1.5, the opposite is true. Figure 10 indicates the ultimate displacements δ_u / δ_y of steel bridge pier frames, which combines the bending and shear cases. In Figure 11, all of computational results are given in the same figure. The solid and black mark means bending failure, and the hollow and white one means shear failure. For the cases with stiffened cross section, the bending failure is dominant. On the other hand, for the cases with unstiffened cross section, the shear failure plays a critical role when R_{wb} is from 0.6 to 1.5. The above findings indicate that we can make a judgment between bending and shear failure modes by the magnitude of R_{wb}, and the approximate boundary of R_{wb} is 0.6. Generally a pier frame may be designed to avoid the occurrence of shear failure. Therefore, its R_{wb} should be less than 0.6. In this study, for some stiffened cases, the stiffener plates make the shear failure risk decrease, and for the unstiffened cases, maybe the shear failure occurs firstly when R_{wb} is greater than 0.6. Consequently, the unstiffened cases should be verified and analyzed, and some stiffened measures for avoiding occurrence of shear failure should be taken into account. The discussions will be carried out deeply in following section 4.4.

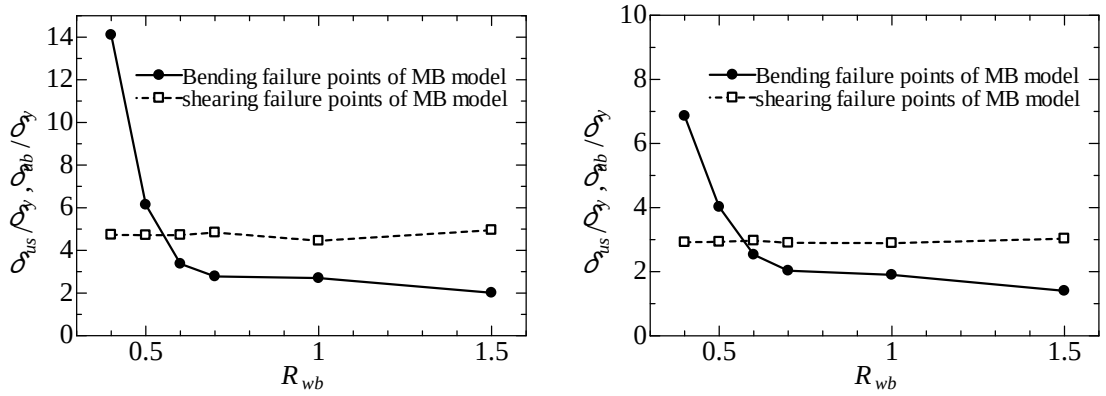

(a) US35-A Series (b) US45-A Series

Figure 9. Comparison between Bending and Shear Failure Points

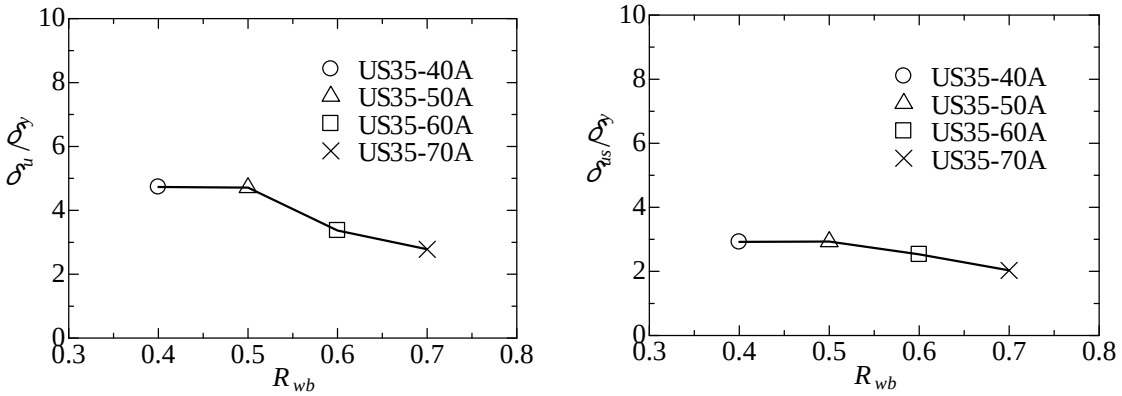

(a) US35-A Series (b) US45-A Series

Figure 10. Ductility Capacity Combining Bending and Shearing Cases

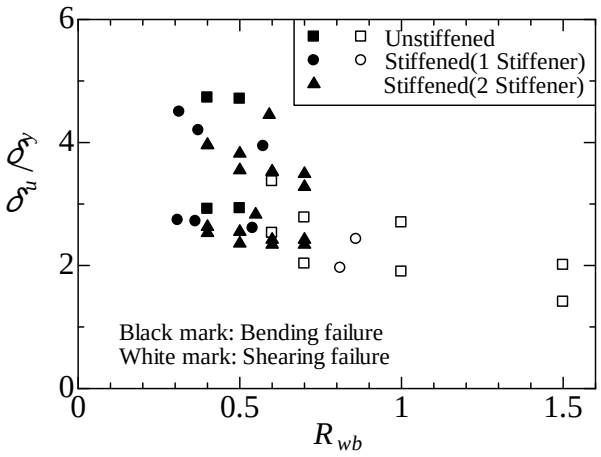

Figure 11. Relationship between Failure Modes (Bending and Shear Failure Modes) and Web Width-thickness Ratio of Beam R_{wb}

4.4 Performance of Steel Frames with and without Stiffeners

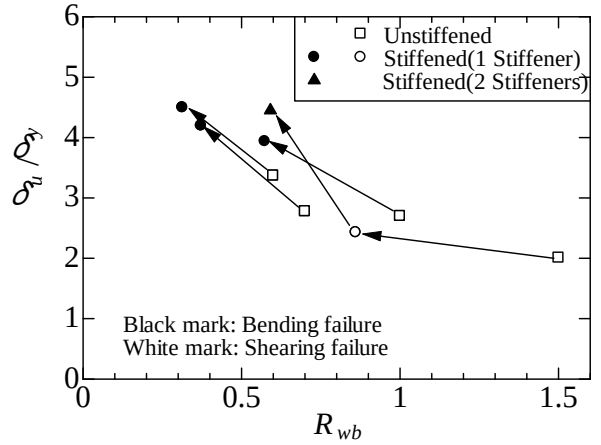

(a) R_f = 0.35

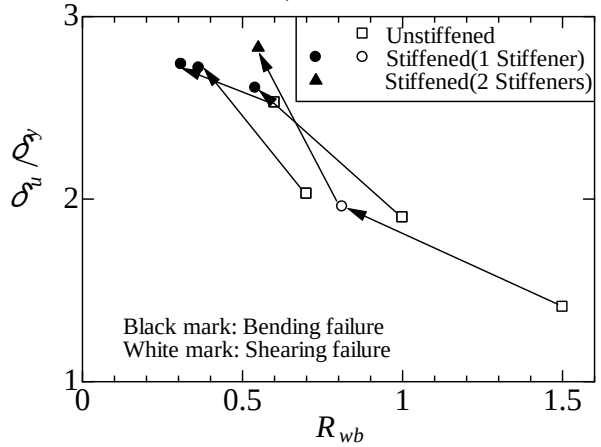

(b) R_f = 0.45

Figure 12. Effect of Stiffener Plate on Failure Modes

Ductility evaluation of US35-60A~150A and US45-60A~150A conducted above reveals that their shear failure is dominant, and some stiffener measures should be taken to avoid shear failure. In order to investigate the effect of stiffener measures on the failure mode for steel frames, the analytical cases with and without stiffeners are conducted. The ultimate displacements δ_u / δ_y versus web width-thickness ratio of beam R_{wb} curves are shown in Figure 12. The figure

illustrates how to improve ductility capacity, and how the failure mode translates from bending to shear failure by taking some stiffened measures. The flange width-thickness ratios R_f of column and beam are 0.35 and 0.45 in Figure 11(a) and Figure 12(b) (ductility capacity), respectively. The following demonstrates and explains these figures.

(1) When the flange width-thickness ratio R_f of column is 0.35 and 0.45, the failure mode changes from shear to bending failure at $R_{wb}=0.6$, for $R_{wb}=1.0,\ 0.7,\ 0.6$, respectively. This discussion dose not include the case of $R_{wb}=1.5$, which has the thinnest web plate. Although for some stiffened cases in above analyses, shear failure will appear firstly when $R_{wb}>0.8$, $R_{wb}=0.6$ is regarded as the boundary from shear failure to bending failure, as described above.

(2) When the flange width-thickness ratio R_f of column is 0.35, its ductility capacity is more better than the case of R_f=0.45. The main reason of this result is that bending failure is dominant if the flange width-thickness ratio is relatively small.

Next, for the cases with the thinnest web plate, every web plate has two stiffeners. The web width-thickness ratio of beam $R_{wb}=0.591$ (R_f =0.35) and $R_{wb}=0.549$ (R_f =0.45), respectively. These computational results are given in Figure 12. The model with two stiffeners has undergone bending failure. The ductility capacity has been improved greatly.

Different marks refer to different stiffened sections as shown in Figures. 11 and 12. From these results, shear failure is prone to occur when $R_{wb}>0.6$. For this reason, in this study, the magnitude 0.6 of web width-thickness ratio of beam is regarded as the key parameter of identifying different failure types.

5. SUMMARY AND CONCLUSIONS

In this paper, a more accurate analytical method considering the effect of shear failure at the mid-span of girder was proposed to investigate the ductility performance of steel bridge pier frames. Different two simulation models, namely BB and MB models, were employed to evaluate the ductility and failure behavior of steel bridge pier frames. In the proposed MB model, membrane and truss elements were introduced. Moreover, comparisons between MB and BB models' results were carried out and parameter effect investigation was conducted. From the above discussions, we can draw the following conclusions:

(1) Comparison between the previous BB model's and the proposed MB model's results has been conducted in this study. The deformation of MB model is larger than that of BB model. The traditional method using the BB model cannot accurately take shear failure at mid-span of girder into account. However, in some cases the effect of shear failure on ductility capacity of steel frames should not be ignored, especially for the cases with large web width-thickness ratio of beam.
(2) Because shear failure is one of the main failure modes of the cases with unstiffened web plate of beam, the finite element analysis using the MB model is necessary. Compared with the BB model, the MB model can accurately predict the shear failure of steel bridge pier frames. When the bending failure is dominant, the proposed analysis method in this paper shows acceptable agreement with the previous method.
(3) The stiffener of beam web plate can greatly improve ductility capability of structures.
(4) The magnitude of beam web width-thickness ratio (0.6) is the key parameter of identifying different failure types (bending and shear failure modes).

(5) The strength and ductility evaluation method of steel bridge pier frames can be effectively used to study the effects of various structural parameters which will be very useful in establishing design guidelines.

ACKNOWLEDGMENT

The first author is the post doctor researcher of Meijo University at Nagoya, Japan, who is supported by the Daiko Foundation. The author would like to thank to the Daiko Foundation for their financial assistance.

REFERENCES

[1] Nishikawa, K., Yamamoto, S., Natori, T., Terao, O., Yasunami, H., Terada, M., "An Experimental Study on Improvement of Seismic Performance of Existing Steel Bridge Piers", Journal of Structural Engineering, JSCE, 1996, Vol. 42, No. A, pp. 975-986 (in Japanese).

[2] White, D.W., Barth, K.E., "Strength and Ductility of Compact-flange I-girders in Negative Bending", Journal of Constructional Steel Research, 1998, Vol. 45, No. 3, pp. 241-280.

[3] Gao, S., Usami, T., Ge, H.B., "Ductility of Steel Short Cylinders in Compression and Bending", Journal of Engineering Mechanics, ASCE, 1998, Vol. 124, No. 2, pp. 176-183.

[4] Nishikawa, K., Murakoshi, J., Takahashi, M., Okamoto, T., Ikeda, S., Morishita, H., "Experimental Study on Strength and Ductility of Steel Portal Frame Pier", Journal of Structural Engineering, JSCE, 1999, Vol. 45, No. A, pp. 235-244 (in Japanese).

[5] Zheng, Y., Usami, T., Ge, H.B., "Ductility Evaluation Procedure for Thin-walled Steel Structures", Journal of Structural Engineering, ASCE, 2000, Vol. 126, No. 11, pp. 1312-1319.

[6] Susantha, K., Aoki, T., Kumano, T., Yamamoto, K., "Applicability of Low-yield-strength Steel for Ductility Improvement of Steel Bridge Piers", Engineering Structures, 2005, Vol. 27, No. 7, pp. 1064-1073.

[7] Hirano, T., Nishioka, T., Takada, Y., Yoshikawa, N., Matsuda, Y., "Report on Shear Strength of Web Panel in Cross Beam of Rigid Framed Steel Pier", Steel Construction Engineering, JSSC, 2006, Vol. 14, No. 11, pp. 527-534 (in Japanese).

[8] Miki, T., Yamada, O., Higuchi, N., "An Experimental Study on Elasto-plastic Behavior of Steel Web Plates under Cyclic Shearing Force", Journal of Structural Engineering, JSCE, 2007, Vol. 53, No. A, pp. 117-124 (in Japanese).

[9] Shen, Z., Zhang, Q., "Interaction of Local and Overall Instability of Compressed Box Columns", Journal of Structural Engineering, ASCE, 1991, Vol. 117, No. 11, pp. 3337-3355.

[10] Chan, S.L., Kitipornchai, S., Al-Bermani, F.G.A., "Elasto Plastic Analysis of Box Beam Columns Including Local Buckling Effects", Journal of Structural Engineering, ASCE, 1991, Vol. 117, No. 7, pp. 1946-1962.

[11] Fukumoto, Y., Uenoya, M., Nakamura, M., Kobayashi, Y., "Strength and Ductility of Plate Girder Panels under Cyclic Shear", Journal of Structural Engineering, JSCE, 2000, Vol. 46, No. 1, pp. 143-150 (in Japanese).

[12] Krawinkler, H., Popov, E.P., Bertero, V.V., "Shear Behavior of Steel Frame Joints", Journal of the Structural Division, ASCE, 1975, Vol. 101, No. 11, pp. 2317-2336.

[13] Ghobarah, A., Said, A., "Shear Strengthening of Beam-column Joints", Engineering Structures, 2002, Vol. 24, No. 7, pp. 881-888.

[14] Chen, Z.Y., Ge, H.B., Kasai, A., Usami, T., "Simplified Seismic Design Approach for Steel Portal Frame Piers with Hysteretic Dampers", Earthquake Engineering & Structural Dynamics, 2007, Vol. 36, No. 4, pp. 541-562.

[15] Nakamura, H., "Formulae for Evaluating Shear-bending Buckling Strength of Steel Piers with Circular Cross Section and Applicability of the Numerical Buckling Analysis Method", Proceedings of Nonlinear Numerical Analysis and Seismic Design of Steel Bridge Piers, Japan, 1997, Vol. 1, pp. 37-42 (in Japanese).
[16] Lee, S.C., "Strength of Plate Girder Web Panels under Pure Shear", Journal of Structural Engineering, ASCE, 1998, Vol. 124, No. 2, pp. 184-194.
[17] Morishita, N., Mori, H., Maeno, H., Okamoto, T., Nanoka, T., Usami, T., "Seismic Design of Steel Bridge Pier Frames Considering Shear Local Buckling in Beam Member", Proceedings of the 6th Symposium on Ductility Design Method for Bridges, Tokyo, 2003, Vol. 1, pp. 293-298 (in Japanese).
[18] Susantha, K.A.S., Aoki, T., Kumano, T., "Strength and Ductility Evaluation of Steel Bridge Piers with Linearly Tapered Plates", Journal of Constructional Steel Research, 2006, Vol. 62, No. 9, pp. 906-916.
[19] Zheng, Y., Usami, T., Ge, H.B., "Ductility of Thin-walled Steel Box Stub-columns", Journal of Structural Engineering, ASCE, 2000, Vol. 126, No. 11, pp. 1304-1311.
[20] Chusilp, P., Usami, T., "Strength and Ductility of Steel Box Girders under Cyclic Shear", Journal of Structural Engineering, ASCE, 2002, Vol. 128, No. 9, pp. 1130-1138.
[21] Chusilp, P., Usami, T., "New Elastic Stability Formulas for Multiple-stiffened Shear Panels", Journal of Structural Engineering, ASCE, 2002, Vol. 128, No. 6, pp. 833-836.
[22] ABAQUS, "ABAQUS/Analysis User's Manual-version 6.6", ABAQUS, Inc.: Pawtucket, RI, 2006.
[23] Usami, T., Zheng, Y., Ge, H.B., "Seismic Design Method for Thin-walled Steel Frame Structures", Journal of Structural Engineering, ASCE, 2001, Vol. 127, No. 2, pp. 137-144.
[24] JRA, "Specifications for Highway Bridges, Part V", Japanese Road Association, 1996 (in Japanese).
[25] Saiidi, M., Sozen, M.A., "Simple Nonlinear Seismic Analysis of R/C Structures", Journal of the Structural Division, ASCE, 1981, Vol. 107, No. 5, pp. 937-953.
[26] Collins, K.R., Wen, Y.K., Foutch, D.A., "Dual-level Sesmic Design: a Reliability-based Methodology", Earthquake Engineering & Structural Dynamics, 1996, Vol. 25, No. 12, pp. 1433-1467.
[27] Bracci, J.M., Kunnath, S.K., Reinhorn, A.M., "Seismic Performance and Retrofit Evaluation of Reinforced Concrete Structures", Journal of Structural Engineering, ASCE, 1999, Vol. 123, No. 1, pp. 3-10.
[28] Zheng, Y., Usami, T., Ge, H.B., "Seismic Response Predictions of Multi-span Steel Bridges through Pshover Aalysis", Earthquake Engineering & Structural Dynamics, 2003, Vol. 32, No. 8, pp. 1259-1274.
[29] Chusilp, P., Usami, T., Ge, H.B., Maeno, H., Aoki, T., "Cyclic Sear Bhaviour of Seel Bx Grders: Eperiment and Aalysis", Earthquake Engineering & Structural Dynamics, 2002, Vol. 31, No. 11, pp. 1993-2014.
[30] Gao, S., Usami, T., Ge, H.B., "Ductility Ealuation of Seel Bidge Pers with Ppe Sctions", Journal of Engineering Mechanics, ASCE, 1998, Vol. 124, No. 3, pp. 260-267.

RANDOM EQUIVALENT INITIAL BOW AND TILT IN STEEL FRAME

A. Machowski [1] and I. Tylek [2, *]

[1] *Assoc. Prof. D. Sc. Ph. D., Faculty of Civil Engineering, Cracow University of Technology, ul. Warszawska 24, 31-155 Cracow, Poland,*
[2] *Assist. Prof. Ph. D., Faculty of Civil Engineering, Cracow University of Technology, ul. Warszawska 24, 31-155 Cracow, Poland*
**(Corresponding author: E-mail: ik2@poczta.fm)*

Received: 3 September 2011; Revised: 26 September 2011; Accepted: 30 September 2011

ABSTRACT: Probabilistic models of equivalent geometrical imperfections suitable to analysis of steel buildings frames are under consideration. Statistically based models of equivalent imperfections, besides of application in structural reliability analysis, should be taken as basis of verification of equivalent imperfection formulas and rules of introducing imperfections into frame calculations proposed in different Standards. Column random equivalent initial bow was obtained in this paper utilizing randomization of buckling coefficient in well-known deterministic formula of equivalent initial bow. Problem of random equivalent initial tilt of frame was considered for spatial mechanical model of skeletal structure, braced by rigid floor disks, using results of existing buildings geodesic measurements statistical analysis. In the paper assessment of random initial tilts and initial bows joint effect is commented.

Keywords: Multistory steel frame, Random equivalent geometrical imperfection, Eurocode 3

1. INTRODUCTION

Carrying capacity of steel frames significantly depends on imperfections (Table 1(a)): single column; residual stresses and axes misalignments as well as bar system imperfections; column out-of-plumbs, eccentricity in column field joints, assembly stresses, random joint rigidity.

In traditional approach (Chen and Toma [1], Narayanan [2]) imperfections are modeled by linear combination of buckling modes (simplifying – only dominant buckling mode) which correspond to solution of bifurcation problem using linearized model of perfect system elastic stability. In this approach real structure imperfections are taking into consideration only indirectly – by using standard buckling curves. Column out-of-plumbs and other important imperfections, arising during assembly, are passed over in traditional approach.

Contemporary standard approach depends on taking into account of two equivalent geometrical imperfections (Table 1(b)): equivalent initial column bow e_0 (column misalignment and column residual stresses) and equivalent initial frame tilt ϕ_0 (column out-of-plumbs, eccentricity in column field joints, assembly stresses, randomness of beam-column joints rigidity).

Standard approach approximately takes into consideration steel skeleton fabrication conditions, in particular (Figure 1): columns division on assembly parts and its assembly with random out-of-plumbs – causing significant changes of moment values in equilibrium equations – because of large vertical forces occurrence.

Table 1. Conceptions of Equivalent Geometric Imperfections

(a) Imperfections of compressed bar and frame				
compressed bar		frame		
residual stresses	misalingment	column out-of-plumb	joints eccentricity	joints stiffness randomness
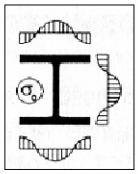		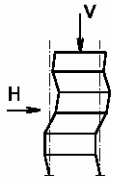	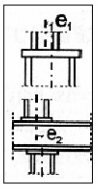	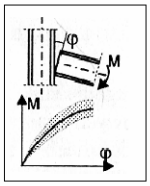
(b) Equivalent geometric imperfections				
compressed bar		frame		
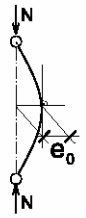	equivalent initial bow	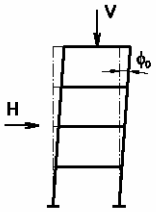	equivalent initial tilt (equivalent initial sway ratio)	

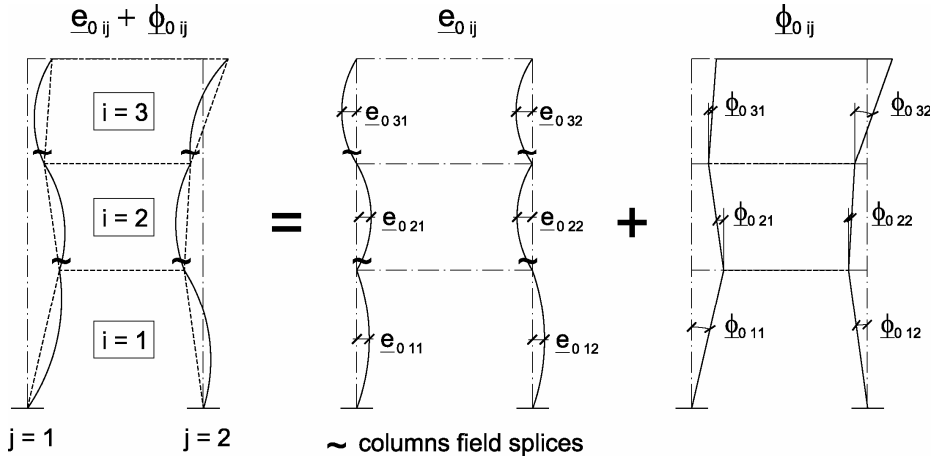

Figure 1. Columns Random Initial Bows and Initial Tilts

Issues connected with research and modeling of equivalent geometrical imperfections e_0 and ϕ_0 are discussed in chapters 2 to 4 of this paper.

2. RANDOM EQUIVALENT INITIAL BOW OF COLUMN

Random equivalent initial bow of column is obtained as function of random buckling coefficient $\underline{\varphi}$ (random values are underlined).

Random buckling coefficient was determined in papers (Machowski, A. [3]) utilizing Fukumoto and Itoh statistical data (Fukumoto, Y. and Itoh, Y. [4]) and applying randomization of axially compressed steel bar flexural buckling resistance standard formula

$$\underline{N}_{b.R} = \underline{\varphi} \cdot \underline{N}_{pl} \,. \tag{1}$$

It was assumed that random flexural buckling resistance of compressed steel bar $\underline{N}_{b.R}$ and bar cross-section random plastic resistance $\underline{N}_{pl}$ have logarithmic-normal distribution(*) – stable (invariant) with respect to multiplication and defined only for positive values of $\underline{N}_{b.R}$ and $\underline{N}_{pl}$.

It follows that stochastically independent (originally) from $\underline{N}_{pl}$ buckling coefficient $\underline{\varphi}$ has also logarithmic-normal distribution. Flexural buckling resistance $\underline{N}_{b.R}$ has median equal to product of medians $\breve{N}_{b.R} = \breve{\varphi} \cdot \breve{N}_{pl}$ and logarithmic coefficient of variation equal to vector sum of logarithmic coefficients of variation $\nu_{N\,b.R} = \sqrt{\nu_{\varphi}^2 + \nu_{N\,pl}^2}$.

Appropriate sets of data have been statistically processed with a mean-square approximation of experimental values of medians $\breve{\varphi}(\Lambda)$ and logarithmic coefficients of variation $\breve{\nu}_{\varphi}(\Lambda)$, where $\Lambda = \sqrt{\breve{N}_{pl} / \breve{N}_{E}}$ - relative slenderness ($\breve{N}_{E}$ - median of bar Euler's resistance) and application of formulas:

$$\breve{\varphi}(\Lambda) = (1 + \Lambda^{2n})^{-\frac{1}{n}}, \qquad \breve{\nu}_{\varphi}(\Lambda) = \nu_m \cdot \left(\frac{2 \cdot l \cdot \Lambda}{1 + (l \cdot \Lambda)^2} \right)^2 . \tag{2}$$

Empirical parameters (Machowski, A. [3]): n, ν_m, and l for buckling curves: "a", "b" and "c" (CEN [5], PKNMiJ [6]) are presented in Table 2.

Table 2. Empirical parameters for formula (2)

	Buckling curve		
	a	b	c
n	3,0	2,6	2,2
ν_m	0,10	0,11	0,13
l	0,8	0,9	1,0

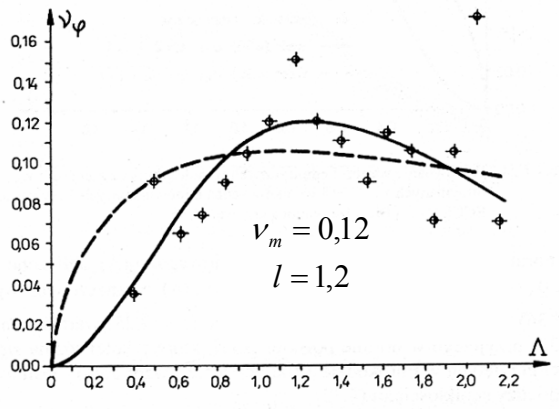

Figure 2. The Example of Values $\nu_{\varphi}(\Lambda)$ Approximation for N = 1251 Column Research Council Test Results (Machowski [3])

(*) parameters of logarithmic-normal variable $\underline{X} > 0$ with probability density function $f(x) = \frac{1}{\sqrt{2\pi} \cdot \nu_X \cdot X} \cdot \exp(-\ln^2(X / \breve{X}) / (2 \cdot \nu_X^2))$; mean value $\overline{X} = E\{X\}$ and coefficient of variation v_X are related as follows: $\breve{X} = \overline{X} / \sqrt{1 + \mathrm{v}_X^2}$, $\nu_X = \sqrt{\ln(1 + \mathrm{v}_X^2)}$.

An example of experimental coefficients of variation approximation by means of function $\nu_\varphi(\Lambda)$ according to Eq. 2 is shown in Figure 2; single points represent empirical mean values of $\nu_\varphi^*(\Lambda)$ connected with individual slenderness Λ. Form of function (2) refers to earlier proposals connected with stability coefficients (PKNMiJ [6], Allen [7], Rondal and Maquoi [8]).
For logarithmic-normal distribution parameters: $\breve{\varphi}$, ν_φ and design value φ_d of buckling coefficient $\underline{\varphi}$ are related as follows

$$\varphi_d \overset{df}{=} N_{b.Rd} / N_{pl,d} = \breve{N}_{b.R} \cdot \exp(-\beta_R \cdot \sqrt{\nu_\varphi^2 + \nu_R^2}) / (\breve{N}_{pl} \cdot \exp(-\beta_R \cdot \nu_R)) = \\ = \breve{\varphi} \cdot \exp(\beta_R \cdot (\nu_R - \sqrt{\nu_\varphi^2 + \nu_R^2})). \tag{3}$$

Introducing into Eq. 3 values according formula (2) and Table 2, $\nu_R = 0{,}10$ (according to (Murzewski [9])) for random plastic resistance of steel $\underline{R} \equiv \underline{f}$ ($\underline{R} = \underline{N}_{pl} / \underline{A}$) corrected for random deviation of bar cross-section area A and partial reliability index $\beta_R = 3{,}0$ relationship $\varphi_d(\Lambda)$ was received. This relationship was compared (for buckling curve "b") in Figure 3 with other curves characterizing buckling coefficient.

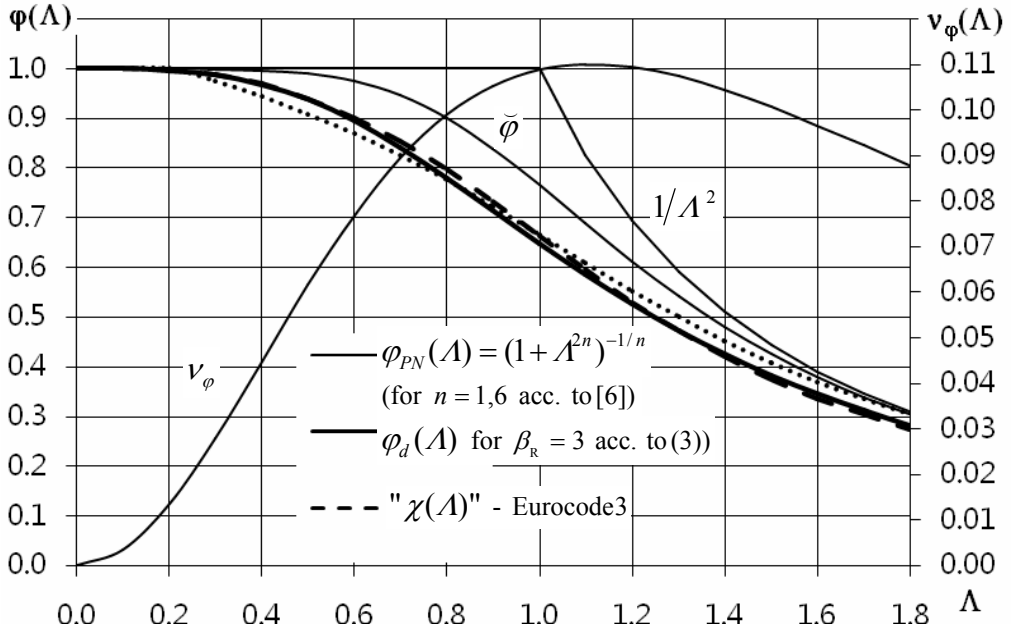

Figure 3. Parameters $\breve{\varphi}$ and ν_φ and Different Relationships $\varphi_d(\Lambda)$ for Buckling Curve "b"

Design values of φ_d obtained from Eq. 3 for $\beta_R = 3{,}0$ and parameters according to Table 2 are very close to standard values of $\varphi_{PN}(\Lambda)$ from Polish Standard [6] and values of $\chi(\Lambda)$ from Eurocode [5] (it was shown in Figure 3 – for buckling curve "b") if following relationship will be used

$$\Lambda = 1{,}1178 \cdot \bar{\lambda} \cong 1{,}12 \cdot \bar{\lambda} \,. \tag{4}$$

Relationship (4) may be obtained by assuming in general formula for relative slenderness

$$\lambda_r \overset{df}{=} \sqrt{N_{pl} / N_E} \cong \lambda / (\pi \cdot \sqrt{E / R_{pl}}) = \lambda / \lambda_1 , \tag{5}$$

medians: $E = \breve{E} = 205$ GPa and $R_{pl} = \breve{f} = 290$ MPa (hence $\lambda_1^{PN} = 84$) – as it was made in Polish Standard [6] for low-carbon steel or values: $E = 210$ GPa and $R_{pl} = f_y = 235$ MPa (hence $\lambda_1^{EC} = 93{,}9$) – according to Eurocode [5].

To determinate column random equivalent initial bow we use well-known formula of dimensionless equivalent initial deflection ε_0 (Rondal And Maquoi [8], ECCS [10]) of hinged bar with sinusoidal initial bow (the formula is based on bar resistance conservation criterion)

$$\varepsilon_{0e} = e_{0e} / r = (\varphi^{-1} - 1) \cdot (1 - \varphi \cdot \Lambda^2) = \varphi^{-1} + \varphi \cdot \Lambda^2 - (1 + \Lambda^2), \tag{6}$$

where: e_{0e} - bar equivalent initial bow,
$r \equiv W / A$ - radius of cross-section core.

Random imperfection $\underline{\varepsilon_{0e}} = \underline{e_{0e}} / r$ is obtained utilizing randomization of Eq. 6 by introducing in place of φ random bucking coefficient $\underline{\varphi}$ with logarithmic-normal distribution and parameters according to formulas (2) and Table 2. It follows that we have to determinate $\underline{\varepsilon}_{0e}$ probability distribution as a known deterministic function $\varepsilon_{0e}(\underline{\varphi})$ of the known random variable $\underline{\varphi}$.

According to mechanical interpretation and property of logarithmic-normal distribution quantity $\varepsilon_{0e} = e_{0e} / r$, similarly as other quantities in Eq. 6, are treated as non-negative (or positive) what follows that function $\varepsilon_{0e}(\varphi)$ is determined for $\varphi \in (0, \min(1, 1/\Lambda^2)]$. In this range of φ values function $\varepsilon_{0e}(\varphi)$ is monotonically decreasing (Figure 4(a)) and probability density function $g(\varepsilon_{0e})$ amounts to transformation type (Papoulis [11]):

$$g(y) = f(u^{-1}(y)) \cdot \left| \frac{du^{-1}(y)}{dy} \right| \tag{7}$$

where: $f(x)$ - known probability density function of random variable $\underline{x}$,
$u^{-1}(y_x)$ - inverse function of given function $y = u(x)$ - strictly monotonic,
$g(y)$ - inquired probability density function of random variable $\underline{y} = u(\underline{x})$.

Logarithmic-normal distribution, rational in case of coefficient φ (definite for $\varphi > 0$ and stable in relation to multiplication) does not fulfil yet condition $\varphi \le \varphi_{\max} = \min(1, 1/\Lambda^2)$. To calculate density function $g(\varepsilon_{0e})$ we introduce corrected (cut off) distribution $\underline{\varphi}$ with density $c \cdot f(\varphi)$, where: $c = 1/(1 - \omega_m)$ - normalizing factor, $\omega_m = \text{Prob.}\{\varphi \ge \varphi_{\max}\}$ (Figure 4(a)). This adoption we propose for skeleton column slenderness $\Lambda \le\sim 1{,}4$ (that is $\lambda <\sim 120$). For slenderness values distant from 1 coefficient c increases significantly.

After introducing into Eq. 7 function $\varepsilon_{0e}(\varphi; \Lambda)$ and corrected logarithmic-normal probability density function $f(\varphi; \Lambda)$ with parameters $\varphi(\Lambda)$ and $\nu_\varphi(\Lambda)$ we obtain density function of random variable $\underline{\varepsilon}_{0e}$ in the form of:

$$g(\varepsilon_{0e};\Lambda)=\frac{c}{\sqrt{2\pi}\cdot\nu_{\varphi}\cdot\varphi(\varepsilon_{0e})}\cdot\exp\left\{-\frac{\ln^2(\varphi(\varepsilon_{0e})/\breve{\varphi})}{2\cdot\nu_{\varphi}^2}\right\}\cdot\left|\frac{\mathrm{d}\varphi(\varepsilon_{0e})}{\mathrm{d}\varepsilon_{0e}}\right|, \tag{8}$$

where: $\varphi(\varepsilon_{0e})=(a-b)/(2\cdot\Lambda^2)$, $\mathrm{d}\varphi/\mathrm{d}\varepsilon_{0e}=(1-a/b)/(2\cdot\Lambda^2)$, $a=a(\varepsilon_{0e};\Lambda)=\varepsilon_{0e}+\Lambda^2+1$,
$b=b(\varepsilon_{0e};\Lambda)=\varepsilon_{0e}^2+2\cdot\varepsilon_{0e}\cdot(1+\Lambda^2)+(1-\Lambda^2)^2$.

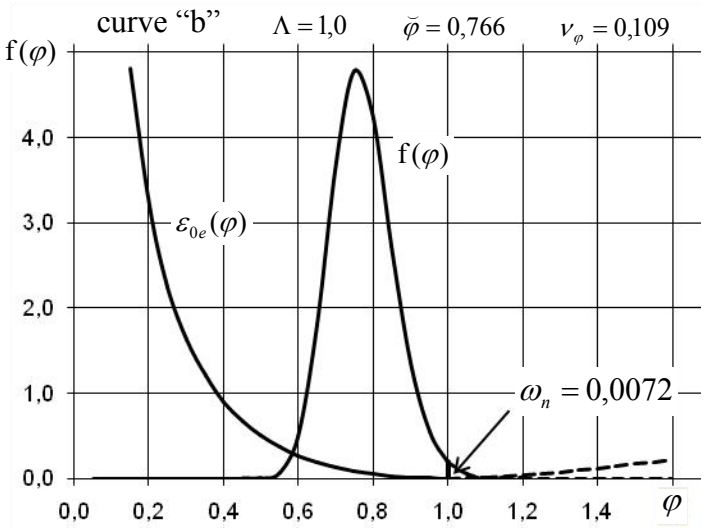

Figure 4(a). The Example of $\varepsilon_{0e}(\varphi)$ and $f(\varphi)$ Relationship

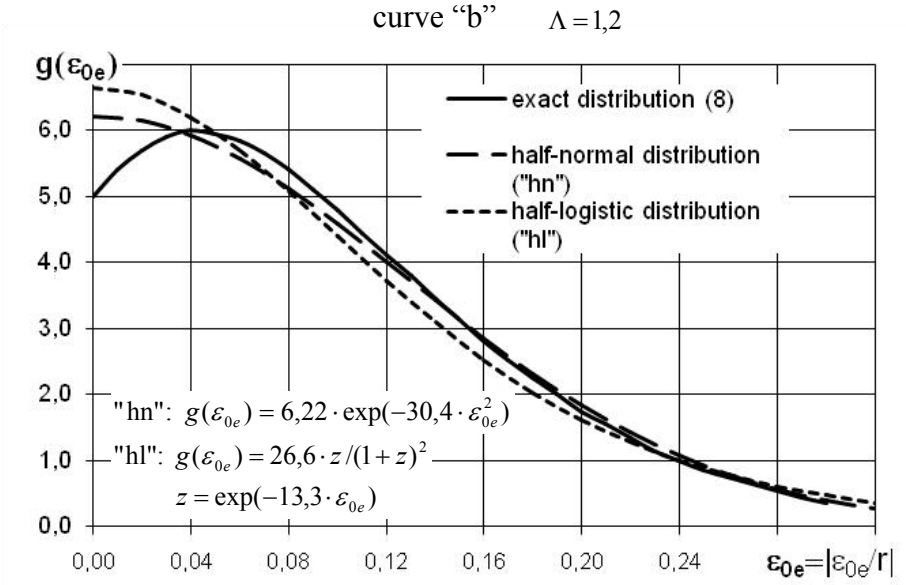

Figure 4(b). The Example of Probability Density Function $g(\varepsilon_{0e})$

Example results of calculation according to Eq. 8, for bucking curve "b" and $\Lambda=1{,}2$, were shown in Figure 4(b). Density of "exact" distribution ("8") according to Eq. 8 shows (beside of close surroundings of $\varepsilon_{0e}=0$ point) very good compatibility with density of half-normal distribution ("hn") and good compatibility with density of half-logistic distribution ("hl"). One-parameter half distributions mentioned above were matched according to mean values conformity criterion: $\overline{X}_e=\overline{X}_{hn}=\overline{X}_{hl}$ (where $\overline{X}\equiv\overline{\varepsilon}_{0e}$).

Mean values $\bar{\varepsilon}_{0e}$ and standard deviations $\mu_{\varepsilon 0e}$, determined from numerical integration of Eq. 8, for appropriate half-normal distributions $\underline{\varepsilon}_{0e}$, are related to Λ almost linearly (Figure 5(a))

$$\bar{\varepsilon}_{0e} = C_{\bar{\varepsilon}} \cdot \Lambda, \qquad \mu_{\varepsilon 0e} = C_{\mu\varepsilon} \cdot \Lambda, \tag{9}$$

with direction coefficients $C_{\bar{\varepsilon}}$ and $C_{\mu\varepsilon}$ given in Table 3.

Value of coefficient $C^*_{\mu\varepsilon}$ (for relationship $\mu^*_{\varepsilon 0e} = C^*_{\mu\varepsilon} \cdot \Lambda$) corresponding to normal distribution $\underline{\varepsilon}^*_{0e}$ with changeable signs and mean value $\bar{\varepsilon}^*_{0e} = 0$ is obtained (Table 3) from relationship $C^*_{\mu\varepsilon} = C_{\mu\varepsilon} / \sqrt{1 - 2/\pi}$ (Machowski [3]).

In Figure 5(b) values of $\varepsilon_{0e}(\Lambda)$, obtained from half-normal distribution ε_{0e} with parameters according to Table 3, were compared, for bucking curve "b", with values from Standard Recommendations and values from formula (6). Straight lines "1" and "2" are obtained for assumed probability ω of exceeding ε_{0e} value (top quantiles) in half-normal distribution. Straight line "2" corresponding to value $\omega = 2\%$ turns out very close to straight line "3" characterized by equation $\varepsilon_{0z} = 0{,}3 \cdot \lambda / 100 = 0{,}3 \cdot \Lambda \cdot \lambda_1 / 100$ (for $\lambda_1 = 0{,}84$) – representing traditional British Recommendations (BS 449). Broken line "4", according to Eurocode 3 – with equation: $\varepsilon_{0z} = 0{,}34 \cdot (\bar{\lambda} - 0{,}2)$ - for $\bar{\lambda} > 0{,}2$ and $\varepsilon_{0z} = 0$ - for $\bar{\lambda} \le 0{,}2$, (taking relationship $\Lambda = 1{,}12 \cdot \bar{\lambda}$ into consideration) shows good compatibility with curve "5" obtained from (6) substituting $\chi(\bar{\lambda})$ in place of $\varphi(\lambda)$ and $\bar{\lambda}$ in place of Λ.

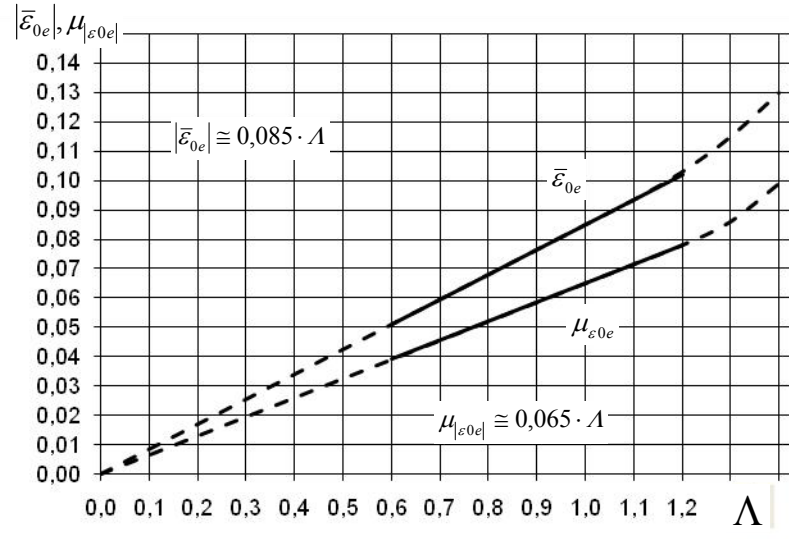

Figure 5(a). Examples of Relation $\bar{\varepsilon}_{0e}(\Lambda)$ and $\mu_{\varepsilon 0e}(\Lambda)$ for Curve "b"

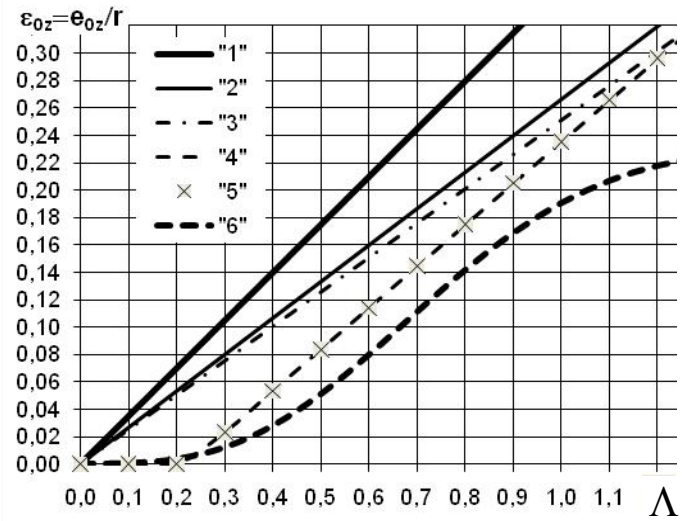

Figure 5(b). Comparison of relation $\varepsilon_{0e}(\Lambda)$ according to different formulas ("1" – random for ω = 1,35‰, "2" – random for ω = 2%, "3" – "0,3λ/100", "4" – "$0{,}34(\bar{\lambda} - 0{,}2)$", "5" – acc. to Eq. 6 for $\bar{\lambda}$ and $\chi(\bar{\lambda})$, "6" – acc. to Eq. 6 for Λ and $\varphi(\Lambda)$

Table 3. Coefficients values for formula (9)

buckling curve	$C_{\bar{\varepsilon}}$	$C_{\mu\varepsilon}$	$C^{*}_{\mu\varepsilon}$
a	0,065	0,045	0,075
b	0,085	0,065	0,110
c	0,120	0,085	0,140

Occurrence of φ and Λ quantities in non-linear form in Eq. (6) cause significant mutual discrepancy between curves "5" and "6" (Figure 5(b)) despite of affirmed earlier good compatibility of buckling curves (Figure 3).

3. RANDOM EQUIVALENT INITIAL TILT OF FRAME

Mathematical model of column single story initial tilt was determined on the basis of column out-of-plumbs post-fabrication measurements, carried out after all frames erection and after construction of all floors.

Most extensive statistical analysis of measurements mentioned above was conducted in (Machowski [3, 12]) which also includes results obtained earlier by Beaulieu (Beaulieu and Adams [13]) and Lindner (Lindner and Gietzelt [14]).

Conducted analysis showed that that mathematical model of stationary gaussian random noise $\underline{\phi}^{x}_{ijk}$ and $\underline{\phi}^{y}_{ijk}$ (stationary random series with mean value $\bar{\phi} = 0$ and constant variance $D_{\phi} = \mu^{2}_{\phi} = \text{const.}$) is justified if empirical variance fulfils a constraint

$$\mu^{2}_{\phi} \le 3\,(‰)^{2}, \tag{10}$$

what agrees with keeping initial tilt standard tolerance.

The second conclusion was that only exist weak autocorrelation dependence between tilts of columns in the same vertical planar frames and lack of correlation between any other initial tilts.

For design purposes it is very convenient to assume one random value of equivalent initial tilt for frame as a whole $\underline{\phi}^{EFF}$ instead of column initial tilts random sequences $\underline{\phi}_{ip}$.

Post-fabrication column out-of-plumbs cause additional bending moments from vertical load for frame as vertical cantilever (Machowski, A. [3, 12]).

For bar-disk analytical scheme of multistory skeletal structure with rigid floor-disks effective initial random tilt for *i*-th story of building $\underline{\phi}_i^{eff}$ may follow from conservation of global moment increment condition (if torsional effect for building as vertical cantilever is neglected)

$$\Delta \underline{\mathrm{M}}_{\mathrm{i}}^{\phi} = \sum_{\mathrm{p}=1}^{\mathrm{s}} \mathrm{P}_{\mathrm{ip}} \cdot \mathrm{h}_{\mathrm{i}} \cdot \underline{\phi}_{\mathrm{ip}} = \mathrm{P}_{\mathrm{i}} \cdot \mathrm{h}_{\mathrm{i}} \cdot \underline{\phi}_{\mathrm{i}}^{\mathrm{eff}}, \tag{11}$$

where: $P_i = \Sigma P_{ip}$, ($p = 1 \ldots s.$) - sum of all vertical loads acting on building above *i*-th story,
P_{ip} (for *s* columns $i = 1, 2, \ldots, s.$ on *i*-th story of building) – sum of vertical loads above *i*-th story in *p*-th column,

hence *i*-th story equivalent initial tilt

$$\underline{\phi}_i^{eff} = \sum_{p=1}^{s} w_{ip} \cdot \underline{\phi}_{ip} = \mathbf{w}_i \, \boldsymbol{\phi}_i^{\mathrm{T}}, \tag{12}$$

Story random initial tilt $\underline{\phi}_i^{eff}$ is normal random variable with parameters (Machowski [3, 12]):

$$\mathrm{E}\left\{\underline{\phi}_i^{eff}\right\} = 0, \quad \mu_{\phi \mathrm{i}}^2 = k_{c,i}^2 \cdot \mu_{\phi}^2, \tag{13}$$

where

$$k_{c,i}^2 = \mathbf{w}_i \boldsymbol{\rho}_s \mathbf{w}_i^{\mathrm{T}} = \sum_{p=1}^{s} w_{ip} \cdot \sum_{q=1}^{s} w_{iq} \cdot \rho_{pq} \tag{14}$$

is positively defined quadratic form of *s*-variables: $w_{i1}, \ldots, w_{ip}, \ldots w_{is}$. with symmetric matrix of coefficients $\boldsymbol{\rho}_s$ equal to normalized correlation matrix $\boldsymbol{\rho}_s$ of random vector $\underline{\boldsymbol{\phi}}_i$.

Values of reduction coefficient $k_{c,i}$ according to Eq. 14 have been analysed in detail in (Machowski [3, 12]). Conducted analysis showed that among standard formulas closest to obtained result is that in Polish Standard [6], on condition that only columns with vertical load (above *i*-th story) arrangement parameter $c \geq 0{,}5$ are taken into account.

Safe approximation of effective random initial tilt for frame as a whole may be defined as follows

$$\underline{\phi}^{EFF} = \max_{i=1}^{n} \left| \underline{\phi}_i^{EFF} \right| = \max_{i=1}^{n} \left| \sum_{t=i}^{n} V_t \cdot \sum_{q=i}^{t} h_q \cdot \underline{\phi}_q^{eff} \cdot \left(\sum_{t=i}^{n} V_t \cdot \sum_{q=i}^{t} h_q \right)^{-1} \right|, \tag{15}$$

$\underline{\phi}_i^{EFF}$ – effective random initial tilt for frame as a whole, which guarantee safe estimation of additional bending moment for *i*-th story of frame as vertical cantilever,

$\underline{\phi}_i^{eff}$ – according to Eq. 12,

V_t – sum of vertical loads imposed immediately to *t*-th story.

Analyses conducted in (Machowski [3, 12]) showed that within confines of discussed conception reduction of initial tilt standard deviation and characteristic value depending on story number is unfounded. According to extensive analyses presented in (Rondal and Maquoi [8], Machowski and Tylek [15]) this reduction is justified only in special cases, e.g. with reference to frames fulfilled "strong columns" condition (columns remain elastic up to plastic mechanism formation).

4. JOINT EFFECT OF EQUIVALENT INITIAL TILT AND INITIAL BOW

Statistically based models of equivalent imperfections $\underline{e}_{0e}$ and $\underline{\phi}_{0e}$, according to chapters 2 and 3, first of all may be used to verify Standard conceptions of steel skeletons calculation. This verification may apply, among others things, to often criticized effective length conception for sway frames and described in p. 6.3.4 Eurocode 3 [5] so called "general method" depending on reduction of resistance coefficient $\alpha_{ult,k}$ by means of factor χ_{op} determined as Standard flexural buckling coefficient χ or Standard lateral-torsional buckling coefficient χ_{LT} - calculated for "global non-dimensional slenderness" $\overline{\lambda}_{op}$, connected with out-of-plane buckling of a structural component. Analysis of Standard conceptions mentioned above with application of proposed models of $\underline{e}_{0e}$ and $\underline{\phi}_{0e}$ would require, as it seems, separate extensive study.

Another important problem that will be consider farther in this article, is influence of both random equivalent imperfections on total imperfections effect. In this case random variability of $\underline{e}_{0e}$ sign (direction) in column assembly elements may be important. Taking into account of this last effect requires, even in the simplest cases, to consider examples of multistory steel frames.

Joint effect of random equivalent initial tilt $\underline{\phi}_{0e}$ and random equivalent initial bow $\underline{e}_{0e}$ in "advanced analysis" was considered on the example of 5-story steel skeleton (Figure 6). Vertical loads from floors, roof and walls of the building are carried by floor beams on five transversal rigid frames located in axes 1-1 to 5-5 of building horizontal projection. Skeleton bracing system, carrying horizontal load, is made up, among transversal frames mentioned above, three equal two-bay rigid frames located in axes: A-A, B-B and C-C (see horizontal projection in Figure 6). Skeleton filling consist of floors and flat roof with reinforced concrete supporting structure, (rigid in own plane and nonflexibly connected with beams) and light-weight partition and curtain walls. It should be noticed that plane of every longitudinal frame agrees with column minor stiffness plane (Figures 6 and 7).

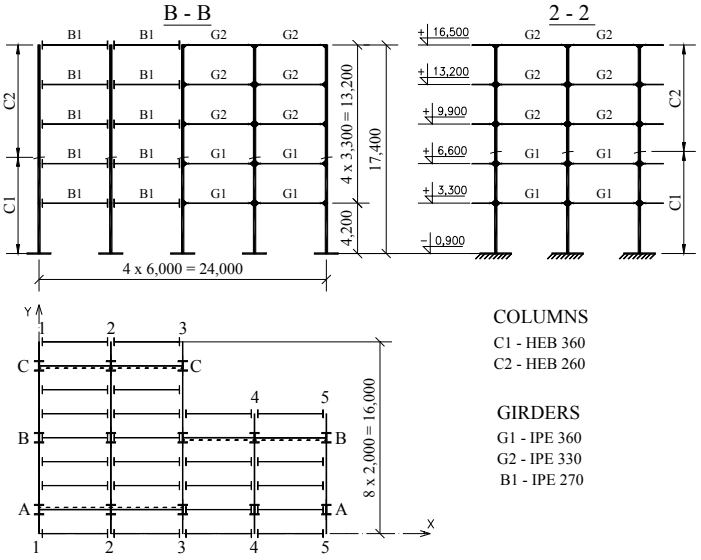

Figure 6. Analysed Skeletal Framed Steel Structure

Considering vertical planar frame of longitudinal bracing system (e.g. C-C) acc. to Figure 6 and neglecting torsional effects for building as vertical cantilever substitute static system of planar frame (Figure 7) was assumed. This system was loaded by realistic vertical loads in the form of concentrated forces Q_{11}^{C} to Q_{n3}^{C} – putted in nodes and fictitious imperfectional load uniformly distributed on columns: q_{11} ... q_{n3} (as in [5]) – balanced by reactions R_{11} ... R_{n3}.

Influence of column initial tilts of skeleton braced in longitudinal direction by three identical frames, joined by rigid floor disks, was taken into consideration by adding to planar frame fictitious system (Figure 7) consisted of bars ideally rigid, connected by hinges with each other and with frame. To the nodes of system mentioned above following loads were applied: vertical loads V_1 ... V_i ... V_n equal to 1/3 of sum of Q_i vertical loads on i-th skeleton floor and couples of forces $P_i\phi_{0i}$ (i = 1, 2, ..., n.) representing equivalent imperfectional load from initial tilts.

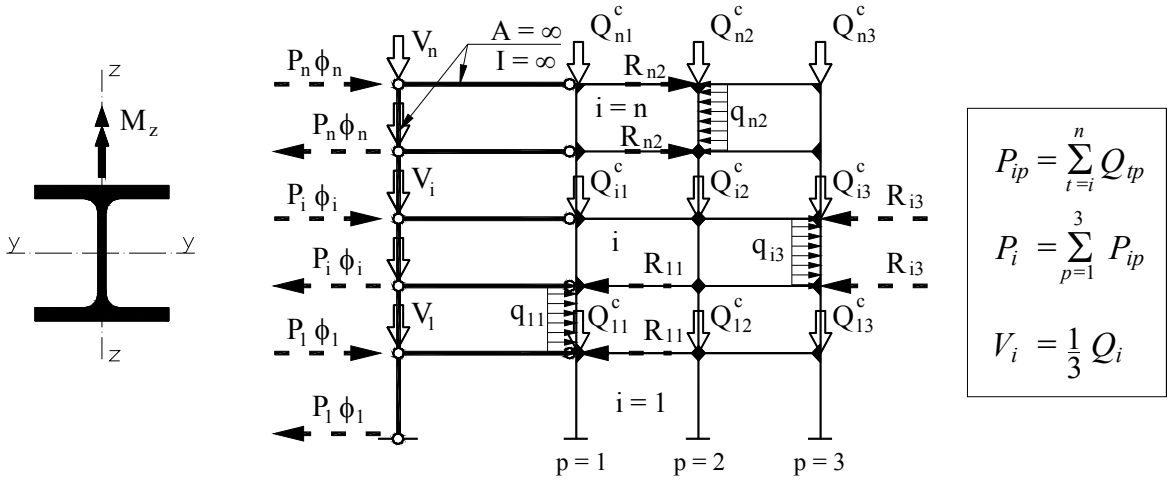

Figure 7. Substitute Static System of Analyzed Planar Bracing System of 5-story Skeletal Steel Structure (Q_{ip} – Total Vertical Load of Building as a Whole i-th story)

Random sequences of story initial tilts were computer generated in the form of vector $\underline{\boldsymbol{\phi}}^{eff} = \{\underline{\phi}_i^{eff}\}$ which elements were normal variable with parameters according to Eq. 13. Week correlation between initial tilts in vertical sequences was neglected.

Mathematical model of column random equivalent initial bow was product of random initial bow and random binary sequence (with elements 1 and -1). Value of column random initial bow was determined on the basis of knowledge of probability density function and characteristics of random dimensionless column bow distribution (according to p.2). Normal distribution with parameters $\{\bar{\varepsilon}_{0e}^{*} = 0,\ \mu_{\varepsilon 0e}^{*} = C_{\mu\varepsilon}^{*} \cdot \Lambda\}$ ($C_{\mu\varepsilon}^{*}$ according to Table 3) was assumed. It was also assumed that column splices are located on every story (above bottom node of column) so there is no correlation between initial bows of individual columns.

Additional effect of column equivalent initial bows on frame carrying capacity (associated with limit point on frame equilibrium path) was determined by comparison of frame initial tilt $\underline{\phi}^{EFF}(\underline{\phi}_{0e})$ (substitutes for random sequence of story initial tilts only – Figure 8a) standard deviation with frame initial tilt $\underline{\phi}^{EFF}(\underline{\phi}_{0e}, \underline{e}_{0e})$ (substitutes for story random initial tilts and column random initial bows – Figure 8b) standard deviation values. In both cases the same sequences of story random initial tilts were considered.

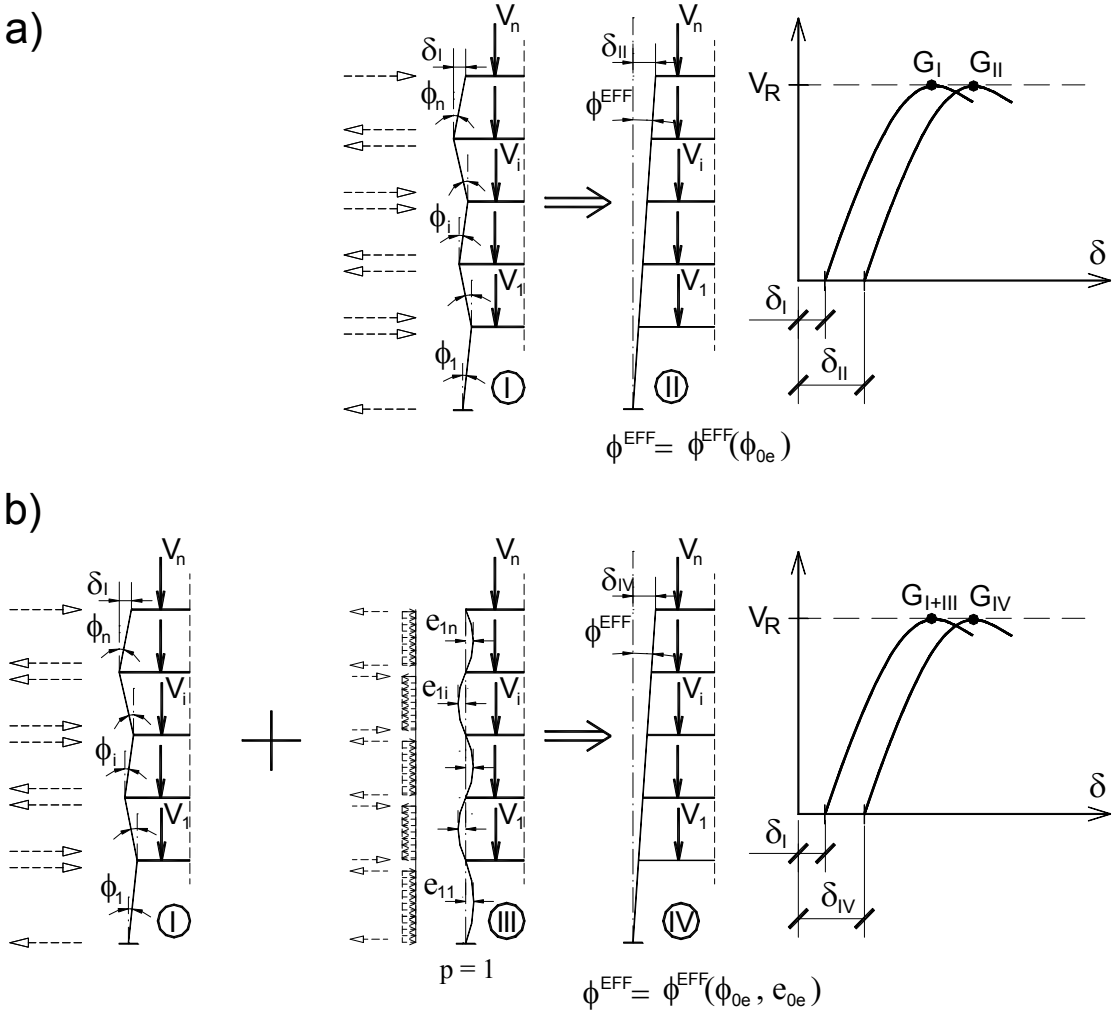

Figure 8. Random Sequence of Story Initial Tilts, Random Set of Column p = 1 Initial Bows and Its Equivalent Forces; Equivalent Tilts of Frame as a Whole and Corresponding Paths of Equilibrium

According to applied simulation procedure, for every realization of equivalent imperfectional loads set (Figure 7) respective frame equilibrium path and frame carrying capacity were determined. Next the effective initial tilt of frame as a whole $\underline{\phi}^{EFF}$ was chosen in agreement with condition of frame limit carrying capacity conservation (Figure 8). Equivalent random initial tilt of plane frame as a whole $\underline{\phi}^{EFF}$ was determined on the basis of conservation of carrying capacity associated with limit point on frame equilibrium path criterion. Calculations were conducted for 700 elements population.

In order to obtain frame equilibrium path and frame limit carrying capacities computer program ANSYS, based Finite Element Method, were utilized. Two-dimensional bar structure model with regular mesh and elastic-plastic (bilinear) model of material was assumed. Description of the material model was based on Huber-Mises-Hencky plasticity criterion, associative flow rule and rule of kinematic hardening. Development of plastic zones (in cross section and along length of element) and large displacements (translations and rotations) with small deflections were take into consideration.

Difference between standard deviations of frame initial tilt $\underline{\phi}^{EFF}(\underline{\phi}_{0e})$ and frame initial tilt $\underline{\phi}^{EFF}(\underline{\phi}_{0e},\underline{e}_{0e})$ obtained from conducted analysis is lower than 2% and indicates that additional influence of column random equivalent initial bows on frame carrying capacity in advanced analysis may be neglected.

Results of earlier works (De Luca and Mele [17]) indicated that interaction of global (tilts) and local (bows) geometric imperfections causes reduction of frame carrying capacity by 10%, but authors [17] assumed deterministic (instead of random) values of equivalent imperfections and selected some combinations of global and local equivalent geometric imperfections, compatible with first buckling eigenvector of ideal elastic frame and combinations of initial bows acceptable for the sake of columns splices (Figure 9).

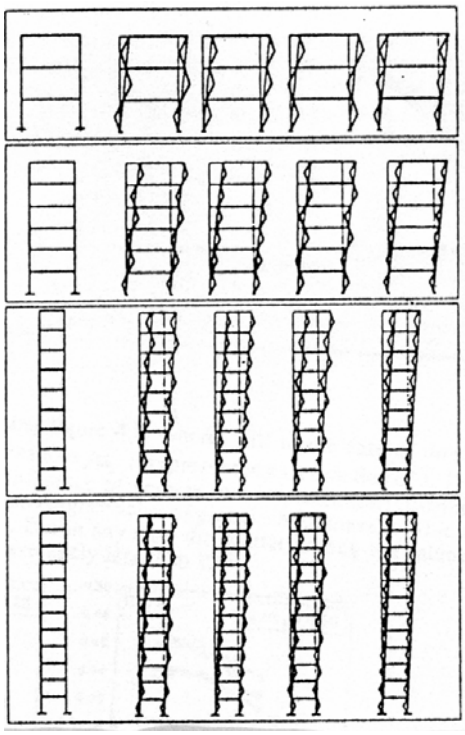

Figure 9. Set of Local and Global Geometrical Imperfections Combination Analyzed in [17]

5. CONCLUSIONS

Verification of Standard recommendations of steel skeletons design with equivalent geometrical imperfections (column initial tilt ϕ_0 and bow e_0) should base on probabilistic models of these imperfections and takes into account its interaction. Application of random models and imperfections acting together should lead to taking into consideration of favourable effects – similar to these which we deal with in case of random load combinations.

Possibility of applying approach mentioned above offers this work model of equivalent random initial bow of compressed bar $\underline{e}_0$. It is obtained out of randomization of buckling coefficient in well-known deterministic formula of equivalent initial bow. This model together with known from earlier works, e.g. authors' works [3, 12, 15, 16], model of equivalent random initial tilt $\underline{\phi}_0$, allows analyses of mentioned above Standard reccomendations.

In the paper effects of column initial tilts and initial bows interaction were investigated using probabilistic approach, introducing into calculations, in elastic-plastic structure behaviour, statistically based models of equivalent imperfections.

Analysis of 2-bay 5-story frame planar bracing system with random sequences of story initial tilts and random sets of column initial bows showed slight influence of column random initial bows on frame carrying capacity and equivalent initial tilt of frame as a whole $\underline{\phi}^{EFF}$. Influence of interaction of global and local imperfections on frame carrying capacity was lower than 2%.

Results of conducted analysis justify passing over of local geometric imperfections influence in planar frames advanced analysis. It also shows that Eurocode 3 procedure of steel frame design, recommending to introduce in stage on static calculations only frame equivalent initial tilt while influence of column equivalent initial bows is taking into account in beam-column design formulas.

ACKNOWLEDGEMENT

Scientific research has been carried out as a part of the Project "Innovative resources and effective methods of safety improvement and durability of buildings and transport infrastructure in the sustainable development" financed by European Union from the European Fund of Regional Development based on the Operational Program of the Innovative Economy.

REFERENCES

[1] Chen, W.F. and Toma, S., "Advanced Analysis of Steel Frames", London-Tokyo: CRC Press, 1994.
[2] Narayanan, R. ed, "Steel Framed Structures, Stability and Strength", Elsevier Science, 1985.
[3] Machowski, A., "Problems of Limit States and Reliability of Steel Multistory Building Frames", Monograph No. 262, Cracow University of Technology, 1999 [in Polish].
[4] Fukumoto, Y. and Itoh, Y., "Multiple Buckling Curves Based on Experimental Data", Construction Metállique, 1984, Vol. 3 [in French].
[5] CEN "EN 1993-1-1. Eurocode 3, Design of Steel Structures, Part 1.1: General Rules and Rules for Buildings".
[6] PKNMiJ, "PN-90/B-03200, Steel Structures, Design Rules" [in Polish].

[7] Allen, D., “Merchant-Rankine Approach to Member Stability”, Journal of the Structural Division, 1978, 104 (ST.12), pp. 1909-1914.
[8] Rondal, J. and Maquoi, R., “The Ayrton-Perry Formulation for Buckling of Metallic Bars”, Construction Metállique, 1979, 4, pp. 41-53 [in French].
[9] Murzewski, J., “Design of Steel Structures for Differentiated Reliability Levels”, Archives of Civil Engineering, 2008, LIV(1), pp. 209-237.
[10] ECCS, “European Specifications for Steel Structures”, 1-st ed; 1974.
[11] Papoulis, A., “Probability, Random Variables and Stochastic Processes”, McGraw-Hill Inc, 1965.
[12] Machowski, A., “Initial Random Out-of-plumbs of Steel Frame Columns”, Archives of Civil Engineering, 2002, XLVIII(2), pp. 207-226.
[13] Beaulieu, D. and Adams, P.F., “The Results of a Survey on Structural Out-of-plumbs”, Canadian Journal of Civil Engineering, 1978, Vol. 5, pp. 642-470.
[14] Lindner, J. and Gietzelt, R., “Evaluation of Imperfections of Support – Elements”, Stahlbau, 1984, Vol. 4, pp. 97-98 [in German].
[15] Machowski, A. and Tylek, I., “Conceptions of Equivalent Imperfections in Analysis of Steel Frames”, The International Journal of Advanced Steel Construction, 2008, Vol. 4, No. 1, pp. 13-25.
[16] Tylek, I., “Equivalent Geometrical Imperfections of Multistory Steel Building Frames”, Doctoral Thesis, Cracow University of Technology, 2007 [in Polish].
[17] De Luca A. and Mele, E., “Analysis of Steel Frames in the Light of Eurocode 3 and New Research Results”, In: White, D.W. and Chen, W.F. ed., “Plastic Hinge Based Methods for Advanced Analysis and Design of Steel Frames”, SSRC, Lehigh Univ., 1993, pp. 97-152.

THE EFFECTS OF FRAME DEFORMATION ON WELDED GUSSET PLATES FOR DIAGONAL BRACING ELEMENTS LOADED IN TENSION

J. Kent Hsiao[1,*], Donald W. Tempinson[2] and Jianming Li[3]

[1]*Associate Professor, Department of Civil and Environmental Engineering, Southern Illinois University Carbondale, Carbondale, IL, USA*
[2]*Former Graduate Student, Department of Civil and Environmental Engineering, Southern Illinois University Carbondale, Carbondale, IL, USA*
[3]*Graduate Student, Department of Civil and Environmental Engineering, Southern Illinois University Carbondale, Carbondale, IL, USA*
**(Corresponding author: E-mail: hsiao@engr.siu.edu)*

Received: 10 February 2012; Revised: 17 April 2012; Accepted: 27 April 2012

ABSTRACT: The effects of frame deformation on a gusset plate in a braced frame can be defined as the increases in stress in the gusset plate caused by the deformations of the beams and the columns of the braced frame. The hand-calculated approach for the design of gusset plates for diagonal bracing elements loaded in tension has traditionally neglected the frame deformation effects. A design example for a brace-beam-column gusset plate connection using the traditional hand-calculated approach is given in this paper. Two finite element approaches (one neglects the effects of frame deformation on the gusset plate while the other one considers the effects) are used to investigate the adequacy of the gusset plate designed by the hand-calculated approach. This study concludes that frame deformation effects have caused the increases in the von Mises and the first-principal stresses located at the Whitmore section of the gusset plate, as well as the increase in the combined effects of the factored tension and shear forces at the gusset edges. The traditional hand-calculated approach which neglects the frame deformation effects, therefore, may result in an under-design of the gusset plate.

Keywords: Finite element method, Nonlinear analysis, Rigid frames, Stress concentration, Tensile strength, Welded connections, Yield stress

1. INTRODUCTION

Gusset plates are used to transmit the applied forces from main elements (beams and columns) to bracing elements and vice versa. Figures 1 and 2 illustrate examples of gusset plate connections for an eccentrically braced frame and a special concentrically braced frame [1]. Many research papers have addressed the analyses and designs of gusset plate connections [2, 3, 4]. The stresses distributed along the edges and/or at the Whitmore effective sections of the gusset plates were the major topics discussed in these papers.

When a bracing member is subjected to a compressive force, the gusset plate, which is connected to the bracing member, will be stressed in compression and shear. However, since the vertical main member is deflecting away from the bracing member (refer to the lower left-hand quarter portion of the braced frame shown in Figures 3(a) & (b)), the angle between the vertical main member and the horizontal main member is enlarged. As a result, tensile stresses are also introduced to the gusset plate.

The effects of frame deformation on gusset plates for diagonal bracing elements loaded in compression were investigated by Cheng, Grondin, and Yam [5] using full-scale tests. Their tests found that the capacity of the gusset plate was reduced due to the effects of frame deformation on the gusset plate.

Similarly, for a reverse condition, when a bracing member is subjected to a tensile force, the gusset plate, which is connected to the bracing member, will be stressed in tension and shear. However, since the vertical main member is deflecting toward the bracing member (refer to the lower left-hand quarter portion of the braced frame shown in Figures 3(c) & (d)), the angle between the vertical main member and the horizontal main member is reduced. As a result, compressive stresses are also introduced to the gusset plate.

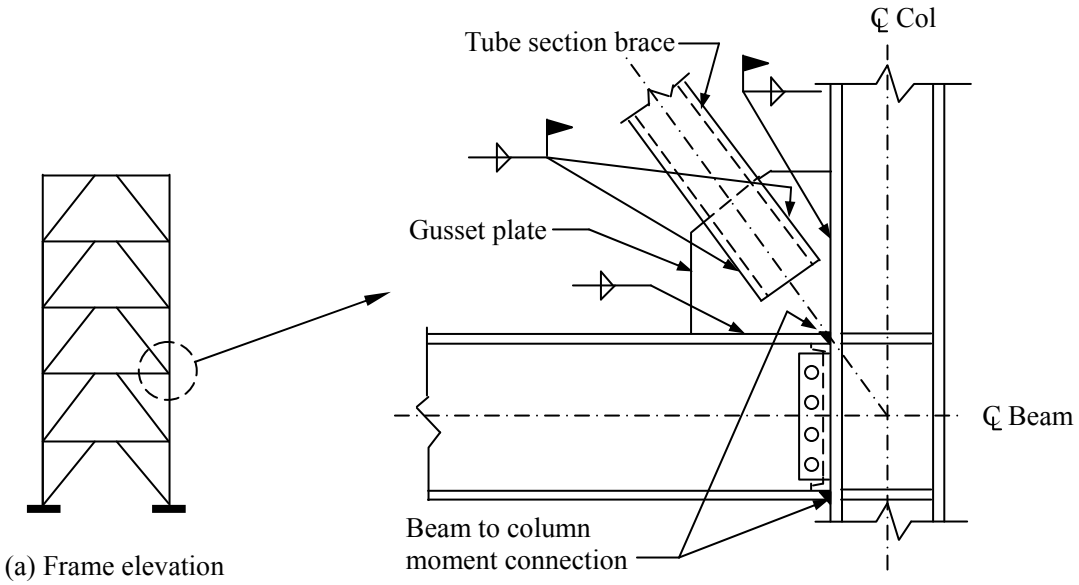

Figure 1. Gusset Plate Connection Example for an Eccentrically Braced Frame

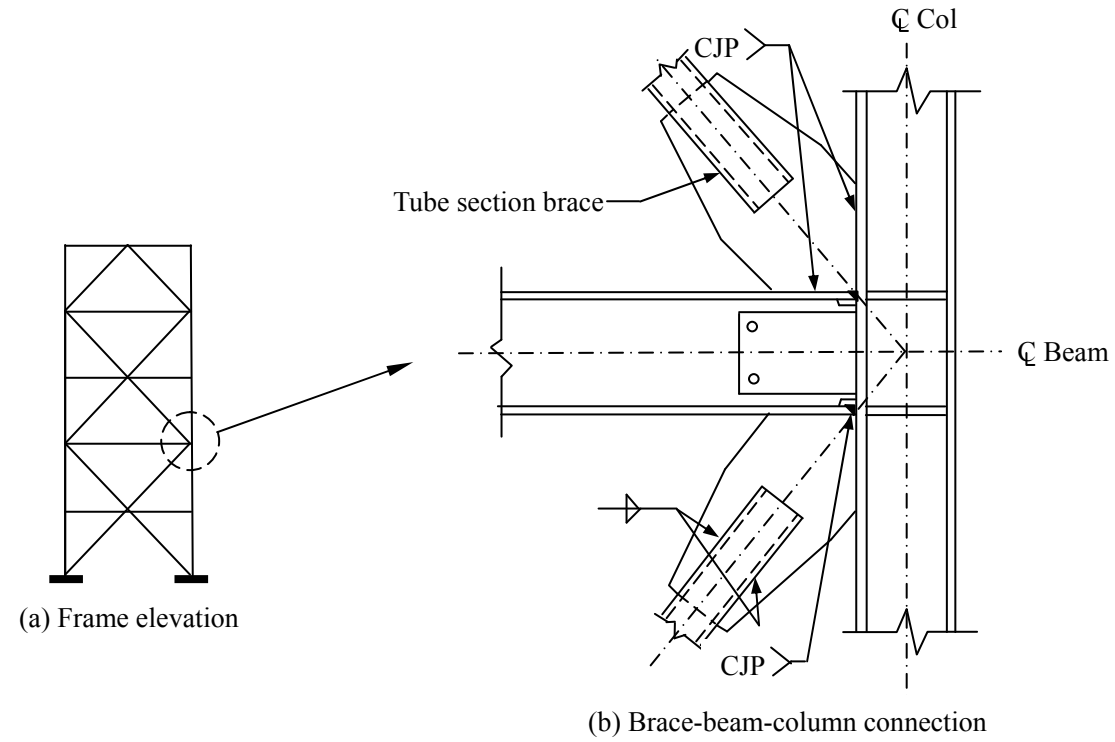

Figure 2. Gusset Plate Connection Example for a Special Concentrically Braced Frame

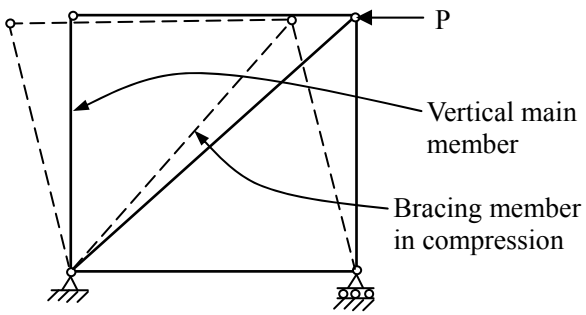

(a) Pinned-joint frame (bracing member in compression)

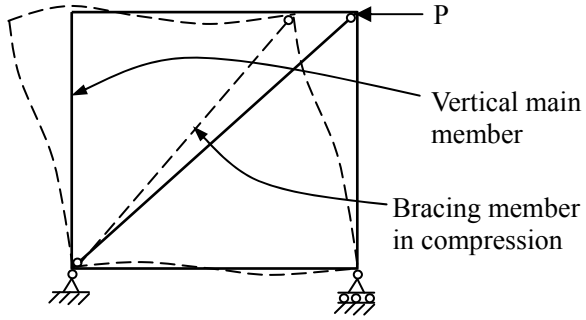

(b) Rigid-joint frame (bracing member in compression)

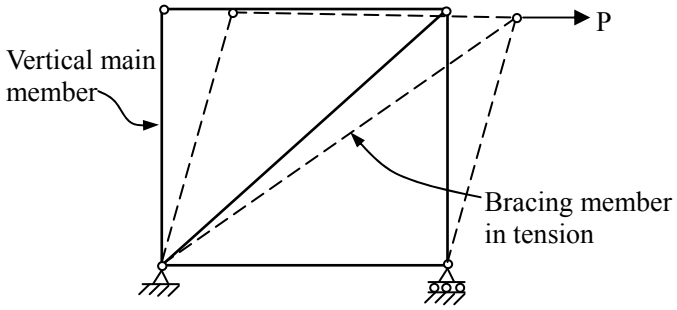

(c) Pinned-joint frame (bracing member in tension)

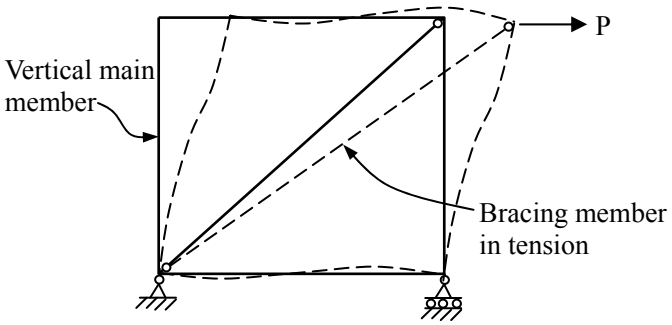

(d) Rigid-joint frame (bracing member in tension)

Figure 3. Deformations of Laterally Loaded Braced Frames

The effects of frame deformations on a welded gusset plate for a diagonal bracing element loaded in tension are investigated and the results are presented in this paper. This study is limited to the following conditions: (1) the gusset plate, the web of the beam (the horizontal member) and the

web of the column (the vertical member) are in the same plane; (2) as shown in Figures 1 and 2, the beam (the horizontal member) is rigidly connected to the column (the vertical member); (3) the bracing element is welded to the gusset plates and is loaded in tension; and (4) fillet welds are used for the gusset-to-bracing element, gusset-to-beam, and gusset-to-column connections.

2. DESIGN EXAMPLE OF A GUSSET PLATE CONNECTION FOR A DIAGONAL BRACING ELEMENT LOADED IN TENSION

The following is a design example of a gusset plate connection for a diagonal bracing element loaded in tension. Two C3×6 channels are used as the diagonal bracing element in a rigid frame as shown in Figure 4. ASTM A36 steel is used for the columns, beams, bracing member, and the gusset plates. Note that in the U.S., A992 steel is the preferred material for W shapes, while the availability of A36 should be confirmed prior to the use of it. Also, E70XX electrodes having a minimum tensile strength of 483 MPa (70 ksi) are used for the fillet weld made by shielded metal arc welding (SMAW). Assume that the factored tensile force, P_u, applied to the bracing element is 507 kN (114 kips).

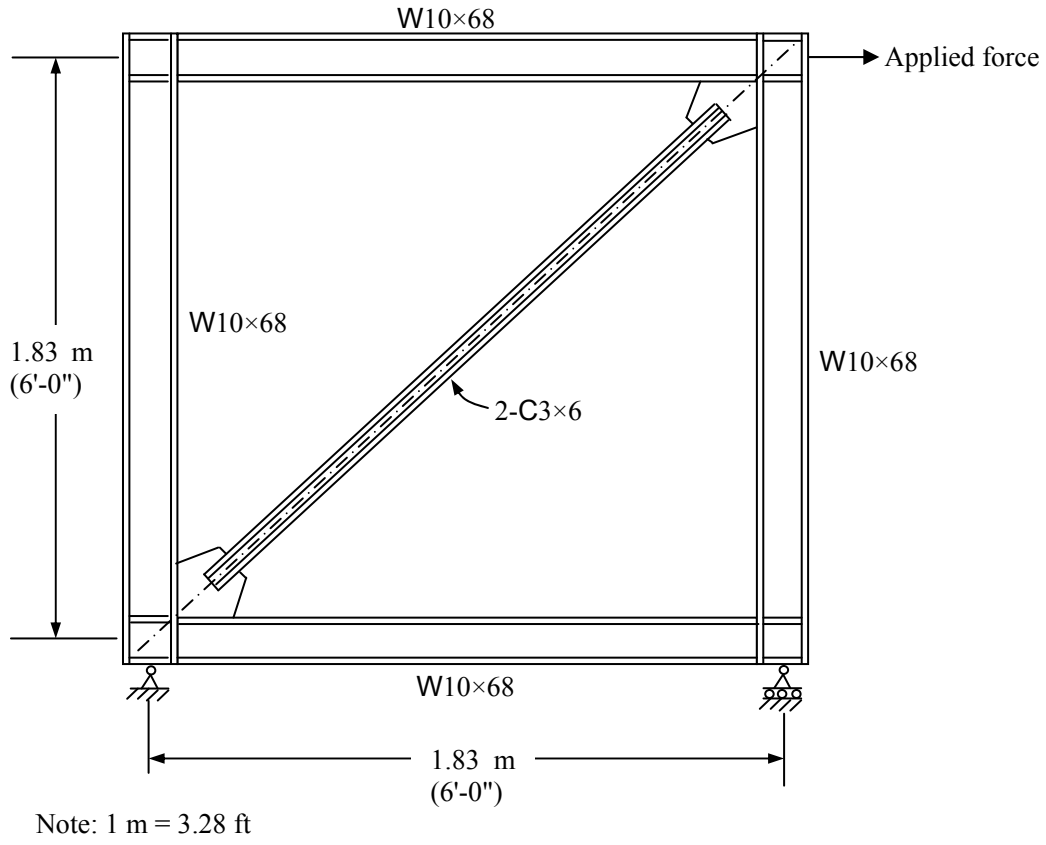

Figure 4. Braced Frame Elevation

Design of a gusset plate connection using the hand-calculated approach

The following hand-calculated approach illustrates the use of the Whitmore section [6, 7] and the Uniform Force Method [1, 7, 8, 9] for the design of the gusset plate connection for the diagonal bracing element loaded in tension.

1. Compute the design tensile strength of the bracing member [7]:

   (a) For tensile yielding in the gross section:

   $$\phi_t P_n = \phi_t F_y A_g = 0.9\ (248\ \text{MPa})\ (2270\ \text{mm}^2) = 507\ \text{kN}\ (114\ \text{kips}) \geq P_u \qquad \textbf{o.k.}$$

   where $\phi_t P_n$ = design tensile strength; F_y = specified minimum yield stress of the type of steel being used [F_y = 248 MPa (36 ksi) for A36 steel]; and A_g = gross area of the bracing member [A_g = 2270 mm^2 (3.52 in^2) for 2-C3×6].

   (b) For tensile rupture in the net section:

   $$U = 1 - \frac{\bar{x}}{l} = 1 - \left(\frac{11.6}{200}\right) = 0.942$$

   $$\phi_t P_n = \phi_t F_u A_n U = 0.75\ (400\ \text{MPa})\ (2270\ \text{mm}^2)\ (0.942) = 642\ \text{kN}\ (144\ \text{kips}) \geq P_u \qquad \textbf{o.k.}$$

   where U = reduction coefficient, used in calculating effective net area; $\bar{x}$ = horizontal distance from the outer edge of a channel web to its centroid; l = length of the weld (assume that each weld length for the bracing element-to-gusset plate connection is 200 mm (8 in.); the assumed length will be verified in the following step); $\phi_t P_n$ = design tensile strength; F_u = specified minimum tensile strength of the type of steel being used [F_u = 400 MPa (58 ksi) for A36 steel]; and A_n = net area.

2. Design the fillet weld for the bracing element-to-gusset plate connection:
   In order to avoid brittle failure of connections, the capacity of the welded connection is recommended to be at least equal to or greater than the axial tension yield capacity of the bracing member determined using a conservative expected yield stress of 1.1 $R_y F_y$ [4]. Therefore, the axial tension yield capacity of the bracing member (2-C3×6) can be computed as follows:

   $1.1\ R_y F_y A_g = 1.1\ (1.5)\ (248\ \text{MPa})\ (2270\ \text{mm}^2) = 929\ \text{kN}\ (209\ \text{kips})$

   where R_y = ratio of the expected yield strength to the specified minimum yield strength of the grade of steel to be used (R_y = 1.5 for ASTM A36 steel channels [10]).

   Using an 8 mm ($^5/_{16}$ in.) fillet weld, the effective throat of the 8mm ($^5/_{16}$ in.) fillet weld is
   t_e = (8 mm) (0.707) = 5.66 mm (0.22 in.)

   Therefore, the capacity of weld per inch can be computed as follows:
   0.75 t_e (0.60 F_{EXX}) = 0.75 (5.66 mm) (0.60) (483 MPa) = 1.23 kN/mm (7.0 kips/in.)

   Using a length of 200 mm (8 in.) for each fillet weld, since there are a total of four (4) 200 mm-long welds for the bracing element-to-gusset plate connection, the total welding capacity is 984 kN (222 kips) (= 4 × 1.23 kN/mm × 200 mm), which is larger than 929 kN (209 kips) (the axial tension yield capacity of the bracing member). Therefore, the capacity of the fillet weld for the bracing element-to-gusset plate connection is adequate. Figure 5 illustrates the fillet weld for the bracing element-to-gusset plate connection.

3. Determine the thickness of the gusset plate using the Whitmore section:
In order to increase global ductility of a braced frame, yielding of the bracing member shall occur before the yielding of the gusset plate [4]. Therefore, the following equation is suggested for the determination of the gusset plate thickness:

$$R_y F_y A_g \leq F_y A_e \quad (1)$$

where R_y = 1.5 for ASTM A36 steel; F_y = 248 MPa (36 ksi) for ASTM A36 steel; A_g = cross area of steel channels (bracing member); and A_e = area of the Whitmore effective section of the gusset plate.

Referring to Figures 5 and 6, the Whitmore effective width [7] of the plate is:

l_w = 2 (200 mm)(tan 30°) + 76 mm = 307 mm (12.2 in.)

Note that 76 mm (3 in.) is the depth of the C3×6 channels. Therefore, the area of the Whitmore effective section can be computed as follows:

$A_e = (l_w)(t)$ = 307t mm^2 (12.2t in.^{2})

Note that t is the thickness of the gusset plate. From Eq. 1, one has
1.5 (248 MPa) (2270 mm^2) ≤ 248 MPa (307t mm^2)
[1.5 (36 ksi) (3.52 in.^{2}) ≤ 36 ksi (12.2t in.^{2})]
From which, the minimum required thickness t = 11.1 mm (0.43 in.). Therefore, 12 mm ($^{15}/_{32}$ in.) is used for the thickness of the gusset plate.

4. Determine the configuration of the gusset plate:
The configuration of the gusset plate shown in Figure 5 was determined based on the following criteria: (1) A minimum length of 25 mm (1 in.) is provided on each side of the bracing element along the gusset plate edge, which is perpendicular to the diagonal bracing element. (2) Weld is terminated not less than one weld size from edge of the gusset plate. Since the weld size is 8 mm ($^5/_{16}$ in.), 10 mm ($^3/_8$ in.) is provided for the required distance as shown in Figure 5. (3) The re-entrant corner of the gusset plate is located at the intersection of the face of the column (or the face of the beam) and the 30° line as shown in Figures 5 and 6). (4) The distance from the end of the bracing element to the line that connects the two re-entrant corners is not less than two times the thickness of the gusset plate in order to ensure that the gusset plate can freely rotate when the bracing element is subjected to a compression force [4]. Since the thickness of the gusset plate is 12 mm ($^{15}/_{32}$ in.), 24 mm ($^{15}/_{16}$ in.) is provided for the required distance as shown in Figure 5.

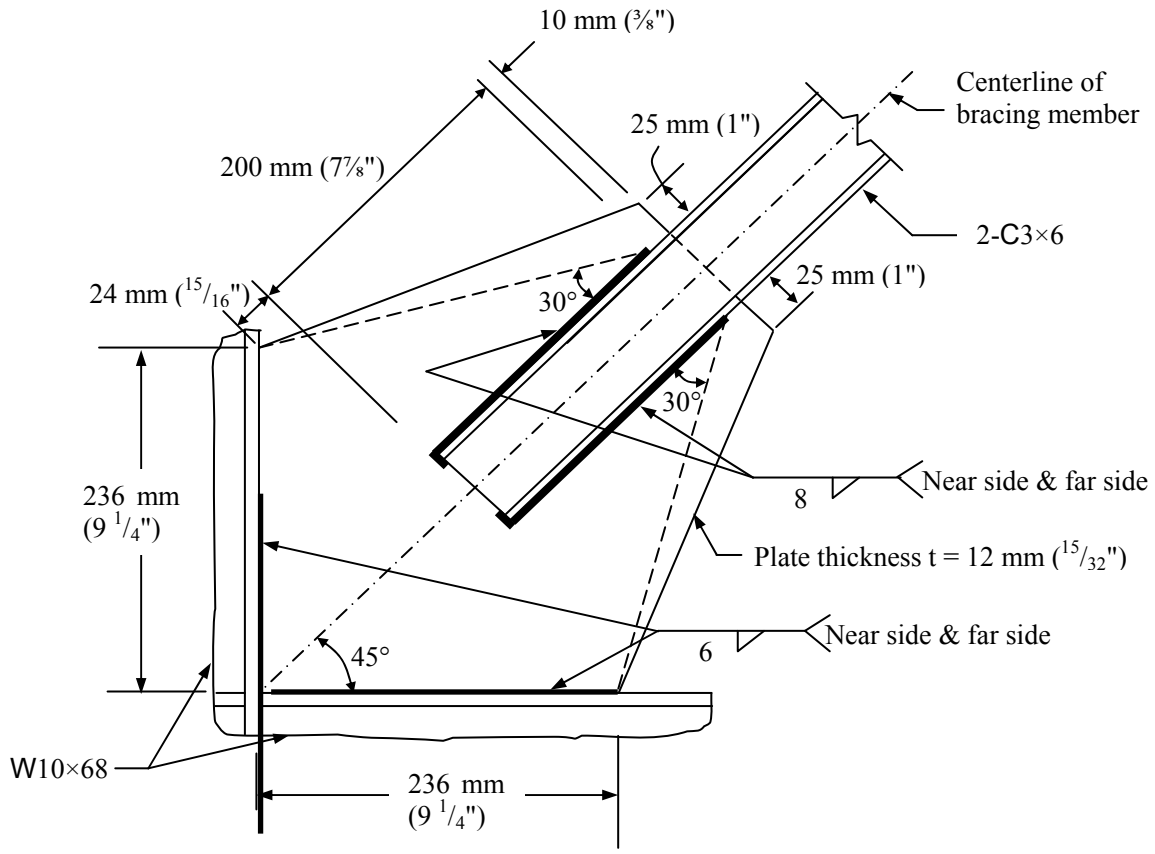

Note: 1 mm = 0.0394 in.

Figure 5. Gusset Plate Connection for a Diagonal Bracing Element

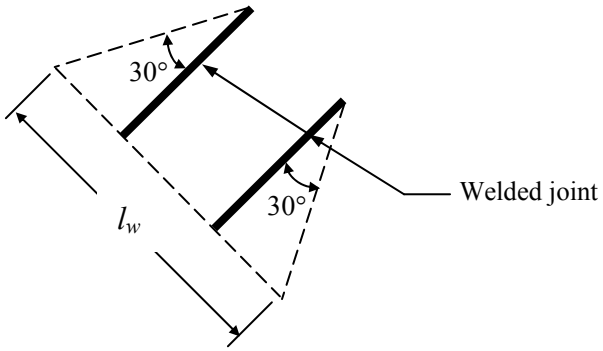

Figure 6. The Effective Width of the Whitmore Section for a Welded Joint

5. Determine the adequacy of the thickness of the gusset plate using the Uniform Force Method: Using the connection geometry shown in Figures 5 and 7, five geometric parameters e_b, e_c, α, β, and r can be determined as:

   One-half the depth of the beam (the horizontal element W10×68), $e_b = d_b/2 = (264 \text{ mm})/2 = 132$ mm (5.2 in.).

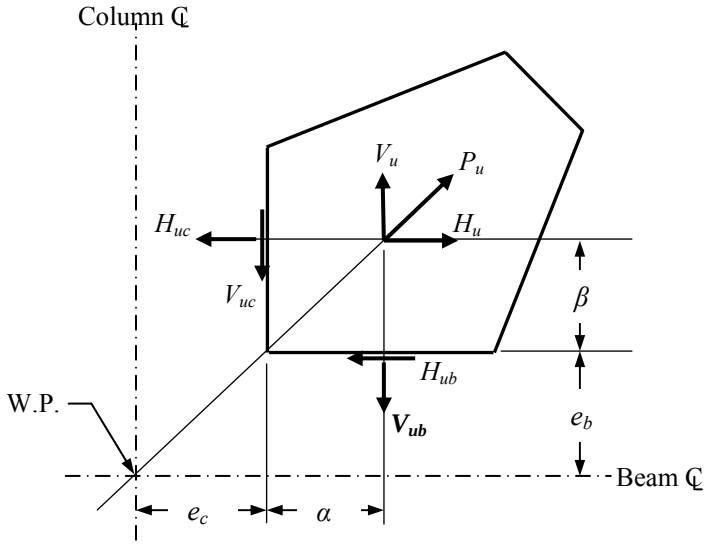

Figure 7. Gusset Plate Free-body Diagram

One-half the depth of the column (the vertical element W10×68), $e_c = d_c/2$ = (264 mm)/2 = 132 mm (5.2 in.).

The distance from the face of the column flange to the centroid of the gusset-to-beam connection, α = 118 mm (4.6 in.).

The distance from the face of the beam flange to the centroid of the gusset-to-column connection, β = 118 mm (4.6 in.).

The distance from the working point (as shown in Figure 7) to the centroid of the gusset plate connection,

$$r = \sqrt{(\alpha + e_c)^2 + (\beta + e_b)^2} = \sqrt{(118\text{ mm} + 132\text{ mm})^2 + (118\text{ mm} + 132\text{ mm})^2}$$
$$= 354\text{ mm (13.9 in.)}$$

Therefore, the factored shear force at the gusset-to-column connection,

$$V_{uc} = \frac{\beta}{r} P_u = \frac{118\text{ mm}}{354\text{ mm}}(507\text{ kN}) = 169\text{ kN (38.0 kips)}$$

The factored axial force at the gusset-to-column connection,

$$H_{uc} = \frac{e_c}{r} P_u = \frac{132\text{ mm}}{354\text{ mm}}(507\text{ kN}) = 189\text{ kN (42.5 kips)}$$

The factored axial force at the gusset-to-beam connection,

$$V_{ub} = \frac{e_b}{r} P_u = \frac{132\text{ mm}}{354\text{ mm}}(507\text{ kN}) = 189\text{ kN (42.5 kips)}$$

The factored shear force at the gusset-to-beam connection,

$$H_{ub} = \frac{\alpha}{r} P_u = \frac{118 \text{ mm}}{354 \text{ mm}} (507 \text{ kN}) = 169 \text{ kN (38.0 kips)}$$

The next step is to check the design strength at the horizontal and vertical edges of the gusset plate against the combined effects of the factored tension and shear forces using the von Mises yield criterion [1].

The combined effects of the factored tension and shear forces at the vertical edge of the gusset plate can be computed as follows:

$$\mathrm{P_u} = \sqrt{\mathrm{H_{uc}^2} + 3\mathrm{V_{uc}^2}} = \sqrt{(189 \text{ kN})^2 + 3(169 \text{ kN})^2} = 348 \text{ kN (78.2 kips)}$$

The design strength at the vertical edge of the gusset plate is

$\phi P_n = \phi(2\beta)tF_y = 0.9$ (2 × 118 mm) (12 mm) (248 MPa) = 632 kN (142.1 kips)

Therefore, the design strength at the vertical edge is larger than the combined effects of the factored tension and shear forces.

The result at the horizontal edge of the gusset plate will be the same as that at the vertical edge of the gusset plate since the horizontal and vertical edges are symmetric about the diagonal bracing element.

The results shown above indicate that the thickness of the gusset plate is adequate.

6. Design the fillet weld for the gusset-to-W10×68 flange connection using the Uniform Force Method:

Since H_{ub} = 169 kN (38.0 kips), the shear force along the gusset-to-beam interface can be computed as follows:

$$\mathrm{f_v} = \frac{169 \text{ kN}}{236 \text{ mm}} = 0.716 \text{ kN/mm (4.09 kips/in.)}$$

Also, since V_{ub} = 189 kN, the tension force along the gusset-to-beam interface can be computed as follows:

$$\mathrm{f_a} = \frac{189 \text{ kN}}{236 \text{ mm}} = 0.801 \text{ kN/mm (4.57 kips/in.)}$$

Furthermore, since there is no in-plane bending stress along the gusset-to-beam interface, f_b = 0 KN/mm. Therefore, the peak and average forces at the gusset-to-beam interface [9] can be computed as follows:

$$f_{peak} = \sqrt{f_v^2 + (f_a + f_b)^2} = \sqrt{f_v^2 + f_a^2} = 1.074 \text{ kN/mm (6.13 kips/in.)}$$

$$f_{avg} = (1/2)\left(f_{peak} + \sqrt{f_v^2 + (f_a - f_b)^2} \right) = \sqrt{f_v^2 + f_a^2} = 1.074 \text{ kN/mm (6.13 kips/in.)}$$

Note that when the gusset is directly welded to the beam or column, the connection should be designed for the larger of the peak stress and 1.25 times the average stress, but the weld size need not be larger than that required to develop the strength of the gusset [9]. Therefore, the connection should be designed for the stress of 1.343 kN/mm (7.67 kips/in.) (= 1.25 × 1.074 kN/mm), but need not be larger than 2.678 kN/mm (15.2 kips/in.). Note that ϕtF_y = 0.9 (12 mm) (248 MPa) = 2.678 kN/mm (ϕtF_y = 0.9 (0.47 in.) (36 ksi) = 15.2 kips/in.).

Using a 6 mm fillet weld, the design strength of the fillet weld for the gusset-to-beam (W10×68) flange connection can be computed as follows:

$$\phi R_n = 2 \times 0.75(0.6F_{EXX}t_e) = 2 \times 0.75\left[0.6 \times 0.483 \times \frac{\sqrt{2}}{2} \times 6\right] = 1.844 \text{ kN/mm} \quad (10.53 \text{ kips/in.})$$

Since the design strength is larger than the required strength of 1.343 kN/mm (7.67 kips/in.), the horizontal fillet weld for the gusset-to-beam flange connection is adequate. The same approach can be repeated to determine the adequacy of the vertical fillet weld for the gusset-to-column flange connection.

Figure 5 summarizes the results of the above hand-calculated approach. Note that the hand-calculated approach neglects the effects of frame deformation on the gusset plate.

3. INVESTIGATION OF GUSSET PLATE CONNECTION USING FINITE ELEMENT METHOD

The following investigation procedure illustrates the use of the finite element method for the determination of the adequacy of the gusset plate connection, which was designed using the hand-calculated approach presented above. Nonlinear static analyses have been conducted using the computer software NISA/DISPLAY [11] for the finite element approaches. The elastic, linear hardening stress-strain curve (derived from Salmon et al. [12]), with F_y = 248 MPa (36 ksi), corresponding to a strain of 0.00124 mm/mm (in./in.) and F_u = 400 MPa (58 ksi), corresponding to a strain of 0.185 mm/mm (in./in.), has been used as the material property for the A36 steel. Assuming that the E7018 electrode was used for the fillet weld, the elastic, linear hardening stress-strain curve (derived from the Lincoln Electric Company [13]), with F_y = 448 MPa (65 ksi), corresponding to a strain of 0.00224 mm/mm (in./in.) and F_u = 510 MPa (74 ksi), corresponding to a strain of 0.15 mm/mm (in./in.), has been used as the material property for the fillet weld. In the strain-hardening range, the stress again increases and continues up to the tensile strength. In this paper, the elastic, linear hardening stress-strain curves were used in order to conduct the nonlinear static finite element analyses, as well as to determine the actual location of the maximum first-principal stress (which is related to the occurrence of fracture if the stress reaches the tensile strength, the limiting value in tension) in the gusset plate. Two approaches have been used for the investigation; one neglects the effects of frame deformation on the gusset plate while the other one considers the effects.

Finite element approach I - neglecting the effects of frame deformation on the gusset plate:

The lower left-hand quarter portion of the braced frame shown in Figure 4 was used for the development of the finite element model as shown in Figure 8. The model was made of 3-D solid elements. A pinned condition was used at the free end of the beam and column as well as at the base of the gusset-beam-column connection. In this model, an additional plate was added to the base of the gusset-beam-column connection in order to mitigate the stress concentration caused by the pinned support [Figure 8(a)].

A load increment was applied at the end of the bracing element. As the load gradually increased, the stress concentration gradually accumulated at the end of the welded joint, as well as at the start of the welded joint (Figures 9, 10, and 11). When the load applied to the bracing element reached 507 kN (114 kips), as shown in Figure 8(b), the von Mises stress reached 215 MPa (31.2 ksi) and 286 MPa (41.5 ksi) at the end of the welded joint and the start of the welded joint, respectively, as shown in Figure 10. Meanwhile, the first-principal stress reached 223 MPa (32.3 ksi) and 219 MPa (31.8 ksi) at the end of the welded joint and the start of the welded joint, respectively, as shown in Figure 11.

The above results indicate that when the load applied to the bracing element reaches 507 kN (114 kips), the maximum von Mises stress located at the start of the welded joint reaches 286 MPa (41.5 ksi), which is larger than 248 MPa (36 ksi) (the specified minimum yield stress of the A36 steel). Therefore, yielding is expected to initiate at the start of the welded joint. However, since the maximum first-principal stress, 223 MPa (32.3 ksi), located at the end of the welded joint is less than 400 MPa (= 58 ksi, the specified minimum tensile strength of the A36 steel), fracturing is not expected to happen in the gusset plate.

Moreover, when the load applied to the bracing element reaches 507 kN (114 kips), the shear stress (S_{xy}) distributions along the gusset edges are shown in Figure 12, the normal stress (S_{xx}) distribution along the vertical gusset edge is shown in Figure 13, and the normal stress (S_{yy}) distribution along the horizontal gusset edge is shown in Figure 14. The resultant forces for the shear and tensile stresses are shown in Figure 15.

Figure 15 indicates that the resultant shear force acting along the horizontal and vertical gusset edges is 177 kN (39.8 kips), which is about 5% larger than that obtained from the hand-calculated approach (169 kN (38.0 kips)), as shown in the design example. Also, the resultant tensile force acting on the horizontal and vertical edges is 181 kN (40.7 kips), which is about 4% less than that obtained from the hand-calculated approach (189 kN (42.5 kips)), as shown in the design example.

Figure 15 also indicates that the resultant tensile force acting on the horizontal gusset edge is located outside the distance ‘α’ (the distance from the face of the column flange to the centroid of the gusset-to-beam connection) and the resultant tensile force acting on the vertical gusset edge is located outside the distance ‘β’ (the distance from the face of the beam flange to the centroid of the gusset-to-column connection). Note that as shown in Figure 7, the hand-calculated approach assumes that the resultant tensile force (V_{ub}) acting on the horizontal gusset edge is located at the centroid of the gusset-to-beam connection, while the resultant tensile force (H_{uc}) acting on the vertical gusset edge is located at the centroid of the gusset-to-column connection.

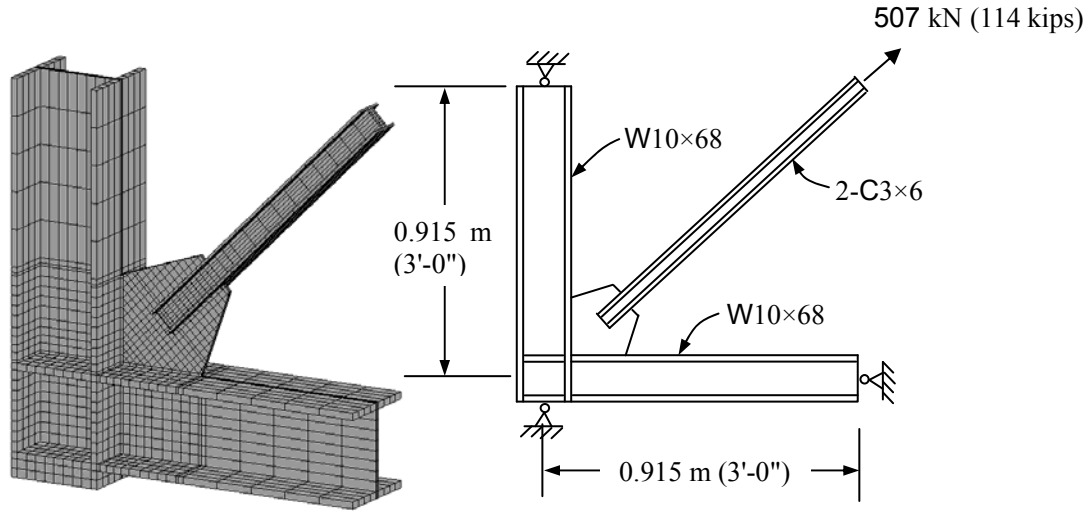

(a) Computer model

(b) Boundary condition of the model

Notes: 1 m = 3.28 ft; 1 kN = 0.2248 kips

Figure 8. Finite Element Model Neglecting Frame Deformation Effects

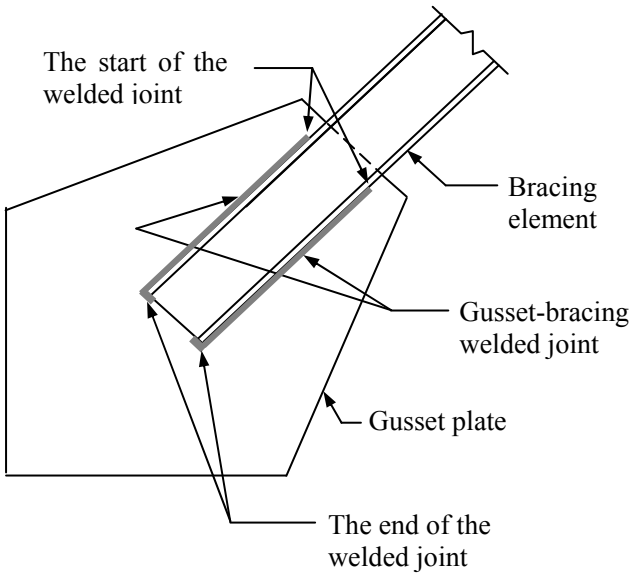

Figure 9. Gusset Plate-bracing Element Welded Joint

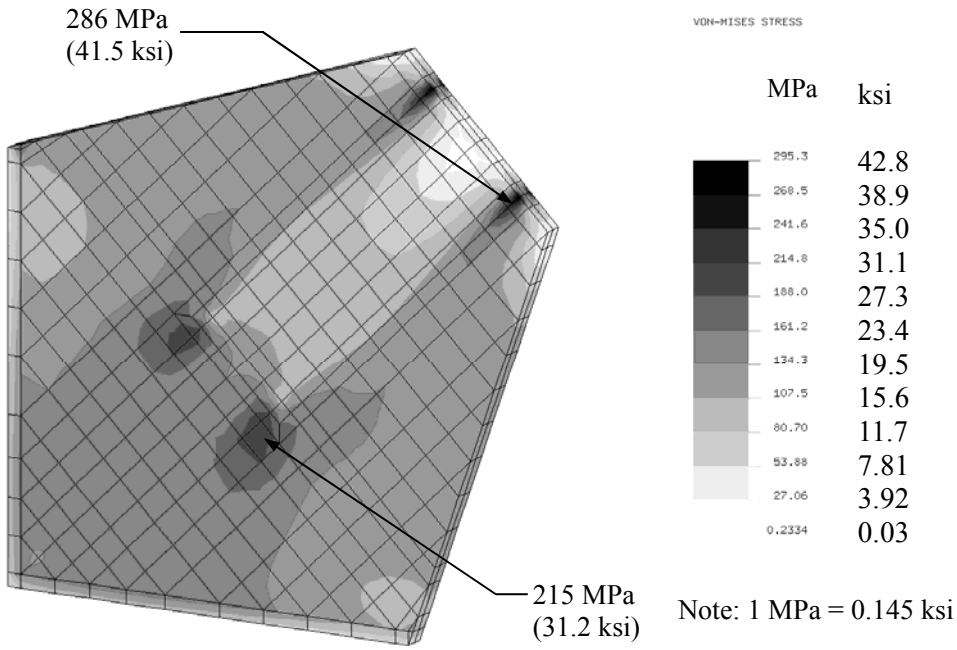

Figure 10. Von Mises Stress Distribution on Gusset Plate Neglecting Frame Deformation Effects

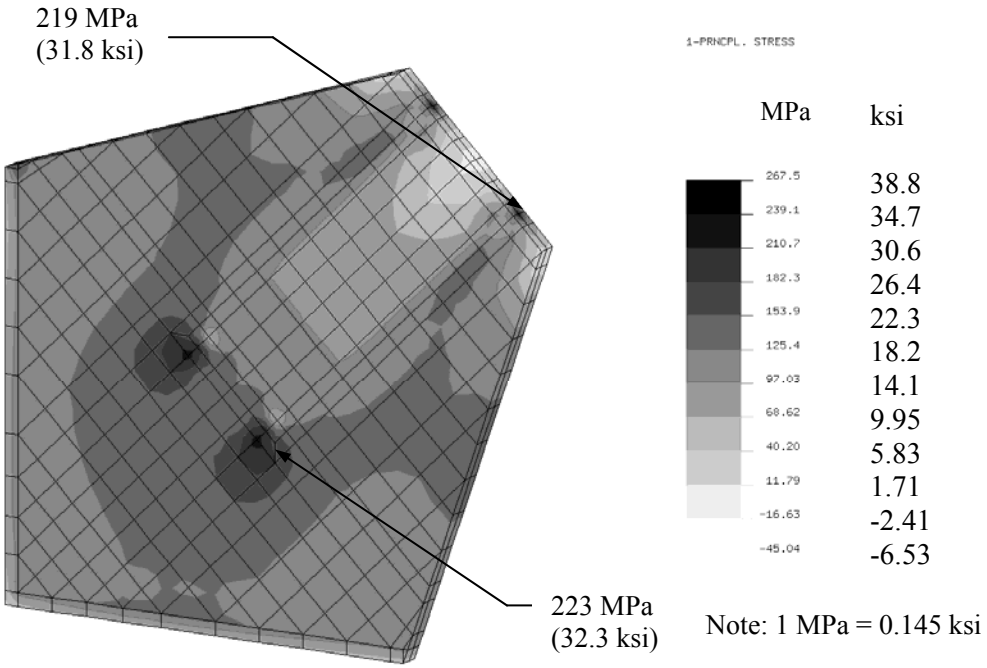

Figure 11. First-principal Stress Distribution on
Gusset Plate Neglecting Frame Deformation Effects

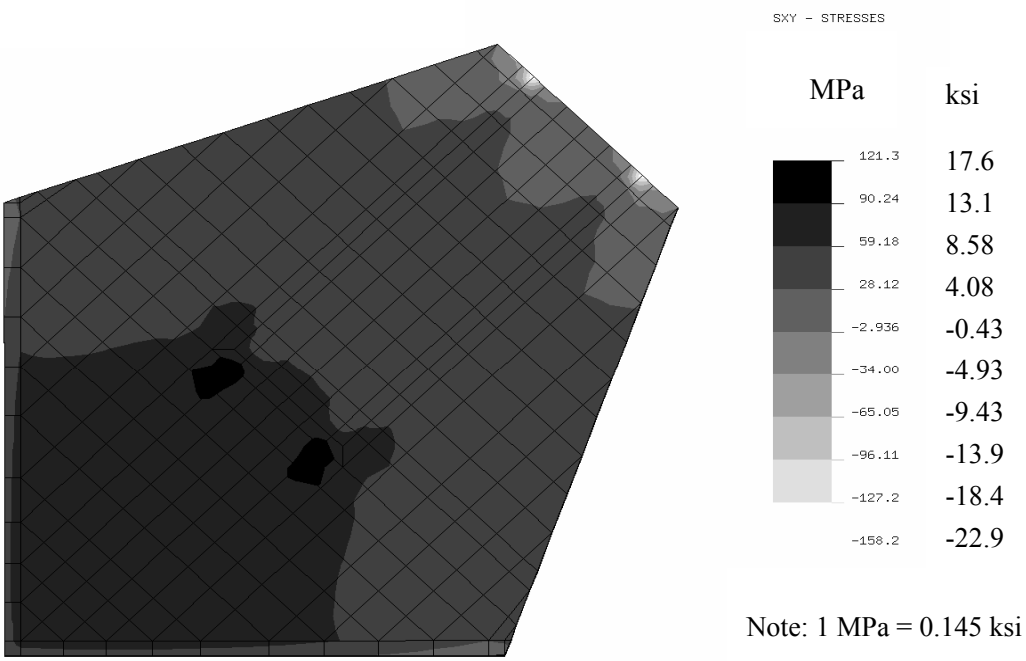

Figure 12. Shear Stress Distributions on
Gusset Edges Neglecting Frame Deformation Effects

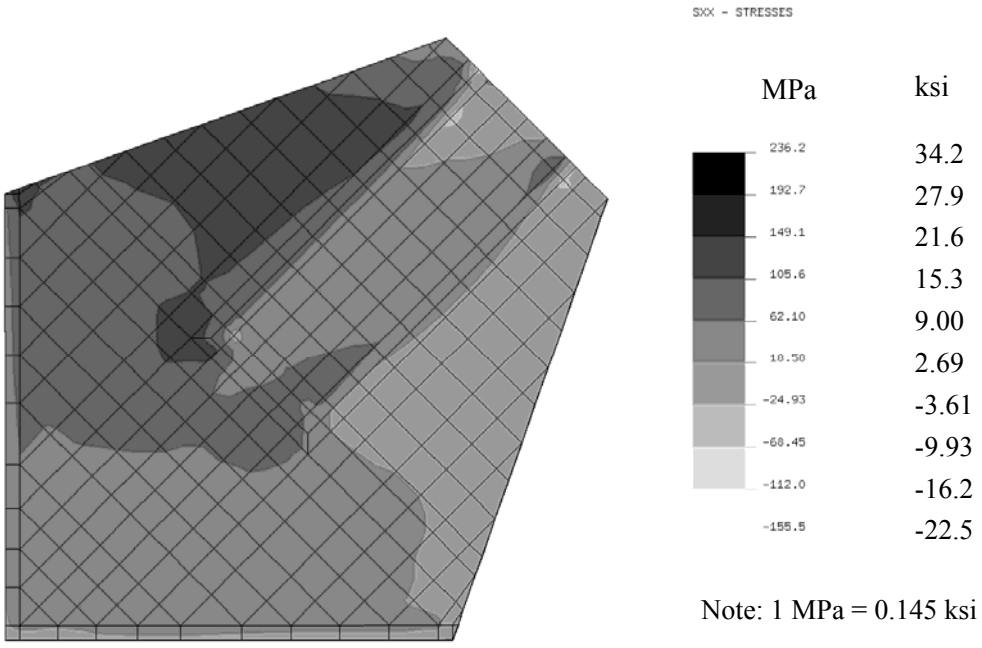

Figure 13. Normal Stress Distribution on
Vertical Gusset Edge Neglecting Frame Deformation Effects

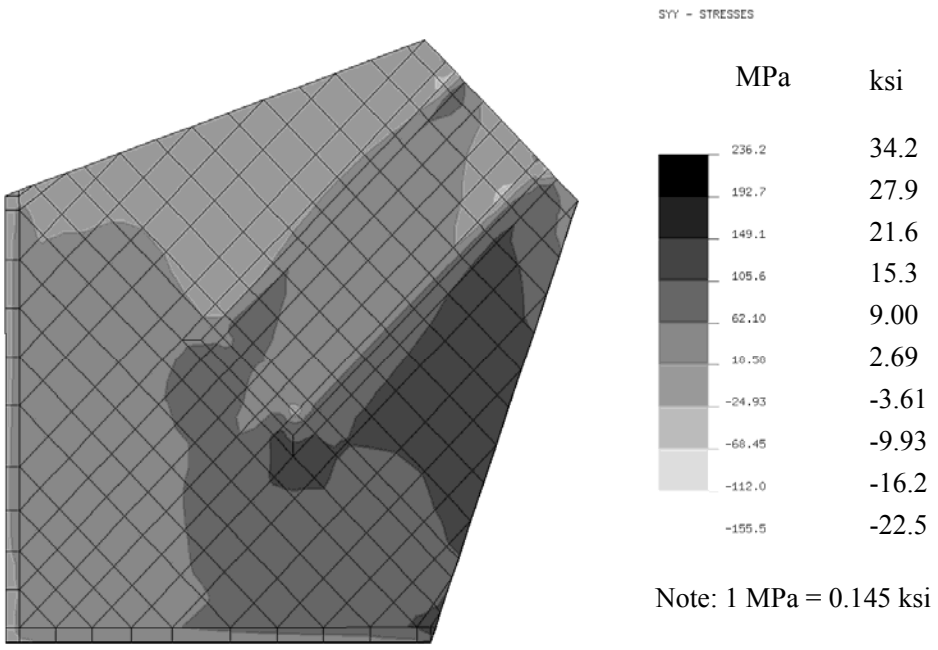

Figure 14. Normal Stress Distribution on
Horizontal Gusset Edge Neglecting Frame Deformation Effects

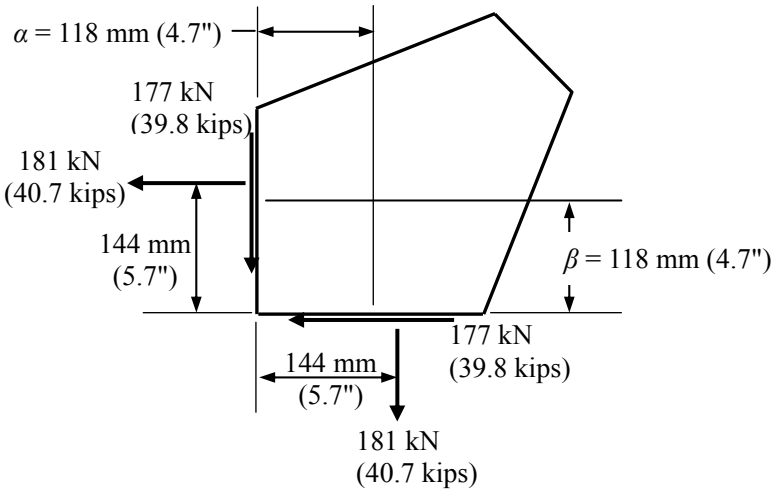

Figure 15. Resultant Shear and Tensile Forces Acting on
Gusset Edges Neglecting Frame Deformation Effects

Finite element approach II - considering the effects of frame deformation on the gusset plate:

The entire braced frame shown in Figure 4 was used for the development of the finite element model as shown in Figure 16(a). A pinned condition was used at the base of the gusset-beam-column connection, as well as at the base of the beam-column connection. In this model, an additional plate was added to each of the bases in order to mitigate the stress concentrations caused by the pinned supports.

A load increment was applied horizontally at the upper right-hand corner of the frame as shown in Figures 4 and 16(b). When the applied load reached 485 kN (109 kips), the tensile force in the bracing element reached 507 kN (114 kips). Meanwhile, the shear forces in the columns (the vertical elements) and beams (the horizontal elements) were developed. Note that these shear forces caused deformations of the column and the beam which in turn produced compressive stresses in the gusset plate. The model shown in Figure 16(a), therefore, considers the frame deformation effects on the gusset plate. The frame deformation effects on the gusset plate can be illustrated using the free-body diagram as shown in Figure 16(c). The applied shear force in the column and the reaction shear force in the beam cause the deflections of the column and the beam, which in turn produce compressive stresses in the gusset plate.

The von Mises stress distribution in the gusset plate obtained from this approach is shown in Figure 17. The maximum von Mises stress located at the start of the welded joint and the end of the welded joint reached 295 MPa (42.8 ksi) and 266 MPa (38.6 ksi), respectively. Since both of them are larger than 248 MPa (36 ksi), yielding is expected to initiate at the start of the welded joint and the end of the welded joint. Meanwhile, as shown in Figure 18, the maximum first-principal stress, 251 MPa (36.4 ksi), located at the end of the welded joint is less than 400 MPa (58 ksi), fracturing is not expected to happen in the gusset plate.

The above finite element approaches conclude that the maximum von Mises stress obtained from Approach II is about 24% more than that obtained from Approach I for the location at the end of the welded joint. Also, the maximum first-principal stress obtained from Approach II is about 13% more than that obtained from Approach I. The increases in stress were caused by the effects of frame deformation on the gusset plate.

Moreover, when the load applied to the bracing element reaches 507 kN (114 kips), the shear stress (S_{xy}) distributions along the gusset edges are shown in Figure 19, the normal stress (S_{xx}) distribution along the vertical gusset edge is shown in Figure 20, and the normal stress (S_{yy}) distribution along the horizontal gusset edge is shown in Figure 21. The resultant forces for the shear and tensile stresses are shown in Figure 22.

Figure 22 indicates that the resultant shear force acting along the horizontal and vertical gusset edges is 284 kN (63.8 kips), which is about 68% larger than that obtained from the hand-calculated approach (169 kN (38.0 kips)), as shown in the design example. Also, the resultant tensile force acting on the horizontal and vertical edges is 74 kN (16.6 kips), which is about 61% less than that obtained from the hand-calculated approach (189 kN (42.5 kips)), as shown in the design example.

Figure 22 also indicates that the resultant tensile force acting on the horizontal gusset edge is located inside the distance ‘α’ (the distance from the face of the column flange to the centroid of the gusset-to-beam connection) and the resultant tensile force acting on the vertical gusset edge is located inside the distance ‘β’ (the distance from the face of the beam flange to the centroid of the gusset-to-column connection).

Also, referring to Figure 22, the combined effects of the factored tension and shear forces at the vertical and horizontal gusset edges can be computed (using the von Mises yield criterion [1]) as $P_u = \sqrt{(74\,\text{kN})^2 + 3(284\,\text{kN})^2}$ = 497 kN (112 kips), which is about 43% more than that obtained from hand-calculated approach (348 kN (78 kips)), which neglected the effects of frame deformation, as shown in the design example. Therefore, the above finite element approaches also conclude that neglecting the effects of frame deformation may result in significant underestimation of the combined effects of the factored tension and shear forces at the gusset edges.

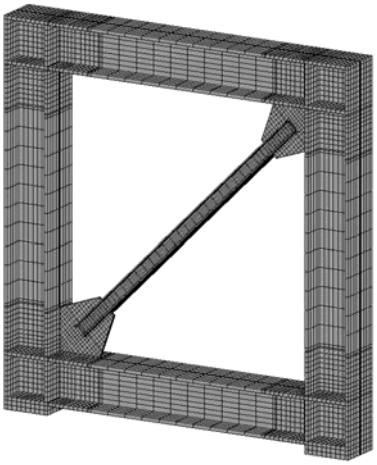

(a) Computer model

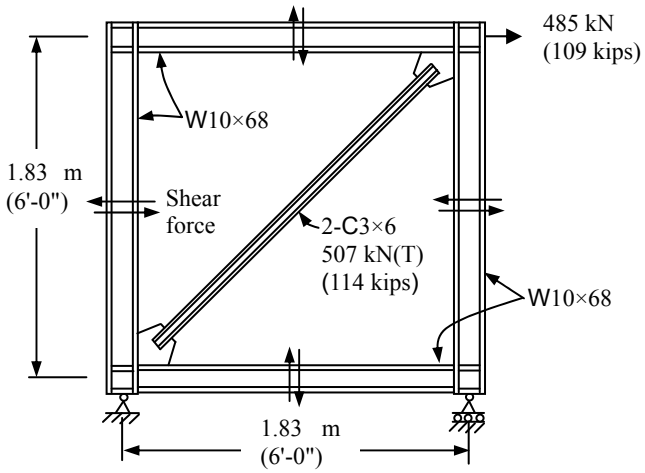

Notes: 1 m = 3.28 ft; 1 kN = 0.2248 kips

(b) Applied load

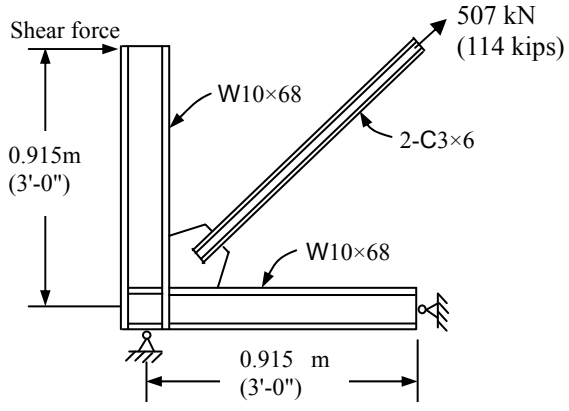

Notes: 1 m = 3.28 ft; 1 kN = 0.2248 kips

(c) Free body diagram of the model

Figure 16. Finite Element Model Considering Frame Deformation Effects

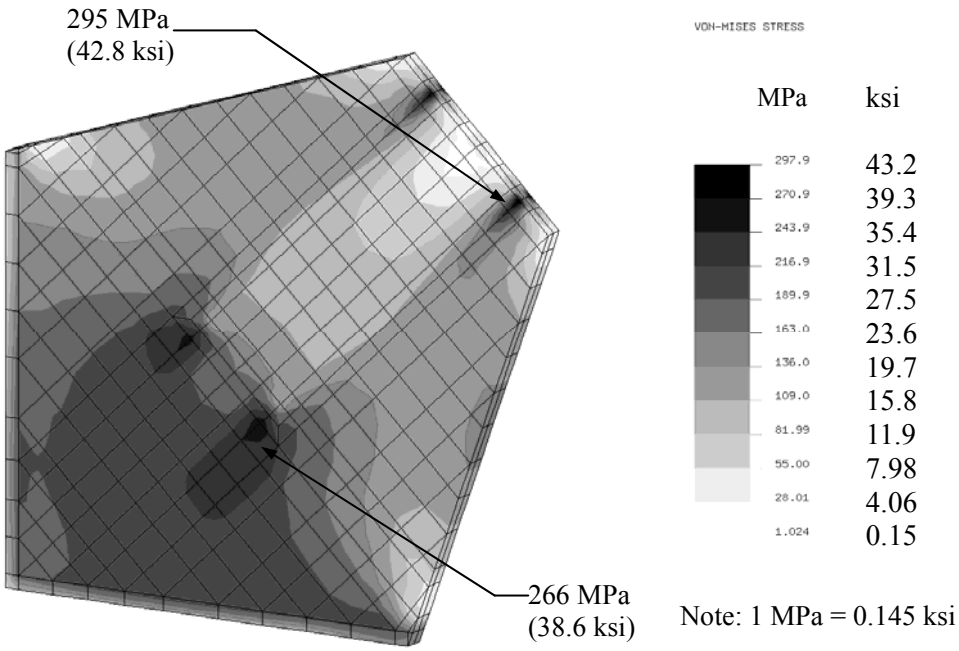

Figure 17. Von Mises Stress Distribution on Gusset Plate Considering Frame Deformation Effects

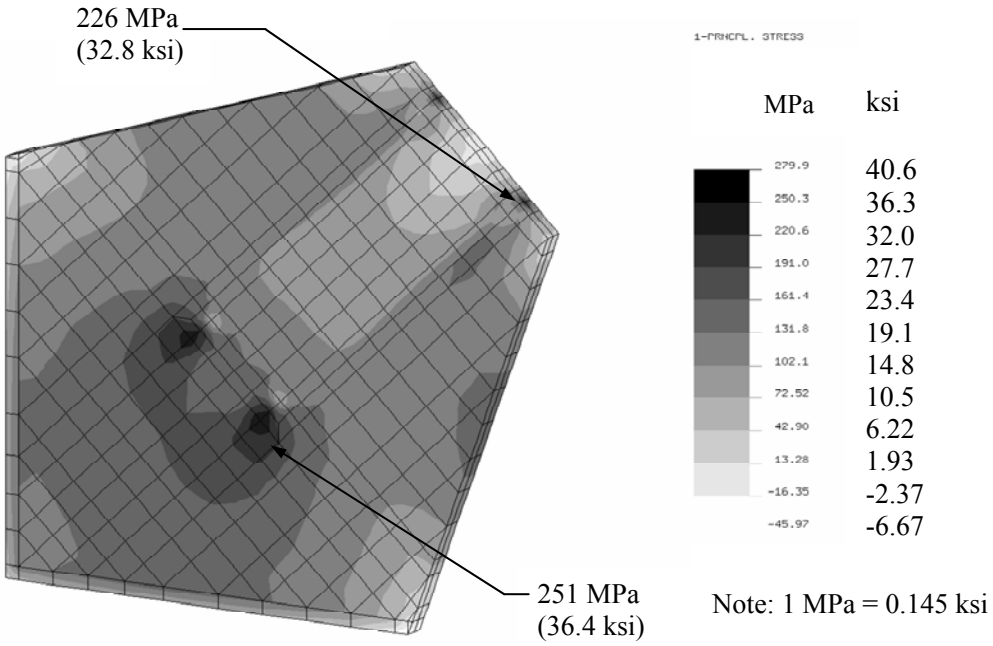

Figure 18. First-principal Stress Distribution on Gusset Plate Considering Frame Deformation Effects

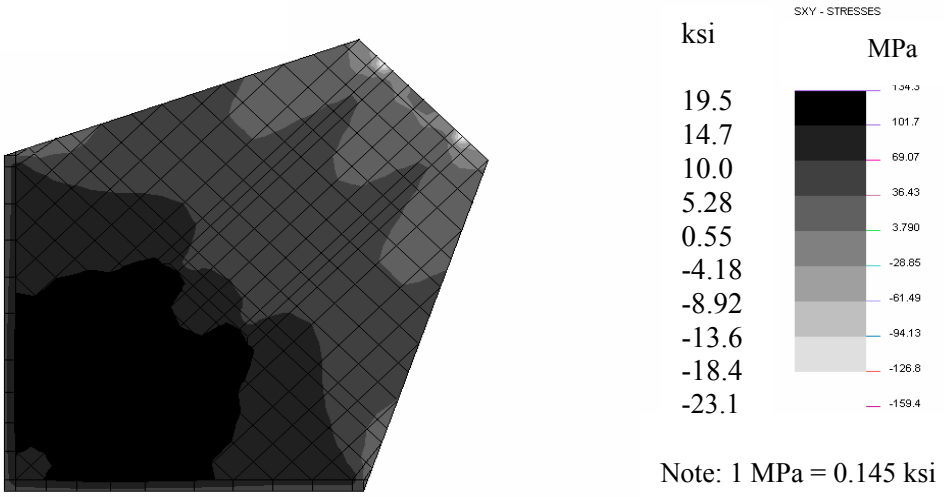

Figure 19. Shear Stress Distributions on Gusset Edges Considering Frame Deformation Effects

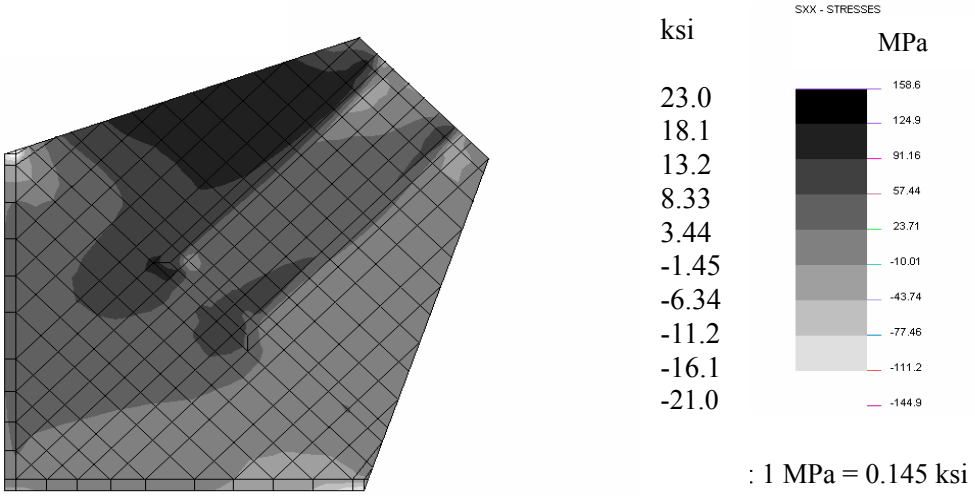

Figure 20. Normal Stress Distribution on
Vertical Gusset Edge Considering Frame Deformation Effects

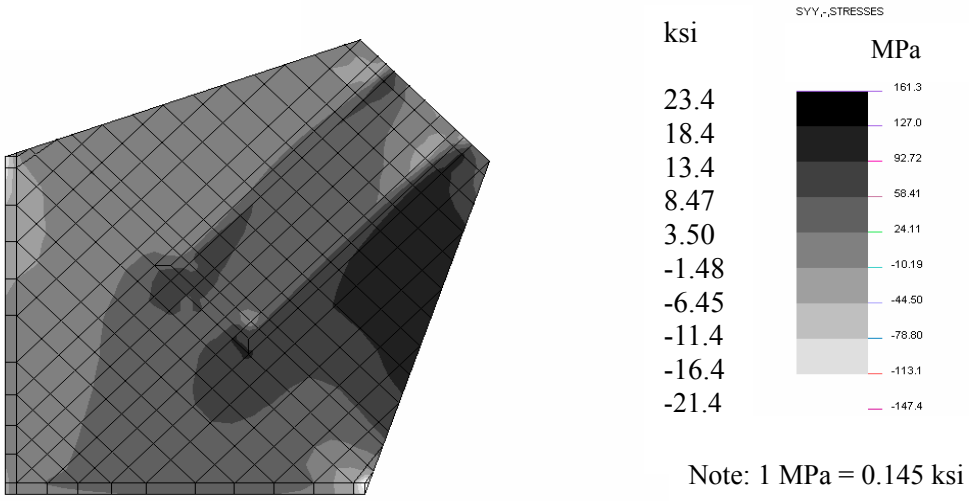

Figure 21. Normal Stress Distribution on
Horizontal Gusset Edge Considering Frame Deformation Effects

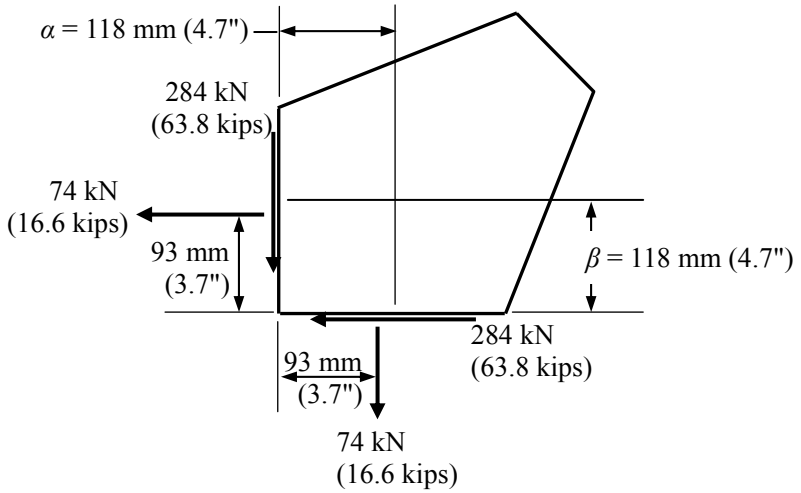

Figure 22. Resultant Shear and Tensile Forces Acting on
Gusset Edges Considering Frame Deformation Effects

4. DISCUSSION OF THE RESULTS

The results obtained from above indicate that significant increases in stress occurred at the end of the welded joint caused by the frame deformation effects on the gusset plate. Therefore, the hand-calculated approach, which neglects the frame deformation effects, may result in an under-design of the gusset plate connection. The following illustrates an under designed example caused by neglecting the deformation effects on the gusset plate:

Assume that ASTM A572 Grade 50 steel [F_y = 345 MPa (50 ksi); F_u = 448 MPa (65 ksi)] is used for the steel elements and the gusset plates as shown in Figure 4. Also assume that the factored tensile force, P_u, applied to the bracing element, is 705 kN (158 kips) (note that the factored tensile force applied to the bracing element using A36 steel was 507 kN (114 kips)). The required thickness of the gusset plate can be determined to be 9 mm ($^{11}/_{32}$ in.) (note that the thickness for the gusset plate using A36 steel was determined to be 12 mm ($^{15}/_{32}$ in.)) using Eq. 1 (note that R_y = 1.1 for ASTM A572 Grade 50 steel [10]) of the hand-calculated approach, which neglected the frame deformation effects.

The maximum first-principal stress located at the end of the welded joint of the A572, Grade 50 gusset plate, therefore, can be estimated to be about 413 MPa (59.9 ksi) [= 223 MPa × (12 mm / 9 mm) × (705 kN / 507 kN)] using the finite element approach I which neglects the effects of frame deformation. Note that the 223 MPa (32.3 ksi) is the maximum first-principal stress at the end of the welded joint of the A36 gusset plate, as shown in Figure 11, which neglected frame deformation effects. Also, the maximum first-principal stress located at the end of the welded joint of the A572 Grade 50 gusset plate, therefore, can be estimated to be about 465 MPa (67.4 ksi) [= 251 MPa × (12 mm / 9 mm) × (705 kN / 507 kN)] using the finite element approach II which considers the effects of frame deformation. Note that the 251 MPa (36.4 ksi) is the maximum first-principal stress at the end of the welded joint of the A36 gusset plate, as shown in Figure 18, which considered frame deformation effects. Since 465 MPa (67.4 ksi) is larger than 448 MPa (65.0 ksi) (the specified minimum tensile strength of the ASTM A572, Grade 50 steel), fracturing may occur at the end of the weld joint of the A572, Grade 50 gusset plate. The above example indicates that the hand-calculated approach, which neglects the effects of frame deformation, may result in an under-design of the gusset plate.

Note that if A992 steel (instead of A36 steel) is used for the beam and column shown in Figure 16, the effects of frame deformation on the stress distribution in gusset plates will not change since the maximum von Mises stress in the column and beam caused by the applied force (485 kN (109 kips)) is below 248 MPa (36 ksi, the yielding stress of A36 steel).

In order to validate the finite element procedure presented in this paper, the following investigation has been conducted:

First, a compressive load increment was applied at the end of the bracing element as shown in Figure 8(a). As the load gradually increased, the stress concentration gradually accumulated at the end of the welded joint. When the load applied to the bracing element reached 198 kN (44.5 kips) (the approximate ultimate compressive capacity of the bracing element), the von Mises stress reached 84 MPa (12.2 ksi) at the end of the welded joint. Note that there is no frame deformation effect on the gusset plate in this case.

Second, a load increment was applied horizontally toward the upper right-hand corner of the frame as shown in Figure 16(a). When the applied load reached 189 kN (42.5 kips), the compressive force in the bracing element reached 198 kN (44.5 kips). Meanwhile, the von Mises stress reached 103

MPa (14.9 ksi) at the end of the welded joint. Note that the increase in von Mises stress at the end of the welded joint was caused by the effects of frame deformation on the gusset plate.

The compressive capacity of the gusset plate decreased due to the increase in von Mises stress at the end of the connected joint caused by the effects of frame deformation on the gusset plate. This result agrees with that of the full-scale tests conducted by Cheng, Grondin, and Yam [5].

5. CONCLUSIONS

This paper has focused on the effects of the frame deformation on welded gusset plates for diagonal bracing elements loaded in tension. A design example for a brace-beam-column gusset plate connection using the traditional hand-calculated approach, which neglects the frame deformation effects, has been given in this paper. Also, two finite element approaches have been used to investigate the adequacy of the gusset plate designed by using the hand-calculated approach. The first approach has neglected the frame deformation effects while the second approach has considered the effects.

The following conclusions are inferred from this study: (1) When a diagonal bracing member is subjected to a tensile force, the gusset plate will be stressed in tension, shear, and compression; the tension and shear stresses in the gusset plate are caused by the tensile force in the bracing member, while the compression stress in the gusset plate is caused by the deflections of the beam and column of the braced frame. (2) When the effects of frame deformation are considered, the resultant shear forces acting along the horizontal and vertical gusset edges will be increased while the resultant tensile forces acting on the horizontal and vertical gusset edges will be decreased. As a result, the combined effects of the factored tension and shear forces at the gusset edges will be increased. (3) Both the von Mises and first-principal stresses located at the end of the welded joint (which is in the Whitmore section) will be increased when the effects of the frame deformation are considered. Therefore, the traditional hand-calculated approach illustrated in this paper, which neglected the frame deformation effects, may result in an under-design of the gusset plate. (4) The increases in stress at the end of the weld joint caused by the frame deformation effects vary widely in magnitude and depend on the following factors: (a) the relative stiffness between the beam (bending stiffness), the column (bending stiffness), and the bracing element (axial deformation stiffness), (b) the configuration of the gusset plate, and (c) the degree of angle between the center line of the column and the center line of the bracing element (or the degree of angle between the center line of the beam and the center line of the bracing element).

All possible conditions of the relative stiffness, the gusset plate configuration, and the slope of the bracing element, therefore, need to be statistically studied in order to determine the maximum possible increases in stress caused by the frame deformation effects.

Due to the frame deformation effects, a rigid frame with brace-beam-column connections is highly indeterminate. Any simplifying hand-calculated approaches could be too approximate to be used for the final design of the gusset plate. The finite element analysis considering frame deformation effects, therefore, is recommended for the design of gusset plates for brace-beam-column connections. Also, this paper concludes that higher ductile structural steel (for example, A36 steel) can mitigate the frame deformation effects better than A572 Grade 50 steel.

NOTATION

The following symbols are used in this paper:

A_e = area of the Whitmore effective section of a gusset plate
A_g = gross area
A_n = net area
e_b = one-half the depth of the beam being used
e_c = one-half the depth of the column being used
F_{EXX} = weld metal tensile strength
F_u = specified minimum tensile strength of the type of steel being used
F_y = specified minimum yield stress of the type of steel being used
f_a = tension force along the gusset-to-beam (or column) interface
f_{avg} = average force at the gusset-to-beam (or column) interface
f_b = in-plane bending stress along the gusset-to-beam (or column) interface
f_{peak} = peak force at the gusset-to-beam (or column) interface
f_v = shear force along the gusset-to-beam (or column) interface
H_{ub} = factored shear force at the gusset-to-beam connection
H_{uc} = factored axial force at the gusset-to-column connection
l = length of weld
l_w = Whitmore effective width of a plate
P_u = factored load
R_y = ratio of the expected yield strength to the specified minimum yield strength of the grade of steel to be used
t = thickness of a gusset plate
t_e = effective throat of fillet weld
U = reduction coefficient, used in calculating effective net area
V_{ub} = factored axial force at the gusset-to-beam connection
V_{uc} = factored shear force at the gusset-to-column connection
$\bar{x}$ = horizontal distance from the outer edge of a channel web to its centroid
α = distance from the face of the column flange to the centroid of the gusset-to-beam connection
β = distance from the face of the beam flange to the centroid of the gusset-to-column connection
r = distance from the working point to the centroid of the gusset plate connection
ϕP_n = design strength
$\phi_t P_n$ = design tensile strength
ϕR_n = design strength of the fillet weld for the gusset-to-beam (or column) flange connection

REFERENCES

[1] SEAOC, “2006 IBC Structural/Seismic Design Manual, Building Design Examples for Steel and Concrete”, Structural Engineers Association of California, Sacramento, Calif., 2006.

[2] Thornton, W.A., “Bracing Connections for Heavy Construction”, Engineering Journal, American Institute of Steel Construction, 3rd Quarter, 1984, Vol. 21, No. 3, pp. 139-148.

[3] Richard, R., “Analysis of Large Bracing Connection Designs for Heavy Construction”, Proceedings of the 1986 National Engineering Conference, AISC, Nashville, June 12-14, 1986.

[4] Astaneh-Asl, A., "Seismic Behavior and Design of Gusset Plates", Steel Tips Report, Structural Steel Educational Council, Moraga, Calif., 1998.
[5] Cheng, J.J.R., Grondin,G.Y. and Yam,M.C.H., "Design and Behavior of Gusset Plate Connections", Steel Connection IV Workshop, Roanoke, VA., 2000.
[6] Whitmore, R.E., "Experimental Investigation of Stresses in Gusset Plates", Bulletin No. 16, Engineering Experiment Station, Univ. of Tennessee, TN., 1952.
[7] AISC, "Steel Construction Manual", 14th Edition, American Institute of Steel Construction, Inc., Chicago, IL., 2011.
[8] Thornton, W.A., "On the Analysis and Design of Bracing Connections", National Steel Construction Conference Proceedings, AISC, Chicago, IL., 1991, pp. 26.1-26.33.
[9] AISC and SSEC, "Seismic Design Manual", American Institute of Steel Construction, Inc., Chicago, IL., 2006.
[10] AISC, "Seismic Provisions for Structural Steel Buildings", American Institute of Steel Construction, Inc., Chicago, IL., 2005.
[11] NISA, "NISA User's Manual", Engineering Mechanics Research Corporation, Troy, Michigan, 1998.
[12] Salmon, C.G., Johnson, J.E. and Malhas F.A., "Steel structures, design and behavior", 5th Ed., Pearson Prentice Hall, Upper Saddle River, N.J., 2009.
[13] The Lincoln Electric Company, "The Procedure Handbook of Arc Welding", 13th Ed., The Lincoln Electric Company, Cleveland, Ohio., 1994.

ORDER FORM

Advanced Steel Construction, an international journal

From: _____

To: ***Secretariat, Advanced Steel Construction, an international journal***
Fax: (852) 2334-6389

I/ We would like to enter a subscription to the ***International Journal of Advanced Steel Construction (IJASC)*** *published by The Hong Kong Institute of Steel Construction.*

Please complete the form and send to:

International Journal of Advanced Steel Construction
c/o Department of Civil and Structural Engineering
The Hong Kong Polytechnic University
Hunghom, Kowloon, Hong Kong

Fax: (852) 2334-6389 Email: ceslchan@polyu.edu.hk

Published by : The Hong Kong Institute of Steel Construction
Website: http://www.hkisc.org/

Please tick the appropriate box

- ❑ Please enter my subscription **(4 issues per year)**.
- ❑ Please send me a complimentary copy of the *Advanced Steel Construction, an International Journal (IJASC).*

Please tick the appropriate box(es)

	Print only	**On-line only**	**Print & On-line**
Personal	❑ US$ 100	❑ US$ 100	❑ US$ 125
Institutional	❑ US$ 250	❑ US$ 250	❑ US$ 280
Postage	❑ Surface mail	(no charge)	
	❑ Air mail	(US$ 30)	
Total Amount	**US$** _____		

Methods of payment *(please tick the appropriate box(es))*

❑ Please invoice me
❑ Cheque enclosed for US$ _____ payable to
Hong Kong Institute of Steel Construction Limited
(No personal cheque accepted)

Ship to

Name (Prof./ Dr./ Mr./ Ms.) _____
Address _____
_____
_____
City/ State/ Postal Code _____
Country _____
Email _____ Fax _____